

Multistate GTPases Control Cotranslational Protein Targeting

Thesis by

Xin Zhang

In Partial Fulfillment of the Requirements
for the Degree of
Doctor of Philosophy



California Institute of Technology

Pasadena, California

2010

(Defended May 12, 2010)

© 2010

Xin Zhang

All Rights Reserved

Acknowledgements

I dedicate this dissertation to my parents. I thank them for bringing me to this world, raising me up, teaching me early and well, and having always been supportive to me. My sisters and brothers-in-law have always been there for me and provided great support and love to me. My lovely and cute nephew and nieces have brought happiness to my life.

My graduate life has been both challenging and exciting. One of the reasons why this is so is my advisor, Dr. Shu-ou Shan. Being fairly brave, Shu-ou took me as her first graduate student and started her rocky journey to train me into an experimental biochemist from a theoretical chemist. She successfully led a critical turn in my career and now I formally stumble into the fascinating area where the kinetic and thermodynamic nature of protein machineries is appreciated and revealed. I also feel extremely lucky that she has been working very close to me in person; and that experience has given me the exclusive opportunity to learn from a pair of golden hands and a smart mind. Above all, she has been tremendously encouraging and supportive, and certainly has pushed me to extend myself into new areas. Shu-ou has tried her best to train me as a future professor who makes contributions to understand nature, and I will work my best to make sure that her hope does not fall.

Another two people who have shaped my graduate life are Sowmya Chandrasekar and Peera Jaru-Ampornpan. They are my mentors in addition to Shu-ou in the lab, and are my best friends in my personal life. Sowmya is an exceptional experimental biologist

and has been my bench-side mentor since my first day in the lab. Peera is a certainly talented graduate student. Her insights into various biological questions always enlighten me in the way that I can dive into a new direction with her lead. The genuine friendship and selfless help from them and their significant others, Vijay Natraj and Knot Pipatsrisawat, have made every bit of my success possible.

I also owe a debt of gratitude to my undergraduate advisor Ke-li Han, who is also my advisor during my graduate school in China. He led me into the academic path in my senior year and furthered my research into the field of quantum dynamics of chemical reactions. In my years at Caltech, he remained a valuable mentor and kept being supportive of all my decisions.

I would also like to thank Bill Goddard, who was my advisor prior to Shu-ou. Bill was extremely understanding and supportive when I decided to make the transition to experimental biochemistry, and his kindness made this transition so smooth. Even today, I am still beginning to appreciate the significance of some of the things that he taught me.

I would also like to thank the other members in my committee, Doug Rees, Harry Gray, and Jack Beauchamp. Doug and Harry have given me much advice when I was choosing a future direction for the postdoctoral training, and I have benefited a lot from my conversations with them. Harry also generously provided the environment for me to carry out the time-resolved fluorescence experiment.

I also enjoyed a lot working with my undergraduates, Simon Kung, Jaeyoon Chung, and Kai Wang. Simon purified SRP RNA mutants for me and helped me to finish the work in chapter 2. Jaeyoon gets a pair of golden hands in protein purifications, and he

assisted me to finish the work in chapter 3. Kai characterized the substrate EspP in chapter 4.

Other people in the Shan lab are certainly wonderful co-workers and have helped me at various times. They are Rumana Rashid, Vinh Lam, Dawei Zhang, David Akopian, Kuang Shen, Ishu Saraogi, Thang Nguyen, and Aileen Ariosa. Nathan Piece and Michael Rome also make a wonderful addition to the Shan lab. I am deeply grateful to these people who have made my daily life enjoyable.

I also thank my collaborators who have helped me in certain projects. Tetsunari Kimura and Jay Winkler helped me to carry out all the time-resolved fluorescence experiments. Christiane Schaffitzel and Nenad Ban offered valuable assistance in the RNC purification and sponsored my trip to ETH, Zurich. Yun Mou and Stephen Mayo provided help in molecular docking and Brownian dynamics simulations.

In addition to the science, my life at Caltech has been very enjoyable because of my wonderful friends. The moments that we shared together will be always kept in my heart. These friends are Rui Cai, Zhou Lu, Yimin Xu, Zhaoyan Zhu, Tian Lan, Xiaolan Zhang, Julius Su, Yanling Wu, Yu Zhao, Qi An, Chenying Gu, Yun Wang, and Yun Mou.

In particular, I would like to thank Dr. Rui Cai for always being around and supportive for more than ten years. I am excited to see his independent career taking off in China soon, and I look forward to the bright future.

Abstract

The cotranslational protein targeting process transports roughly one-third of proteins in a cell's genome from the cytoplasmic space to the membrane compartments. This process is regulated by the signal recognition particle (SRP) and its receptor (SR). I aim to understand how the complex assembly and activation of GTP hydrolysis during the SRP-SR interaction are controlled so that the SRP machinery functions as a molecular switch to regulate the series of molecular events in space and time. Using a combination of biochemical and biophysical approaches, this dissertation has defined the kinetic and thermodynamic framework of the SRP-SR interaction and has elucidated the regulatory role of the SRP-SR interaction on the protein targeting process. In particular, this dissertation demonstrates that the function of the SRP machinery is governed by a series of ordered conformational changes during SRP-SR interaction that culminate in their activation of GTP hydrolysis. Further, these conformational changes closely monitor and actively respond to the biological cues so that they provide discrete control points at which regulation can be exerted on the protein targeting reaction spatially and temporally. The paradigm provided in this dissertation offers a mechanistic view of another fascinating system in which multistate protein machineries control critical biological processes with exquisite order.

Contents

1	Introduction	1
2	A Multistep Mechanism for Assembly of the SRP-SR Complex	7
2.1	Abstract.....	8
2.2	Introduction.....	8
2.3	Results.....	12
2.4	Discussion.....	26
2.5	Materials and Methods.....	35
2.6	Supplementary Figures.....	38
2.7	Acknowledgements.....	41
3	Dynamics of the Transient Intermediate during SRP-SR Association	42
3.1	Abstract.....	43
3.2	Introduction.....	43
3.3	Results.....	45
3.4	Discussion.....	55
3.5	Material and Methods.....	58
3.6	Supplementary Figures.....	67
3.7	Acknowledgements.....	75
4	Multiple Conformational Switches Control Cotranslational Protein Targeting	76
4.1	Abstract.....	77

4.2	Introduction.....	78
4.3	Results.....	80
4.4	Discussion.....	90
4.6	Materials and Methods.....	94
4.7	Supplementary Figures.....	98
4.8	Acknowledgements.....	103
5	Sequential Checkpoints Govern Substrate Selection during Cotranslational Protein Targeting	104
5.1	Abstract.....	105
5.2	Introduction.....	105
5.3	Results.....	107
5.4	Discussion.....	117
5.6	Materials and Methods.....	120
5.7	Supplementary Text.....	132
5.8	Supplementary Figures.....	136
5.9	Acknowledgements.....	145
	Bibliography	146

Chapter 1

Introduction

We now know that almost every major biological process is controlled by protein assemblies that comprise two or more proteins that interact with one another to exert their regulatory function (1). These assemblies are called protein machineries because the way that they work at a microscopic scale resembles the way that machines work at a macroscopic scale. Underlying these highly controlled activities are the ordered conformational changes that take place in the protein components of the machineries. These conformational changes often lead to molecular events that drive efficient regulation of the biological processes.

One key process in protein biogenesis is the cotranslational protein targeting (2). This process transports roughly one-third of proteins in a cell's genome from cytoplasmic space to the membrane compartments. This process, like many others, is controlled by the protein machinery in which the protein components interact with one another. This machinery is composed primarily of the signal recognition particle (SRP) and its receptor (SR). In all cells, the SRP machinery carries out targeting of secretory and membrane proteins to the endoplasmic reticulum membrane in eukaryotic cells or to the plasma membrane in bacteria.

Although the SRP machinery varies widely in size and composition through evolution, the functional core of the SRP machinery is well conserved in a variety of organisms. The center of the SRP is comprised of the universally conserved SRP54 guanosine 5'-triphosphatases (GTPases) in complex with the SRP RNA. The SRP

receptor also contains a highly conserved SR GTPase (SR α) subunit that serves as a connector between the SRP and the cellular membrane. Thus, SRP and SR GTPases together form the center of the SRP machinery and provide exquisite spatial and temporal controls to the protein targeting process.

The SRP-dependent protein targeting process involves a series of highly ordered molecular events (3). These events begin when a nascent polypeptide chain destined for the endoplasmic reticulum (ER) or the secretory pathway emerges from a translating ribosome. The signal sequence that specifies its cellular localization is recognized by the SRP. The ribosome•nascent chain complex (RNC), herein denoted as cargo, is then directed to the cellular membrane by the interaction between the SRP and SR. Upon arrival at the membrane, the conformation of the SRP•RNC complex switches from a cargo-loading mode to a cargo-releasing mode in which the RNC is unloaded from the SRP and passed on the protein conducting channel, or the translocon, on the membrane. After the cargo is released, the SRP dissociates from the SR to allow the cargo to be recycled in the next round of protein targeting. Meanwhile, the synthesis of the nascent polypeptide is finished and the nascent protein is either integrated into the membrane or translocated through the membrane to enter its journey to the destined cellular compartment.

SRP and SR GTPases together compose a class of noncanonical GTPases in comparison to the classical GTPases such as Ras, G α , and EF-Tu (3). They do not exhibit significant conformational changes among the apo, guanosine 5'-diphosphate (GDP)-bound and guanosine 5'-triphosphate (GTP)-bound states. Further, these GTPases bind to nucleotides weakly and exchange from GDP to GTP rapidly. However, free SRP and SR

GTPases bound to GTP have a low basal activity to hydrolyze GTP because the key catalytic residues for GTP hydrolysis are not correctly aligned with the bound nucleotide. Instead, GTP binding enables the SRP and SR GTPases to form a thermodynamically stable heterodimeric complex. In this complex, the two GTPases reciprocally activate the GTP hydrolysis activity of one another by two to four orders of magnitude. Following GTP hydrolysis, the GDP-bound SRP-SR complex would lose its affinity and quickly dissociate to regenerate free SRP and SR GTPases for the next cycle.

Since the SRP and SR GTPase are intrinsically capable of multiple rounds of dimerization and GTP hydrolysis, it is of interest to understand how the complex assembly and GTPase activation are controlled so that these GTPase function as molecular switches to regulate the series of molecular events in space and time. The goal of this dissertation is to elucidate the “hidden facts” inside the SRP machinery that control the protein targeting process both efficiently and faithfully. In particular, most efforts have been made to understand how the SRP and SR interact with one another to coordinate the ordered series of molecular events during the protein targeting. Thus, the studies that were carried out in this dissertation focus on the molecular mechanism of the interaction between the SRP and SR GTPases, and on how this interaction responds actively to the cues such as cargos and thus how this interaction helps maintain the efficiency and fidelity of the protein targeting process.

Chapter 2 (4) defines the kinetic and thermodynamic framework of the SRP-SR interaction. A transient, GTP-independent early intermediate during the assembly of a stable SRP•SR complex is discovered by a highly sensitive fluorescence assay in real time. This further demonstrates that the SRP•SR complex assembly is a complex process

that involves at least two steps. In the initial step, an early, GTP-independent SRP-SR complex is formed via the fast association between the SRP and SR. In the second step, the GTP-dependent conformational rearrangements precede the formation of a stable complex. The SRP RNA significantly stabilizes the early, GTP-independent intermediate. Further, mutational analyses show that there is a strong correlation between the ability of the mutant SRP RNAs to stabilize the early intermediate and their ability to accelerate the SRP•SR complex formation. Thus, the SRP RNA is proposed to stabilize the transient early intermediate to give it a longer dwell time and therefore a higher probability to rearrange to the stable complex.

Chapter 3 defines the landscape of the transient intermediate during assembly of a stable SRP-SR complex. Direct structural characterization of a transient intermediate ensemble is challenging because the intermediate tends to either dissociate or rearrange to the stable complex. In this work, an ensemble of the SRP-SR early intermediate is generated by stalling the conformational rearrangements to form the stable complex. Thus, the structural properties of the early intermediate can be directly characterized under equilibrium condition. The interaction surface of the early intermediate is both similar to and different from that of the stable complex. Further, a nanosecond timescale experiment reveals a broad conformational distribution of the early intermediate. These conformational states allow the free SRP and SR GTPases to search the optimal routes in the configurational space toward an efficient assembly of the stable complex. Interestingly, the landscape of the early intermediate actively responds to the cargos, suggesting that the early intermediate could potentially serve as a control point to the protein targeting process.

Chapter 4 (5) focuses on how SRP machinery ensures the efficiency of the protein targeting reaction by examining the effect of cargos on the SRP-SR interaction. Since the conformational dynamics of the early intermediate actively responds to the cargos, I investigate how the cargos kinetically and thermodynamically modulate a series of discrete conformational rearrangements during the SRP-SR interaction. The cargo for SRP is found to accelerate the SRP-SR complex assembly by over two orders of magnitude, thereby driving rapid and efficient delivery of cargo to the membrane. A series of subsequent rearrangements in the SRP•SR GTPase complex switch the SRP from the cargo-binding mode to the cargo-releasing mode where the cargo can be unloaded during the late stages of protein targeting. Further, the cargo delays GTPase activation in the SRP•SR complex by an order of magnitude. The slower GTP hydrolysis in a RNC•SRP•SR complex creates an important time window that could further improve the efficiency of protein targeting. This work shows that the SRP and SR GTPases constitute a self-sufficient system that provides exquisite spatial and temporal control points to maintain the efficiency of protein targeting.

Chapter 5 answers how SRP machinery maintains the fidelity of the substrate selection in the protein targeting process. The “signal hypothesis” postulates that the signal sequence on a protein allows it to be specifically recognized by targeting factors such as SRP, which mediates the delivery of the protein to the correct cellular compartments. It was generally thought that fidelity arises from the inability of SRP to bind strongly to incorrect cargos. Instead, I show that incorrect cargos are further rejected through a series of fidelity checkpoints during subsequent steps of targeting, including complex formation between the SRP and SR and kinetic proofreading through GTP

hydrolysis. Thus, the SRP pathway achieves high fidelity of substrate selection through the cumulative effect of multiple checkpoints; this principle may be generally applicable to other complex cellular pathways that need to recognize degenerate signals or discriminate between correct and incorrect substrates based on minor differences.

Overall, this thesis establishes the framework of how the SRP machinery achieves an efficient and faithful co-translational protein targeting process. In particular, I show that the function of the SRP machinery is governed by a series of ordered conformational changes during the SRP-SR interaction that culminates in their GTPase activation. These conformational changes respond actively to the cargos so that they could provide discrete control points at which regulation can be exerted on the protein targeting process spatially and temporally. The paradigm provided in this thesis adds to an increasing collection of knowledge on how critical biological processes are regulated by multistate protein machineries.

Chapter 2

A Multistep Mechanism for Assembly of the SRP-SR Complex

A version of this chapter has been published as

X Zhang, S Kung, and S-O Shan, Journal of Molecular Biology, (2008), 381, 581-593.

2.1 Abstract

Two GTPases in the signal recognition particle (SRP) and its receptor (SR) control the delivery of newly synthesized proteins to the ER or plasma membrane. During the protein targeting reaction, the 4.5S SRP RNA accelerates the association between the two GTPases by 400 fold. Using fluorescence resonance energy transfer (FRET), we demonstrate here that formation of a stable SRP•SR complex involves two distinct steps: a fast initial association between SRP and SR to form an early, GTP-independent complex, followed by a GTP-dependent conformational rearrangement to form the stable, final complex. We also found that the 4.5S SRP RNA significantly stabilizes the early, GTP-independent intermediate. Further, mutational analyses show that there is a strong correlation between the ability of the mutant SRP RNAs to stabilize the early intermediate and their ability to accelerate SRP•SR complex formation. We propose that the SRP RNA, by stabilizing the transient early intermediate, can give this intermediate a longer dwell time and therefore a higher probability to rearrange to the final, stable complex. This provides a coherent model that explains how the 4.5S RNA exerts its catalytic role in SRP•SR complex assembly.

2.2 Introduction

To maintain proper cellular function, a cell needs to efficiently and accurately deliver all its proteins to the different subcellular organelles. The signal recognition particle (SRP) and its receptor (SR) constitute a universally conserved machinery to deliver newly synthesized proteins from the cytoplasm to the eukaryotic endoplasmic reticulum (ER) membrane, or the bacterial plasma membrane (2, 6, 7). The protein

targeting reaction consists of several ordered steps that ensure the efficiency and fidelity of this process (8, 9). At the beginning of the targeting cycle, the SRP recognizes translating ribosome that carries a signal sequence on the nascent chain. The SRP then forms a complex with SR localized on the target membrane; this process brings the ribosome•nascent chain complex (RNC) to the membrane surface. Upon arrival at the membrane, conformational changes in the SRP•SR complex drive the release of the RNC from the SRP to a protein conducting channel composed of the sec61p (or secYEG in bacteria) complex (10). Once the RNC is released, the SRP and SR dissociate into free components, allowing a new round of the protein targeting reaction. Thus, the ordered assembly and disassembly of the SRP•SR complex control the delivery of proteins to their proper cellular destinations.

In eukaryotes, SRP is a universally conserved ribonucleoprotein complex consisting of six proteins and an SRP RNA (11-13). The functional core of the SRP requires only two components: the conserved SRP54 protein in complex with the SRP RNA. The SRP54 (called Ffh in *E. coli*) is composed of two structurally and functionally distinct domains: a methionine-rich M domain and an NG domain. The M domain recognizes the signal sequences and binds the SRP RNA (14-18). A GTPase, G-domain and an N-terminal four helix bundle (the N-domain) together form a structural and functional unit called the NG domain, which binds and hydrolyzes GTP and forms a complex with SR (called FtsY in bacteria) (19-22). The NG domain was also suggested to play a role in signal peptide recognition (23). The SRP and SR GTPases use a regulatory mechanism distinct from that of classical signaling GTPases such as Ras, Rho, and Ran (24). The structure of both GTPases are similar regardless of whether GTP or

GDP is bound (25-28). Thus, the SRP and SR do not switch between active and inactive states depending on whether GTP or GDP is bound. Moreover, these GTPases bind nucleotides weakly and exchange nucleotides quickly, so that no external nucleotide exchange factors are required to switch these GTPases from the GDP- to the GTP-bound state (29). In addition, the SRP and SR reciprocally stimulate each other's GTPase activity upon formation of the SRP•SR complex (21). Therefore, no external GTPase activating proteins are required to regulate the switch of these GTPases from the GTP- to the GDP-bound state. Instead, recent biochemical and biophysical analyses suggest that several discrete conformational changes occur during the binding and reciprocal activation between the two proteins, and each of these conformation may provide a potential point for regulation during the protein targeting reaction (9, 10).

The SRP RNA has been shown to play an indispensable role in protein targeting both in vitro and in vivo (30-35). The size of the SRP RNA varies widely from bacteria to yeast and mammalian cells; nevertheless, the most phylogenetically conserved region of the SRP RNA, domain IV, has been maintained in all three kingdoms of life (36, 37). The role of SRP RNA may involve recognition and binding of the ribosome and signal sequences (15, 30, 38), and stabilization of the folding of the M-domain. In addition, it was also proposed to bind to and stabilize the NG domain of Ffh (39). Intriguingly, kinetic analyses of the role of the 4.5S SRP RNA on the GTPase cycles of Ffh and FtsY showed that the RNA also plays a critical role in the interaction between the two GTPases (21, 29). In the absence of the SRP RNA, Ffh-FtsY association is extremely slow, with a rate constant of $5 \times 10^3 \text{ M}^{-1}\text{s}^{-1}$, and the SRP RNA accelerates their association kinetics by 400 fold (21, 29, 40). An additional step, GTP hydrolysis after the

complex is formed, is also enhanced 8 fold by the 4.5S RNA (29). Thus, the presence of the SRP RNA brings the interaction kinetics between the SRP and SR to an appropriate range for their biological functions. The SRP RNA contains a highly conserved GNRA tetraloop that was shown to be essential for the interaction between the SRP and SR. Tetraloop mutants were reported to impair the binding between SRP and SR, cause a reduction in the GTPase activity of the SRP•SR complex, as well as fail to support normal cell growth *in vivo* (31, 34). A site-directed hydroxyl radical probing study further suggest that the tetraloop is located close to the heterodimer interface of the SRP•SR GTPase complex (41).

To probe the conformational dynamics during the SRP-SR interaction and to elucidate how the SRP RNA exerts its catalytic role on SRP•SR complex assembly, we developed a highly sensitive FRET assay to monitor the interaction between the SRP and SR in real time. This new assay led to the discovery of a new SRP•SR complex that forms independently of GTP. This GTP-independent complex has been observed only once in a surface-resonance experiment using mammalian SRP and SR (42). Further characterization identifies this GTP-independent complex as an early intermediate during the initial stage of the SRP-SR interaction. Formation of the early intermediate is substantially stabilized by the 4.5S RNA, and 4.5S RNA tetraloop mutants that fail to stabilize this intermediate also fail to accelerate SRP•SR complex assembly. We propose that the catalytic role of 4.5S RNA on complex assembly can be explained by its stabilizing effect on the early intermediate, which increases its probability to rearrange to the final, GTP-stabilized complex.

2.3 Results

To characterize the conformational dynamics during the SRP-SR interaction, we developed a real time assay based on fluorescence resonance energy transfer (FRET). The basic strategy is to engineer a single cysteine residue on cysteine-less Ffh and FtsY proteins, and label the single cysteines with thio-reactive fluorescent probes (figure 2.1a). In Ffh, the intrinsic cysteine at position 406 can be replaced with serine without disrupting its function (41, 43). A cysteine was introduced at position 153 of cysteine-less Ffh and labeled with maleimide-coumarin (DACM) as the FRET donor. FtsY does not contain any cysteine residue; thereby a cysteine was introduced at position 345 and labeled with maleimide-BODIPY-fluorescein (BODIPY-FL) as the FRET acceptor. These probes are close to the nucleotide binding pocket in the G domains of both proteins, and are 31 Å apart as estimated from the crystal structure of the *Thermus aquaticus* Ffh•FtsY complex (figure 2.1a) (20). The cysteine mutation and fluorescence labeling do not alter the ability of Ffh and FtsY to bind and activate each other's GTPase activity (figure 2.S1), nor do they affect their ability to translocate model SRP substrates into ER microsomal membranes.

2.3.1 A GTP-Independent Complex is Detected by the FRET Assay

Previous studies have shown that SRP and SR form a stable complex in the presence of GTP or non-hydrolyzable GTP analogues such as 5'-guanylylimidodiphosphate (GppNHp), with dissociation constants of 16-30 nM (21). As expected, a significant amount of FRET was observed upon assembly of the SRP•SR complex in the presence of GppNHp (figure 2.1b). At saturating protein concentrations, the FRET

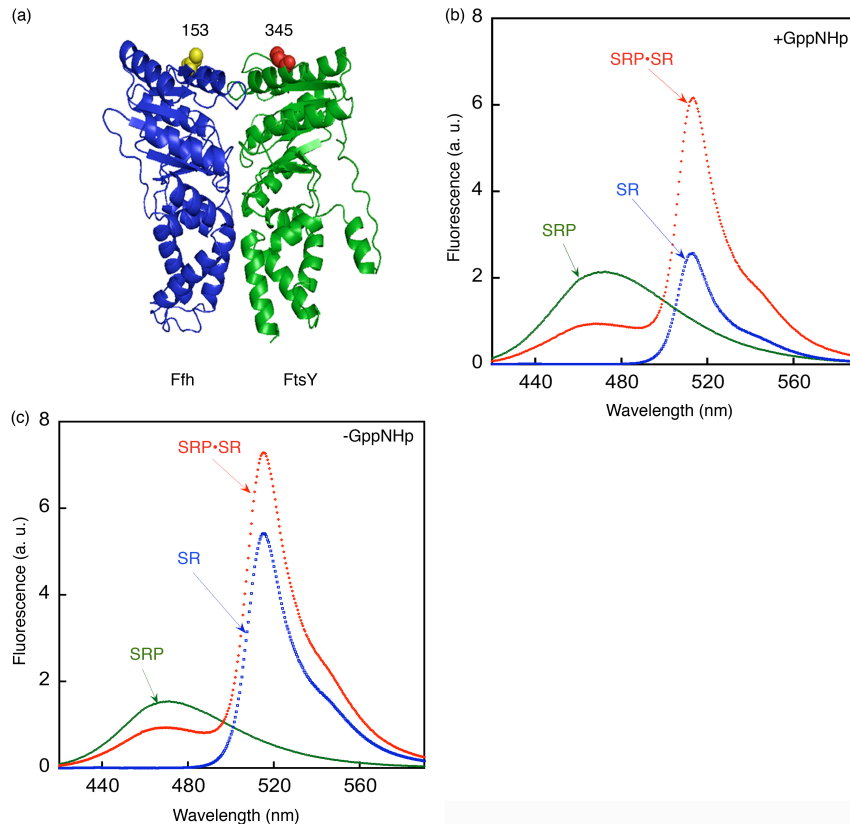


Figure 2.1. SRP and SR can form a complex independently of GTP. (a) Position of FRET donor (●) and acceptor (●) probes on the SRP (Ffh) and SR (FtsY) on a co-crystal structure of the Ffh•FtsY complex (20). (b) Fluorescence emission spectrum of SRP•SR complex in the presence of 100 microM GppNHp. 0.5 microM SRP and 2 microM SR were incubated for 10 minutes at 25 °C to form the SRP•SR complex (red). SRP- and SR-only spectra (green and blue, respectively) were obtained by incubating fluorescently labeled SRP (or SR) with unlabeled SR (or SRP). (c) Fluorescence emission spectrum of SRP•SR complex in the absence of GppNHp. 5 microM SRP and 15 microM SR were incubated at 25 °C for 10 minutes. SRP or SR-only spectra were obtained as in part (b).

efficiency was 0.80 (figure 2.2a), in good agreement with the distance between the two residues in the crystal structure and the Förster radius of this donor-acceptor pair. To our surprise, when GppNHp was either removed from the reaction mix or replaced by GDP, efficient FRET was also observed (figure 2.1c), suggesting that an SRP•SR complex can be formed independently of GTP.

The affinities of the GTP-dependent and GTP-independent complexes were measured by equilibrium titration. The dissociation constant of the complex formed in the presence of GppNHp was determined to be 16 nM using this FRET assay (figure 2.2a, circles), consistent with previous studies (21). In contrast, a dissociation constant of 4–10 microM was observed for the complex assembled in the presence of GDP or no nucleotide (figure 2.2a, squares and triangles, respectively). Thus, the γ -phosphate of GTP contributes over 250 fold to the stability of the SRP•SR complex. In these titration experiments, the FRET value at saturating protein concentrations represent the FRET efficiency of the two probes in their respective complexes: the GTP-independent complex has a FRET efficiency of 0.62, which is ~25% lower than that of the GTP-dependent complex (0.80). The different FRET values suggest that these two complexes have different conformations in which the donor and acceptor fluorophores are positioned or oriented differently. Similar results were observed when another FRET pair was engineered near the N-domain of each protein (figure 2.S2).

In addition to equilibrium measurements, we also determined the kinetics for assembly and disassembly of the GTP-independent complex by following fluorescence emission from the FRET donor over time. The time course for assembly of the GTP-independent complex fits well to single exponential kinetics (figure 2.3, blue); plots of the observed rate constant against the concentration of SR gave an association rate constant k_{on} of $5.7 \pm 0.5 \times 10^6 \text{ M}^{-1} \text{ s}^{-1}$ (figure 2.2b). This is over 50 times faster than the association kinetics for formation of the GTP-dependent complex previously determined (21). The dissociation rate constant of the GTP-independent complex is $60 \pm 6 \text{ s}^{-1}$ (figure 2.2c), which is 2×10^4 fold faster than that of the GTP-dependent complex (21). Thus in

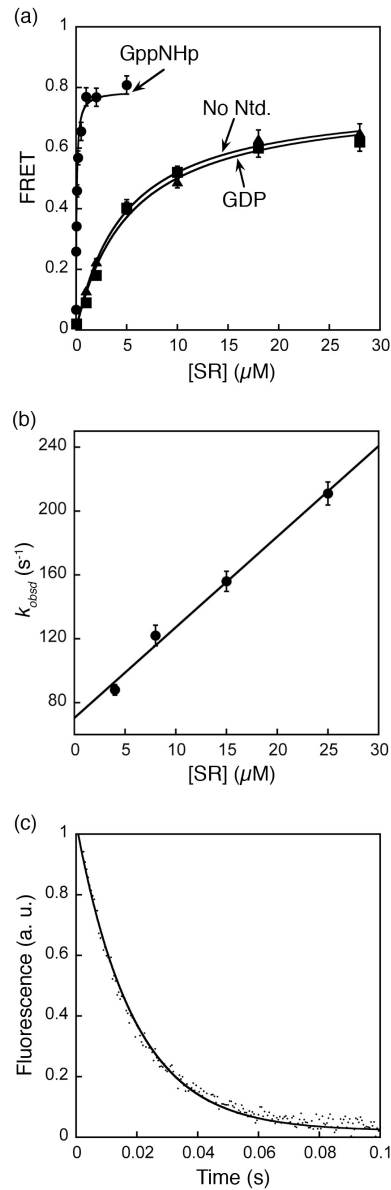


Figure 2.2. Stability and kinetics for formation of the GTP-independent complex. (a) Equilibrium titration of SRP•SR complex with GppNHp (●), GDP (■), and without nucleotide (▲). The data were fit to a single binding equation and gave dissociation constants of 16 nM (GppNHp), 4 μM (GDP) and 4.2 μM (no nucleotide). (b) Association kinetics of GTP-independent complex was measured as described in Methods. Values of observed rate constants were plotted against SR concentration and a linear fit of the data gave an association rate constant of $5.6 \times 10^6 \text{ M}^{-1} \text{ s}^{-1}$. (c) Dissociation kinetics was determined in a pulse-chase experiment described in Methods. The data were fit to a single exponential equation and gave a dissociation rate constant of 60 s^{-1} .

addition to the lower equilibrium stability, the GTP-independent complex is also kinetically much less stable than the GTP-dependent complex previously characterized (21). This explains why this complex was not observed previously based on gel filtration analyses (20), which can only detect kinetically stable complexes.

The following observations strongly suggest that the GTP-independent complex is not an artifact introduced by dye labeling: (1) the FRET value is dependent on protein concentration and is saturable, suggesting that the FRET signal arises from complex formation, rather than nonspecific interactions between the dyes; (2) FRET from the GTP-independent complex can be competed away by unlabeled protein (figure 2.2c); and (3) SR labeled with an environmentally sensitive probe (acrylodan) on position 242 also showed a fluorescence change when the complex was formed in GDP. Thus, FRET provides a robust and highly sensitive assay that allows us to detect, for the first time, a transient GTP-independent SRP•SR complex that has a different conformation than that observed previously for the GTP-dependent complex.

2.3.2 The GTP-Independent Complex Represents a Transient Intermediate on the Pathway for Formation of the GTP-Stabilized Complex

In this section we provide two lines of evidence that strongly suggest that the GTP-independent complex is an on-pathway intermediate preceding the formation of the GTP-dependent complex: (1) an intermediate can be directly detected in the time course for formation of the GTP-dependent complex, and the kinetics for formation of this intermediate agrees with the kinetics for assembly of the GTP-independent complex, and (2) stabilization of the GTP-independent intermediate by the SRP RNA also accelerates

the rate for formation of the final, GTP-dependent complex, consistent with the notion that the GTP-independent complex is an on-pathway intermediate.

The first piece of evidence was obtained from comparison of the kinetics of complex formation in the presence or absence of GppNHp. To ensure that low affinity intermediates can accumulate and be detected, we used a high concentration of SR during complex assembly, and fluorescence emission from the FRET donor was followed over time. The time course for complex formation in the presence of GppNHp exhibits biphasic kinetics (figure 2.3a, red), indicating that there are at least two steps involved in the assembly of the GTP-dependent complex. The first kinetic phase is dependent on SR concentration (figure 2.3b), and therefore represents fast, bimolecular association between SRP and SR to form an intermediate that has a lower FRET value. The second kinetic phase is concentration independent (figure 2.3c) and thus represents the unimolecular rearrangement of this intermediate to a complex that has a higher FRET value. Remarkably, the rate constant of the first kinetic phase coincides very well with that for formation of the GTP-independent complex (figure 2.3a, blue), with observed rate constants of 118 and 122 s⁻¹ at 8 microM SR (figure 2.3a). This strongly suggests that the GTP-independent complex is the intermediate observed in the first kinetic phase during complex assembly in the presence of GppNHp. In contrast to the biphasic kinetic behavior during assembly of the GTP-dependent complex, formation of the GTP-independent complex does not have a second kinetic phase (figure 2.3a, blue), suggesting that the rearrangement represented in the second kinetic phase is strictly GTP-dependent.

A classical criterion for an on-pathway intermediate is that stabilization of the intermediate accelerates the reaction to form the final product. This criterion was

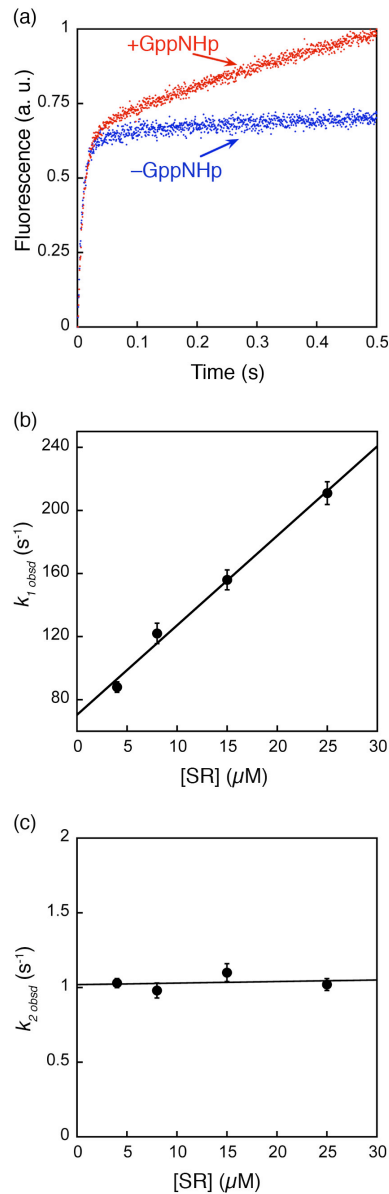


Figure 2.3. Formation of an SRP•SR complex in the presence of GppNHp involves two discrete steps. (a) Comparison of the time courses for complex formation in the absence (blue) and presence of 100 microM GppNHp (red). Data were obtained with 4 microM SRP and 8 microM SR. (b) The observed rate constants of the first kinetic phase during SRP-SR association in the presence of GppNHp were plotted against SR concentration. A linear fit of the data gave an association rate constant of $5.8 \times 10^6 \text{ M}^{-1} \text{ s}^{-1}$ (k_1 in Scheme 2.1). (c) The observed rate constants of the second kinetic phase during SRP•SR association in the presence of GppNHp are independent of SR concentration. The average of these rate constants is 1.03 s^{-1} (k_2 in Scheme I).

satisfied by the effects of the 4.5S SRP RNA on the GTP-independent and GTP-dependent complexes. The GTP-independent complex could not be formed in the absence of the 4.5S RNA (figure 2.4a), even after long periods of incubation when equilibrium had been reached (figure 2.4b). Thus, the 4.5S RNA increases the equilibrium stability of the GTP-independent complex. In contrast, it was shown that a stable GTP-dependent Ffh•SR complex can be formed with or without the 4.5S RNA, but the RNA accelerates the association rate of this complex by 200 fold (cf. figures 2.4c and 2.4d) (21). The results presented here and in the next section show that there is a strong correlation between the ability of the 4.5S RNA to stabilize the GTP-independent complex and its ability to accelerate formation of the GTP-dependent complex. This provides independent evidence that the GTP-independent complex is an on-pathway intermediate. If the GTP-independent complex were off the pathway, then its stabilization by the 4.5S RNA would compromise formation of the native complex in the presence of GppNHp.

Taken together, these results demonstrate that formation of the GTP-stabilized SRP•SR complex involves at least two steps (Scheme 2.1): (1) GTP-independent bimolecular association between the SRP and SR to form a transient intermediate (referred to as the early intermediate); and (2) GTP-dependent rearrangement of the early intermediate to form the stable complex previously observed. As demonstrated previously, additional conformational stages are present even after the stable complex is formed (figure 2.8) (9). Thus, the interaction between the SRP and SRP receptor is a highly dynamic process involving multiple conformational changes during complex assembly and activation.

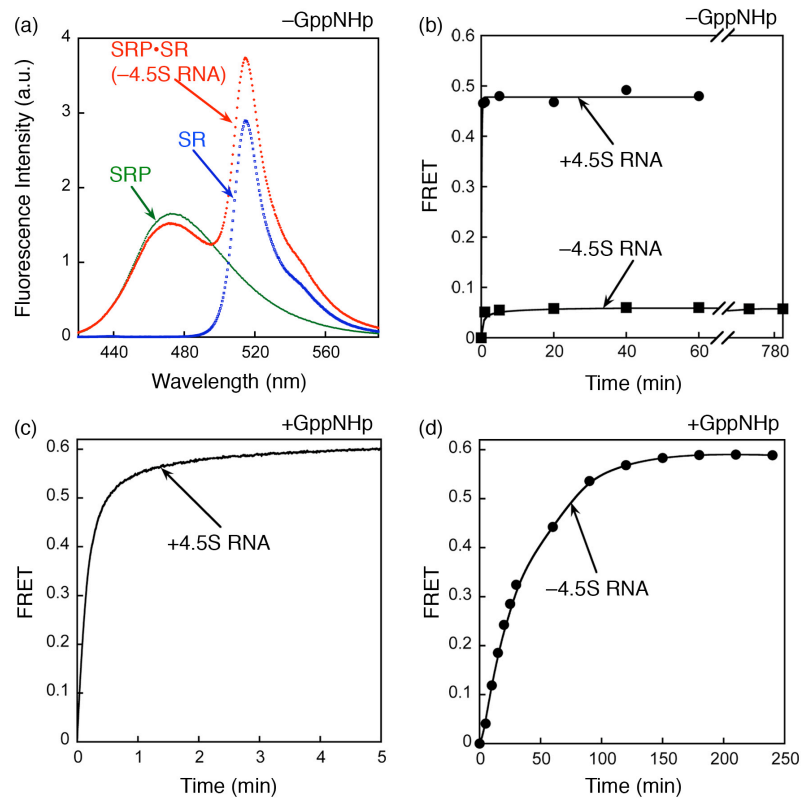


Figure 2.4. The GTP-independent complex is stabilized by the 4.5S RNA. (a) Spectrum of the GTP-independent complex in the absence of 4.5S RNA. The experiment setup is the same as in figure 1c except that the 4.5S RNA was not included. (b) Formation of the GTP-independent complex was monitored in the presence (●) and absence (■) of the 4.5S RNA. (c and d) The time course for formation of the GTP-dependent complex was monitored in the presence (c) and absence (d) of 4.5S RNA. In (c), 0.5 microM SRP and 2 microM SR were used. In (d), 2 microM Ffh and 10 microM SR were used to obtain a faster reaction rate. Note the difference in time scales in (c) and (d).

Scheme 2.1



2.3.3 Defects of Mutant 4.5S RNAs in Formation of the Early Intermediate

Correlates with Defects in Accelerating SRP•SR Complex Formation

The observation that the 4.5S RNA can stabilize the early intermediate suggests that the RNA may exert its catalytic effect on SRP•SR complex formation by prolonging the lifetime of the intermediate, thereby increasing its probability to rearrange to the final stable complex. If this were true, then mutant RNAs that are defective in accelerating SRP•SR complex formation would also be predicted to be defective in stabilizing the early intermediate. To test this model, we reexamined mutations in the universally conserved GGAA tetraloop of SRP RNA (figure 2.5a) that have previously been shown to impair formation of the SRP•SR complex (31, 34).

To this end, eight tetraloop mutants were constructed with various base substitutions: GNRA-type, UNCG-type and mutations that do not form a tetraloop (figure 2.5a). Mutant RNAs were assembled into SRPs with Ffh under the same conditions as wild-type 4.5S RNA, as previous results have shown that mutations in the RNA tetraloop does not affect its ability to bind Ffh (31, 34). Although the effects of these mutations on SRP•SR complex have been characterized before, the earlier study described these effects as a deficiency in forming a stable SRP•SR complex (34). However, kinetic analyses subsequently showed that a stable Ffh•SR complex can be formed without the SRP RNA; the role of RNA is to accelerate the kinetics of complex formation (21). Therefore, we recharacterized these RNA tetraloop mutants to test whether the defects arise from altered kinetics or stability of complex formation.

We first analyzed SRP•SR complex formation using the well-characterized GTPase assay; stimulation of the GTPase activity in the SRP•SR complex provides a

convenient assay for protein-protein interactions. In this assay, the rate constants of two molecular events can be measured. First, at low concentrations of SR, the reaction is

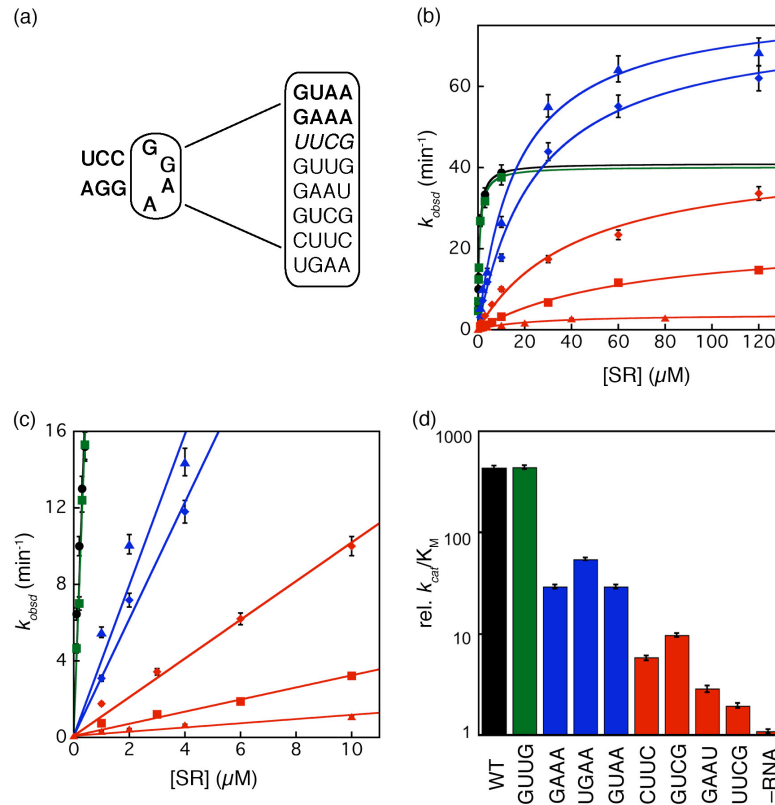


Figure 2.5. Tetraloop mutants in 4.5S RNA slows down the assembly rate of an active SRP•SR complex. (a) List of tetraloop mutants studied in this work. GAAA and GUAA form GNRA type tetraloops (shown as bold); UUCG forms a UNRG type tetraloop (shown as italics); GUUG, GAAU, UCGA, CUUC and UGAA do not form a tetraloop (shown as normal). (b and c) Tetraloop mutants in the 4.5S RNA were classified into three classes based on the severity of defects in SRP-SR association (refer to the classification and color-coding in table 1). The GTPase reaction rate constants were measured and analyzed as described in Methods using 100 nM SRP and 100 microM GTP [wild-type (●), GUUG (■), UGAA (▲), GAAA (◆), GUCG (◇), UUCG (■), and no RNA (▲)]. The initial linear portion of (b) are expanded in (c) to show the difference in k_{cat}/K_M of the various RNA mutants. The values of k_{cat}/K_M and k_{cat} for each RNA are listed in Table 1. (d) Comparison of k_{cat}/K_M values for the various RNA mutants. Data were from figure 2.5c.

rate-limited by SRP-SR association to form an activated SRP•SR complex. Therefore the slope of the initial linear portion of the concentration dependence, which represents the

reaction: $\text{SRP} + \text{SR} \rightarrow \text{products}$ (k_{cat}/K_M), is equal to the rate constant for formation of a stable, active complex. Second, at saturating protein concentrations, the reaction is rate-limited by a different step, the activated GTP hydrolysis after a stable $\text{SRP}\cdot\text{SR}$ is formed. Therefore, the rate constant at saturating FtsY concentrations, k_{cat} , represents the rate constant of GTP hydrolysis from the activated $\text{SRP}\cdot\text{SR}$ complex. Most of the tetraloop mutants show defects in the rate of complex formation (k_{cat}/K_M , figure 5b-d and Table 2.1). Moderate mutants GAAA, UGAA, and GUAA exhibit 8 – 15 fold defects (blue) and severe mutants CUUC, GUCG, GAAU, and UUCG exhibit 45 – 224 fold defects (red). GUUG is the only neutral mutant that exhibits no functional defect in this assay (green). In contrast, most of the mutant RNAs do not significantly impair the activated GTPase reaction in the $\text{SRP}\cdot\text{SR}$ complex (k_{cat} , figure 2.5b and Table 2.1), with some mutants exhibiting even higher GTPase activity than wild-type SRP. Only the most severe mutants GAAU and UUCG showed a modest reduction (1.8- and 1.2 fold, respectively) in the stimulated GTPase activity. These data showed that the primary defect of the RNA tetraloop mutants is the slower kinetics to form the $\text{SRP}\cdot\text{FtsY}$ complex.

We also used the FRET assay to independently determine the effect of mutant RNAs on formation of the GTP-dependent $\text{SRP}\cdot\text{SR}$ complex. Consistent with the results from the GTPase assay, mutant SRPs form GTP-dependent complexes with SR much more slowly than wild-type SRP (figure 2.6a). In addition, the FRET assay directly demonstrates that $\text{SRP}\cdot\text{SR}$ complexes can be formed with the mutant RNAs, given that sufficient time is provided to allow complex formation.

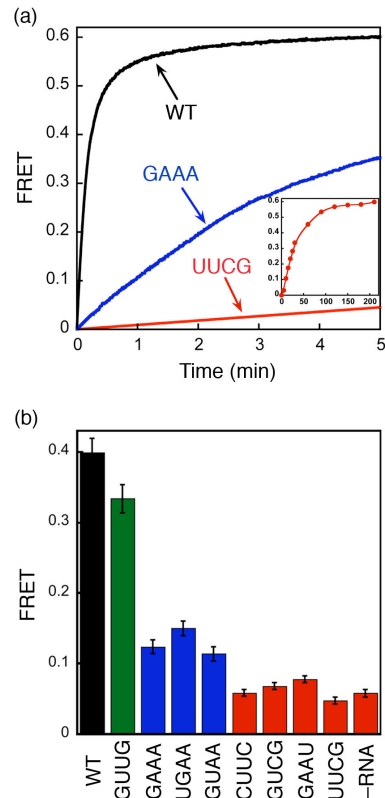


Figure 2.6. FRET measurement shows the deficiency in SRP-SR complex formation caused by 4.5S RNA tetraloop mutants. (a) Time course for formation of the GTP-dependent complex in the presence of different RNA mutants. The inset shows the data over a longer time course with the UUCG mutant (time scale in minutes). 0.5 microM SRP (2 microM SRP for UUCG mutant) and 2 microM SR (10 microM SR for UUCG) were used in the experiment in the presence of 100 microM GppNHp. (b) FRET measurement of the extent of formation of the GTP-independent complex with various 4.5S RNA mutants. 4 microM SRP and 16 microM SR were incubated without GppNHp.

We then tested whether the mutant RNAs can allow formation of the GTP-independent early intermediate using the FRET assay (figure 2.6b). The severe mutants GAAU, CUUC, GUCG, and UUCG, which cause the most deleterious defect on the assembly rate of the GTP-dependent SRP•SR complex, also severely block the formation of the GTP-independent early intermediate, with the observed FRET efficiency similar to that in the absence of 4.5S RNA (figure 2.6b, red). Slightly higher FRET efficiencies are observed with moderate mutants UGAA, GUAA, and GAAA (blue), indicating partial

formation of the GTP-independent early intermediate at the concentration used in this experiment. In contrast, the neutral mutant GUUG (green) formed the GTP-independent complex as efficiently as the wild type SRP. Due to the very weak affinity of the GTP-independent complex formed by the mutant RNAs (>50 μM), saturation could not be reached in equilibrium titration experiments to measure the stabilities of these complexes. Nevertheless, the results in figure 2.6b show that the GTP-independent complex is substantially destabilized by mutations in the tetraloop of the 4.5S RNA. Further, there is a strong correlation between the defects of RNA mutants in stabilizing the GTP-independent early intermediate and their defects in accelerating the assembly rate of the GTP-stabilized, final SRP•SR complex (cf figure 2.6b vs 2.5d).

If stabilization of the early intermediate and efficient SRP•SR complex formation are essential for protein targeting, then the mutant RNAs would be predicted to also impair the protein targeting reaction. To test this notion, we measured the efficiency of protein targeting mediated by the mutant RNAs using a heterologous, co-translational protein targeting assay based on the model SRP substrate preprolactin (pPL) (10, 44). As shown in figure 2.7, most of the mutant RNAs also exhibit translocation defects. The severe mutants (red), which impair complex formation by over 50 fold, completely block pPL translocation. The moderate mutants (blue), which reduce the SRP-SR interaction kinetics by about 15 fold, caused a more modest (~20%) reduction in translocation efficiency. The small translocation defect caused by the moderate mutants is presumably due to the limited sensitivity of this targeting assay, as it can detect translocation defect only when the SRP-SR interaction is reduced by more than 20 fold (10). In contrast, the neutral mutant GUUG does not significantly affect protein translocation. Thus there is

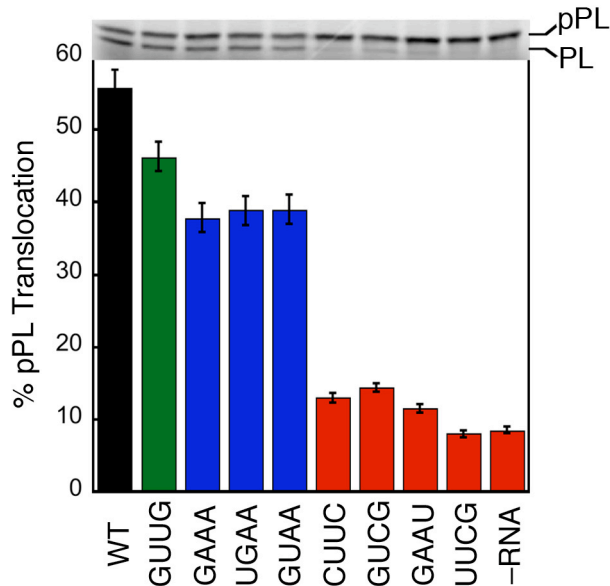


Figure 2.7. Tetraloop mutants impair the co-translational translocation of pre-prolactin. The translocation efficiencies were determined and analyzed as described in Methods. Top panel shows the SDS-PAGE analysis of the translocation of ^{35}S -labeled prolactin. pPL and PL indicate the precursor and mature form of prolactin.

also a good correlation between the translocation defect and the degree to which complex formation is blocked by each mutant RNA (cf. figures 2.5d, 2.6b, and 2.7; see also Table 2.1).

2.4 Discussion

In this study, we developed a highly sensitive, real time FRET assay that allows us to detect a transient, GTP-independent early intermediate during assembly of a stable SRP•SR complex. This demonstrates that SRP•SR complex assembly is a complex multi-step process. Intriguingly, this early intermediate is substantially stabilized by the 4.5S SRP RNA, and there is a strong correlation between the abilities of mutant RNAs to stabilize this early intermediate and their abilities to accelerate the assembly of the stable SRP•SR complex. This led us to propose a new model in which the SRP RNA exerts its

catalytic effect on SRP•SR complex assembly through stabilizing a transient intermediate, thereby allowing it more dwell time to rearrange into the GTP-stabilized final complex. The presence of this additional conformational step provides another potential point for regulation in the protein targeting reaction.

Previous studies have established that GTP or non-hydrolyzable GTP analogues are required for formation of a stable SRP•SR complex, but no complexes have been observed in the absence of GTP (21, 29, 45-47). In this study, FRET provides a highly sensitive assay that allows us to observe an unstable SRP•SR complex in solution that can be formed independently of GTP. Only Mandon et al. have reported a mammalian SRP•SR complex formed in GDP in surface-resonance measurements (42). This complex was not observed in solution previously, presumably because previous studies have relied on gel filtration analysis (20) or the use of tryptophan fluorescence (21, 29, 48). Gel filtration chromatography can only observe kinetically stable complexes but will not be able to detect a more transient complex. Tryptophan fluorescence relies on a late conformational change in FtsY that accompanies complex formation (21), but could miss earlier steps. In contrast, the FRET assay is able to detect transient complexes, because FRET signal relies only on the distance approximation and relative orientation of the donor and acceptor fluorophores on the two proteins. We also showed that the FRET value is different for the GTP-independent complex from the stable, GTP-dependent complex; thus these two complexes have different conformations. Finally, this assay allows us, for the first time, to quantitatively evaluate the contribution of the γ -phosphate group to complex stability. The presence of the γ -phosphate of GTP stabilizes the SRP•SR complex by over 250 fold; the actual interaction energy of the proteins with the

g-phosphate group is presumably larger, as a significant amount of the interaction energy has to be used to induce conformational changes in the complex(9, 20).

For the SRP-subfamily of GTPases, the structural difference between the GppNHp-, GDP-, and apo-proteins is rather minimal (25, 27, 49-51). It is therefore reasonable to suspect that the conformation of the GTP-independent complex can also be adopted by GTP-bound SRP and SR. Here we provide several lines of evidence that strongly suggest that the GTP-independent complex represents an intermediate on the pathway to formation of the final, stable complex by GTP-bound SRP and SR. First, the time course for complex formation in the presence of GppNHp exhibits bi-phasic kinetics indicative of a two-step process, and the first kinetic phase agrees well with the kinetics for formation of GTP-independent complex. Second, the 4.5S RNA is shown to thermodynamically stabilize the GTP-independent complex and also accelerate formation of a GTP-stabilized complex. This observation is consistent with the classical criterion for an on-pathway intermediate: stabilization of an on-pathway intermediate should accelerate the reaction to form the final product. In contrast, if the GTP-independent complex were off-pathway, then stabilizing this complex would be expected to inhibit formation of the GTP-dependent complex. Together, these observations provide strong evidence that the GTP-independent complex is an early intermediate that precedes a GTP-dependent rearrangement to form the final, GTP-dependent complex. The omission of GTP provides a convenient means to isolate this intermediate by preventing the subsequent conformational rearrangements, thereby characterizing its kinetic, thermodynamic, and structural properties and its roles in the protein targeting reaction.

Previously, mutational analysis of the SRP•SR complex have isolated multiple classes of mutant GTPases that each block a different stage during the SRP-SR interaction: class I mutants are defective in complex formation; class II mutants primarily block reciprocal GTPase activation; class III mutants impair both steps; and class IV mutants specifically affect activation of one GTPase in the complex (9). The results with these mutants suggest that during the SRP-SR interaction, complex formation and activation of GTP hydrolysis in the individual GTPases are discrete and separable steps. Our results here further showed that assembly of a stable complex is also a multi-step process that involves an additional GTP-independent early intermediate. Together, these results emphasize the dynamic nature of the SRP-SR interaction. The fact that this early intermediate is much less stable than the previously characterized complexes, and that the class I mutant SR (G455W), which blocks formation of a stable complex, does not affect the formation of the early intermediate (figure 2.S3), indicates that the early intermediate precedes formation of the closed complex.

The model in figure 2.8a describes the multiple steps during the SRP-SR binding and activation cycle. The free SRP and SR, predominantly in an inactive, *open* conformation, quickly associate with one another to form a transient, GTP-independent early intermediate (figure 2.8a, step 1). Interactions of both proteins with the GTP γ -phosphate allow this complex to rearrange into a stable closed complex (step 2). Activation of GTP hydrolysis in the complex requires an additional local rearrangement of the conserved insertion box domain loops from both SRP and SR that precisely aligns the catalytic residues in the loop with respect to both GTP molecules (step 3). GTP

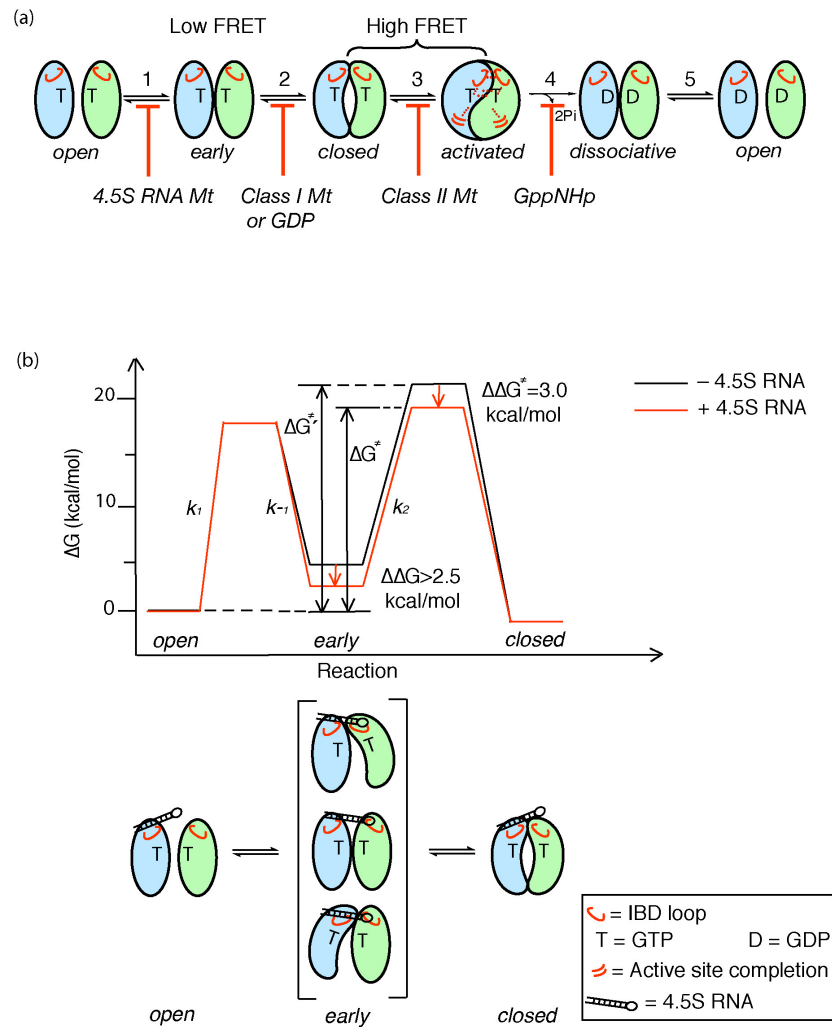


Figure 2.8. Multiple conformational changes during SRP-SR complex formation and activation. (a) SRP and SR GTPases form an early GTP-independent intermediate that exhibits a low FRET (step 1). In the presence of GTP, early rearranges to a more stable, *closed* complex that exhibits a high FRET (step 2). Additional rearrangements in the catalytic loops activate GTP hydrolysis (step 3). GTP hydrolysis drives the dissociation of the SRP•SR complex (steps 4 and 5). Each step can be blocked using specific mutants or nucleotides. 4.5S RNA tetraloop mutants block formation of the early intermediate. Class I mutants of SR (9) or GDP blocks formation of a *closed* complex. Class II mutants on SRP or SR (9) block the rearrangement that activates GTP hydrolysis. GppNHp blocks the chemical step. (b) top panel: free energy profile for the SRP-SR interaction in the absence (black) and presence (red) of the 4.5S RNA for a standard state

of 200 nM. Activation energies were calculated from the observed association and dissociation rate constants using $\Delta G = -RT \ln(kh/k_bT)$, where $R = 1.987 \text{ cal K}^{-1} \text{ mol}^{-1}$, $-h = 1.58 \times 10^{-37} \text{ kcal s}^{-1}$, $k_b = 3.3 \times 10^{-27} \text{ kcal K}^{-1}$, and $T = 298\text{K}$. The relative energies of the different complexes were calculated from the observed equilibrium stabilities using $\Delta G = -RT \ln K$. The 4.5S RNA stabilizes the early intermediate (in bracket) by $> 2.5 \text{ kcal mol}^{-1}$, and the overall activation energy is subsequently lowered by $\sim 3 \text{ kcal mol}^{-1}$. ΔG^\ddagger and $\Delta G^{\ddagger'}$ defines the overall activation energy for forming the GTP-stabilized complex with and without RNA, respectively. The bottom panel depicts a physical picture of how the 4.5S RNA exerts its effect on the SRP-SR interaction as described in the text.

hydrolysis then generates a GDP-complex (step 4), which quickly disassembles due to its low kinetic stability (step 5).

Notably, the early intermediate formed in the first step is significantly stabilized by the 4.5S SRP RNA. Unlike the purely kinetic effect of this RNA on formation of the stable SRP•SR complex (i.e., both complex formation and disassembly is accelerated by the same 200 – 400 fold without affecting the equilibrium stability of the complex) (21, 29), the RNA *thermodynamically* stabilizes the early intermediate. Further, mutations in the conserved tetraloop of the 4.5S RNA are defective in stabilizing the early intermediate, and this defect strongly correlates with the defect of these RNA mutants in accelerating formation of the final, stable SRP•SR complex. Judging from the FRET efficiency of the GTP-independent intermediate in the absence of the RNA, we estimate that the RNA exerts a >60 fold stabilizing effect on this intermediate; this effect accounts for a large part of the ~ 200 fold acceleration of SRP-SR complex assembly by the RNA.

These data allow us to propose a new model for how the 4.5S RNA catalyzes both the association and dissociation between SRP and SR (figure 2.8b). We propose that the early intermediate, although forms quickly, does not have sufficient contacts between the two proteins and thus disassembles just as quickly. The 4.5S SRP RNA, by stabilizing the early intermediate, could provide this intermediate a longer lifetime during which

each protein searches the conformational space and attempts to rearrange to the correct conformation for interacting with each other (figure 2.8b lower panel). The subsequent rearrangement of the early intermediate to the closed complex is the rate-limiting step for formation of a stable SRP•SR complex (figure 8b, DG^\ddagger and $DG^{\ddagger'}$ represents the free energy barrier for formation of the final complex with and without the RNA, respectively). Even if the RNA do not provide additional transition state stabilization for the early \rightarrow closed rearrangement and the same barrier remains for this rearrangement with or without the RNA present, the overall energy barrier for formation of the stable complex is reduced, thus leading to an accelerated assembly rate (figure 2.8b). This model explains how the SRP RNA accelerates assembly of the Ffh•SR complex without affecting its equilibrium stability (21). Several previous models have been proposed to account for the catalytic effect of the RNA by suggesting that the RNA preorganizes the conformation of Ffh to allow a better interaction with SR; however, such models predict that the stability of the Ffh•SR complex would also be increased by the SRP RNA and are not consistent with experimental data.

Although we provide here an energetic model to explain the catalytic role of the 4.5S RNA, the structural origin of this effect remains to be determined. Most likely, the SRP RNA provides a transient tether that holds the two GTPases together upon their initial encounter (figure 2.8b). This tether is broken after rearrangement to the final stable SRP•SR complex since the RNA does not stabilize this stable complex (21), and as such, it has been difficult to identify these transient interactions that the RNA makes with the GTPase domains. Since the thermodynamic stability of the early intermediate directly affects the overall energy barrier of the assembly reaction instead of

characterizing the transition state, we can conveniently characterize the structural and energetic properties of the early intermediate to identify molecular interactions made by the 4.5S RNA to exert its catalytic role.

The presence of the early intermediate and an additional conformational rearrangement required to form the *closed* complex provides an additional potential point for regulation in the protein targeting reaction. In solution, the initial collisional encounter of the SRP and SR leads to a transient and unstable early intermediate that would not accumulate under cellular conditions. In the presence of spatial and temporal cues such as cargo binding and membrane localization, it is possible that the kinetic and thermodynamic stability of this early intermediate and its subsequent rearrangement can be altered and serves to coordinate the proper binding and release of cargo during the protein targeting reaction.

Table 2.1. Summary of mutational effects of tetraloop mutants in the 4.5S RNA. Three classes of mutants are classified based on the severity of the defect as defined in the text.

Tetraloop Mutant	k_{cat}/K_M , rel*	Translocation Efficiency	k_{cat} (min^{-1})	FRET
Wild Type	439	55%	40.9	0.40
GUUG	439	46%	38.7	0.34
GAAA	29.2	37%	76.4	0.12
UGAA	54.9	38%	81.9	0.15
GUAA	29.2	38%	80.6	0.11
CUUC	5.8	12%	35.8	0.06
GUCG	9.8	14%	44.3	0.07
GAAU	2.9	11%	23.0	0.08
UUCG	1.9	8%	33.8	0.05
No RNA	1	8%	3.8	0.05

* Relative value of k_{cat}/K_M compared to that of the no-RNA reaction.

2.5 Materials and Methods

2.5.1 Material

Escherichia coli Ffh, FtsY and 4.5S RNA were expressed and purified using established procedures (29). Mutant proteins and RNAs were constructed using QuickChange procedure (Stratagene, La Jolla, CA), and were expressed and purified by the same procedure as that for wild-type proteins and RNAs. Fluorescent dyes DACM and BODIPY-FL were purchased from Invitrogen (Carlsbad, CA).

2.5.2 Fluorescence labeling

Single-cysteine mutants of Ffh and FtsY were labeled with maleimide derivatives of coumarin and BODIPY-FL, respectively. Protein was dialyzed in labeling buffer [50 mM KHEPES (7.0), 300 mM NaCl, 2 mM EDTA] and treated with 2 mM TCEP to reduce the disulfide bonds. The labeling reaction was carried out using a five fold excess of dye over protein for over 2 hours at 4 °C, and stopped by adding 2 mM DTT. Excess dye was removed by gel filtration using Sephadex G-25 (Sigma, CA). Absorbance of DACM ($\epsilon_{363} = 27,000 \text{ M}^{-1} \text{ cm}^{-1}$) and BODIPY-FL ($\epsilon_{504} = 79,000 \text{ M}^{-1} \text{ cm}^{-1}$) was used to determine the concentration of labeled protein. The efficiency of labeling reaction was evaluated using

$$I = \frac{\text{moles of dye}}{\text{moles of proteins}} \quad (2.1)$$

The efficiency of labeling reaction was typically $\geq 95\%$ for both probes. The background, estimated from the labeling of cysteinless Ffh and FtsY using the same procedure, are less than 3%.

2.5.3 Fluorescence measurement

FRET was determined by steady-state fluorescence measurement on a Fluorolog-3 spectrofluorometer (Jobin Yvon, Edison, NJ). All measurements were carried out at 25 °C in assay buffer [50 mM KHEPES, pH 7.5, 150 mM KOAC, 2 mM Mg(OAc)₂, 2 mM DTT, 0.01% Nikkol] using an excitation wavelength of 380 nm. Fluorescence emission spectra were acquired from 420 to 600 nm. Equilibrium titration or kinetic measurements using FRET were determined by monitoring the fluorescence emission at 470 nm. FRET efficiency (E) is calculated by the relative fluorescence intensities of the donor in the presence and absence of acceptor (eq. 2.2),

$$E = 1 - F_{DA} / F_D \quad (2.2)$$

where F_{DA} and F_D are the fluorescence intensities of the donor measured in the presence and in the absence of acceptor, respectively. F_D was measured using donor-labeled Ffh and unlabeled FtsY. The Förster distance for the donor-acceptor pair coupled to the different positions was experimentally determined to be $R_0 \sim 47 \text{ \AA}$ (52). Fast reactions were measured on a Kintek stop-flow apparatus at 25 °C. The association rate constant for the SRP•SR complex was measured by mixing 2 microM SRP with 4, 8, 15, 25 microM SR in the presence or absence of GppNHp. The observed rate constant (k_{obsd}) is linearly dependent on SR concentration (eq. 2.3) and the slope of the concentration dependence gives the association rate constant, $k_{\text{on}}(21)$.

$$k_{\text{obsd}} = k_{\text{on}} [\text{SR}] + k_{\text{off}}. \quad (2.3)$$

The dissociation rate constant for the GTP-independent complex (k_{off}) was determined by a pulse-chase experiment (29). 2 microM SRP and 8 microM SR were incubated in the absence of GppNHP for 5 minutes to form the SRP•SR complex, then the solution was mixed with equal volume of 400 microM unlabeled SR to drive irreversible dissociation of the complex. The time course of change in donor fluorescence was fit to exponential function (eq 2.4), where F_{obsd} is the observed fluorescence, $F_{t \rightarrow \infty}$ is the fluorescence when reaction reaches equilibrium, and ΔF is the amount of fluorescence change during the experiment.

$$F_{\text{obsd}} = F_{t \rightarrow \infty} + \Delta F \times e^{-k_{\text{off}} t}. \quad (2.4)$$

2.5.4 Translocation assay

Mutant 4.5S RNAs were used to reconstitute SRP with Ffh, and protein targeting efficiency of the mutant SRPs were measured using a heterologous co-translational translocation assay as described (10, 44).

2.5.5 GTPase assay

The GTPase assay to measure the stimulated GTP hydrolysis reaction between SRP and FtsY were carried out and analyzed as described (29).

2.6 Supplemental Figures

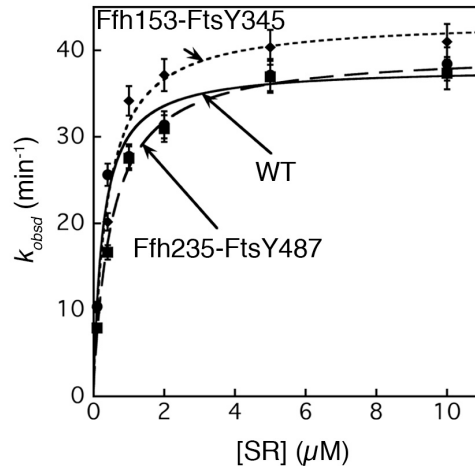


Figure 2.S1. Reciprocally stimulated GTPase activity between SRP and FtsY are unaffected in fluorescently labeled proteins. The reaction rate constants were measured and analyzed as described in Methods using 100 nM SRP and 100 μM GTP. The maximal GTP hydrolysis rate constants at saturating protein concentrations are 37.9, 42.2, and 38.9 min^{-1} for wild-type (solid line), Ffh 153C and FtsY 345C (dotted line), and Ffh 235C and FtsY 487C (broken line), respectively.

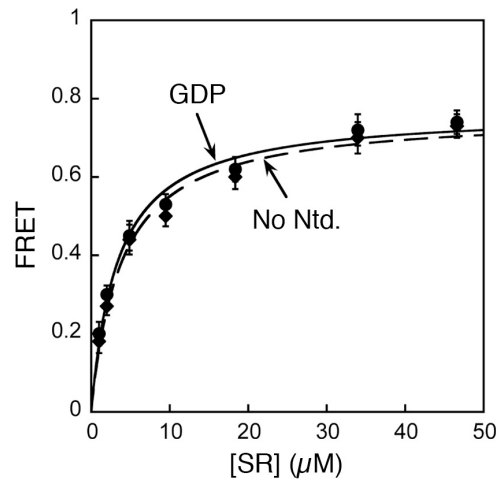


Figure 2.S2. Equilibrium titration of SRP•SR (Ffh 235C and FtsY 487C) complex with 100 μM GDP (●), and without nucleotide (◆). The data were fit to a single binding equation and gave dissociation constants of 3.9 μM (GDP) and 3.6 μM (without nucleotide).

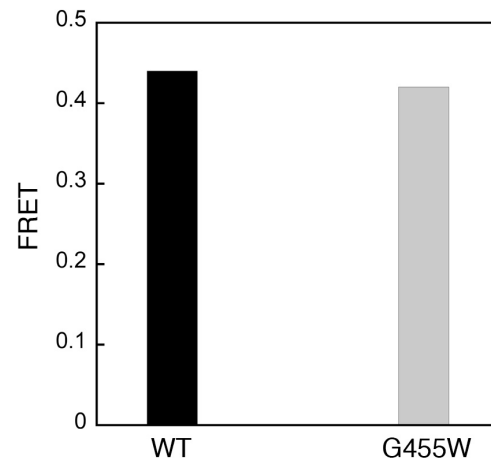


Figure 2.S3. Formation of the GTP-independent complex for wild type SR and a Class I mutant SR G455W (9). FRET values were measured with 4μM SRP and 16μM wildtype or mutant SR in the absence of nucleotides.

2.7 Acknowledgments

We thank members of the Shan laboratory for comments on the manuscript. This work was supported by NIH grant GM078024 to S.S. S.S. was supported by the Burroughs Wellcome Fund career award, the Henry and Camille Dreyfus foundation, the Beckman Young Investigator award, and the Packard and Lucile award in science and engineering. X.Z. was supported by a fellowship from the Ulric B. and Evelyn L. Bray Endowment Fund.

Chapter 3

Dynamics of the Transient Intermediate during SRP-SR Association

A version of this chapter has been prepared for submission.

3.1 Abstract

Interactions between proteins are in the center of biology. Kinetic studies of protein-protein interaction have proposed a mechanism in which proteins initially form a pre-equilibrium transient intermediate along the association pathway that subsequently relaxes to the stable complex. However, the landscape of the transient intermediate that precedes formation of the stable complex is still not well defined experimentally. In this work, we directly visualized the conformational dynamics of the early complex as a transient intermediate during the assembly between two GTPases in the signal recognition particle (SRP) and its receptor (SR) under equilibrium condition. We show that the interaction surface of the early complex shares both similarities and differences with that of the stable complex. In addition, a broad conformational distribution of the early complex allows the free proteins to search optimal routes in the configuration space toward to an efficient stable complex assembly. Interestingly, the dynamics of the early complex actively responds to the external biological cues that the SRP-SR interaction dictates. Collectively, understanding the landscape of the SRP-SR early complex provides a general feature that is shared by the transient intermediate during protein assembly.

3.2 Introduction

Most proteins rely on interacting with one another to carry out their biological functions (1, 53-56). However, unbound proteins often need to change their conformation substantially to form stable complexes. A model that combines both the “induced fit” and the “conformational selection” hypotheses postulates three steps

for the protein-assembly process (57-59). The initial step arises from a diffusing binding event between proteins form a transient intermediate in solution; subsequently, the complementary structures are recognized and selected from the conformational ensemble of the transient intermediate; and last, the intermediates composed of complementary structures reorient into a native, stable complex with a fitted interaction surface. In this model, formation of the transient intermediate is mostly mediated by nonspecific collisions and directional long-range electrostatic interactions; and does not undergo extensive conformational rearrangements in proteins. Although nonspecific and weak, a transient intermediate could give rise to the rate of complex formation because proteins that are loosely held in this intermediate are given time to undergo rearrangements and reorientations to form short-range interactions that are required for the interaction surface of a stable complex.

Despite significant progresses in understanding how the transient intermediate kinetically facilitates the protein assembly (60), direct visualization on the transient intermediate during protein assembly pathway is still much less common. Several studies were reported to visualize the dynamics of the transient encounter complexes that are formed upon collision, but these encounter complexes do not lead to the formation of stable complexes (61, 62). During assembly of a stable complex, the transient intermediate is much more unstable than the stable complex, so it either rearranges into a stable complex or dissociates rapidly. Only a very small population of the intermediate can be captured in an ensemble experiment, and this situation complicates the structural study of the transient intermediate. To understand the conformational dynamics of the

transient intermediate during protein assembly, we choose the interaction between two guanosine triphosphatases (GTPases) in the signal recognition particle (SRP) and the SRP receptor (SR) as a model system because the transient intermediate during the SRP-SR assembly process can be isolated and characterized under equilibrium condition (4, 5).

3.2 Results

SRP and SR GTPases initially associate with one another to form an unstable, transient intermediate named early complex (step 1 in figure 3.1A), and then the early complex undergoes extensive local conformational rearrangements to form the stable complex (step 2 in figure 3.1A). Interestingly, the conformational rearrangements to form the stable complex are largely dependent on the γ -phosphate of the guanosine triphosphate (GTP) molecules that bound to both GTPases. If binding guanosine diphosphate (GDP) instead of GTP, the SRP•SR complex is stalled at the stage of the early complex without further rearranging into the stable complex (figure 3.1A). Taking the advantage of this distinct feature, we could generate an ensemble of early complex by stopping it forming the stable complex. Thus the structural properties of the early complex can be directly characterized in detail under equilibrium condition. In the following experiment, the early complex is formed using GDP; and the stable complex is formed with non-hydrolyzable GTP analogue, 5'-guanylylimido-diphosphate (GMPPNP).

Formation of the transient intermediate is mainly guided by long-range electrostatic interactions and nonspecific collisions within solvent cages; therefore, it is believed that

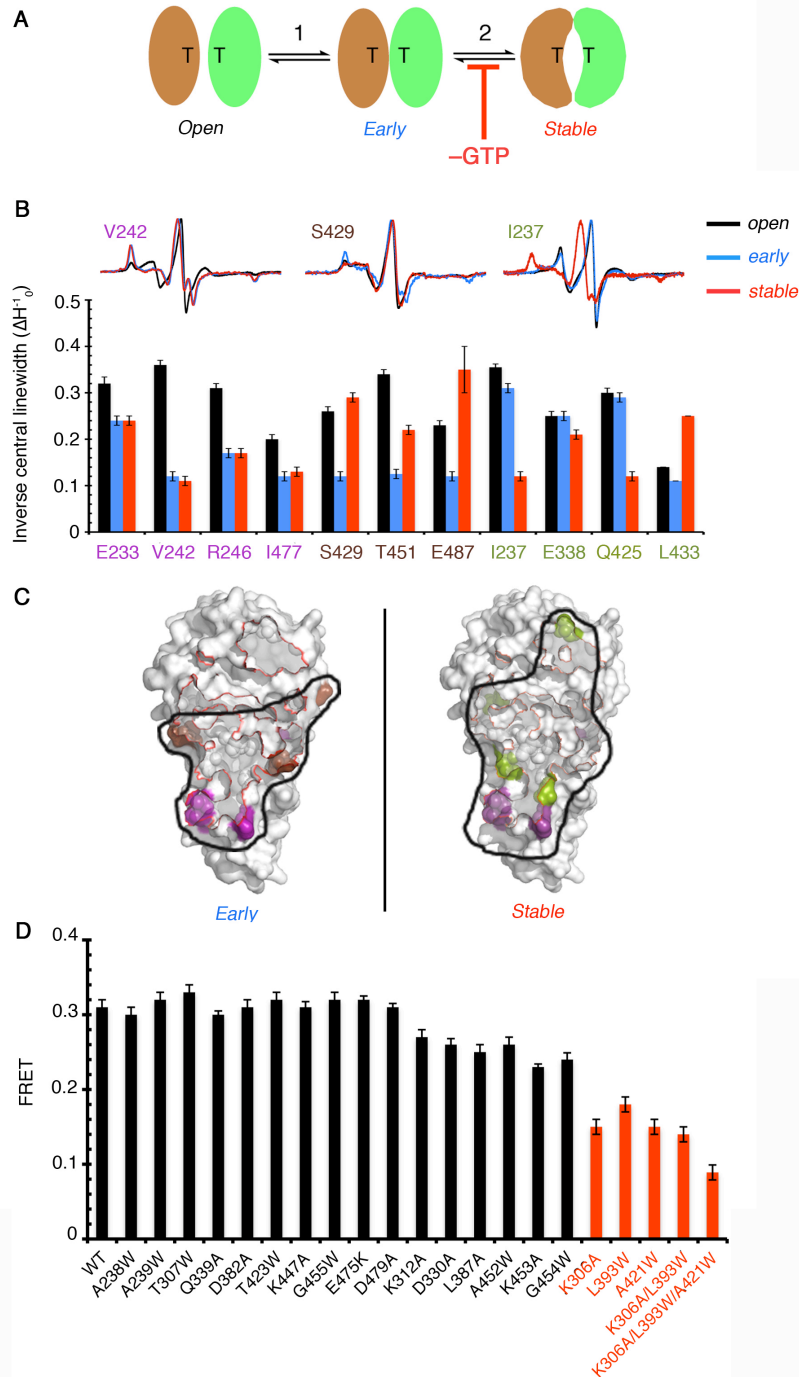


Figure 3.1. The interface of the SRP-SR early complex is both similar to and different from that of the stable complex. **(A)** Schematic mechanism of SRP-SR assembly. Upon directional collision, SRP and SR form a non-specific early complex (step 1), which serves as a transient intermediate that leads to the formation of a stable, specific complex (step 2). Removing GTP from the solution stalls the early complex from evolving into the stable complex. Brown and green denote for SRP and SR, respectively. T denotes GTP. **(B)** The mobility of residues changed upon the formation of either the early complex

(brown), the stable complex (green), or both (purple). (C) Interaction surface of the early and stable complexes mapped by EPR measurements. (D) Mutations that disrupt the formation of the stable complex do not significantly affect the thermodynamic stability of the early complex. Mutations causing moderate defect in the formation of the early complex are highlighted in red.

very few short-range interactions can be made in the intermediate (63). The questions arose are what the interaction surface of the transient intermediate looks like and how different it is from that of the stable complex. To answer these questions, we explored the interaction surface of both the early and stable SRP•SR complexes using electron paramagnetic resonance (EPR) spectroscopy. The strategy was to select the residues to examine whether their mobility was affected by the formation of either the early or the stable complexes. These residues were replaced by cysteines for site-directed spin labeling with nitroxide probe (1-oxy-2,2,5,5-tetramethyl-3-pyrrolyl-3-methyl) methanethiosulfonate (MTSSL). Sites that the nitroxide probe modification does not affect the ability of SR to interact with SRP are selected for EPR measurements. For each individual residue, EPR measurement was carried out to characterize the mobility of the spin-label in the apo-SR (figure 3.1B, black), the early complex (figure 3.1B, blue), or the stable complex (figure 3.1B, red). From the line width of the central resonance and the overall breadth of the spectra along the magnetic field axis, we could derive a qualitative description of the local mobility of the nitroxide probe-labeled SR. If the mobility of the spin label decreases upon complex formation, then the labeled residue is considered to be involved in strong interactions that contribute to form the interface of this complex.

Shown in figure 3.1B, three classes of residues were identified from the EPR measurements. The first class includes four residues that are represented by residue 242

(figure 3.1B and figure 3.S1, purple), in which the apo-SR exhibits restrained EPR spectra with a majority of molecules being mobile. Upon formation of both the early and stable complexes, decreased mobility of the nitroxide probes indicated that these residues were involved in local interactions, suggesting that these residues are engaged in the interface of both complexes. We also identified residues that are involved in the formation of interfaces of either the early complex (figure 3.1B and figure 3.S1, brown) or the stable complex (figure 3.1B and figure 3.S1, green). In either group, mobility of these residues was only affected by the interaction surface of one conformational state but not the other. Summarizing the above results, we were able to obtain a collective view of the interaction surfaces the early (figure 3.1C, left panel) and stable complexes (figure 3.1C, right panel). In the early complex, most contacts between SRP and SR were concentrated in the N/G domain interface and the N domain, whereas most of the G domain made little contribution to the interaction surface. In contrast, the interface of the stable complex covered both G and N domains, consistent to the interaction surface that was shown in the co-crystal structure of SRP-SR stable complex (red line on surface representation in figure 3.1C) (20). Taken together, EPR measurements suggested that the early complex did contain a detectable interaction surface that shared both similarities and differences to that of the stable complex (figure 3.1C).

Based on the above observation, we reasoned that the fact that the early and stable complexes share a common interaction surface would allow us to mutate residues to disrupt the formation of both complexes. To this end, we introduced 24 mutations to the SR protein, and all of them severely blocked the formation of the stable complex (figure 3.1D and figure 3.S2B) (9). The stability of early complex formed with SR mutants was

measured using fluorescence resonance energy transfer (FRET) between coumarin (DACM) labeled SRP C235 and BODIPY-fluorescein (BODIPY-FL) labeled FtsY C487 (4). Whether a mutation was defective in forming the early complex could be derived from the extent of reduction in FRET efficiency compared to that of the wild-type SR at a fixed protein concentration. To our surprise, most of the mutations did not disrupt the formation of the early complex at protein concentrations that we tested (black bars in figure 3.1D). Only three mutations caused moderate reduction in the stability of the early complex by a factor of up to four (red in figure 3.1D and figure3.S2A). A triple mutation including all three positions further destabilized the early complex by only a factor of eight (red in figure 3.1D and figure3.S2A).

The mutagenesis experiments showed that mutations severely disrupting the formation of the stable complex were only marginally defective in forming the early complex, suggesting that these two complexes employed distinct interaction surfaces. This conclusion was seemingly contradictory to what was suggested by the EPR measurements. We then speculated that the early complex did not contain a defined interface like the stable complex did. If the early complex was composed of multiple distributions of conformations and each of them used different interface from one another, then mutations that only disrupted the interface of particular conformations would not affect other conformations that were still bound to maintain the stability of the early complex. In contrast, the stable complex could contain only a few well-defined conformations so mutations that disturbed one population would substantially reduce the stability of the complex.

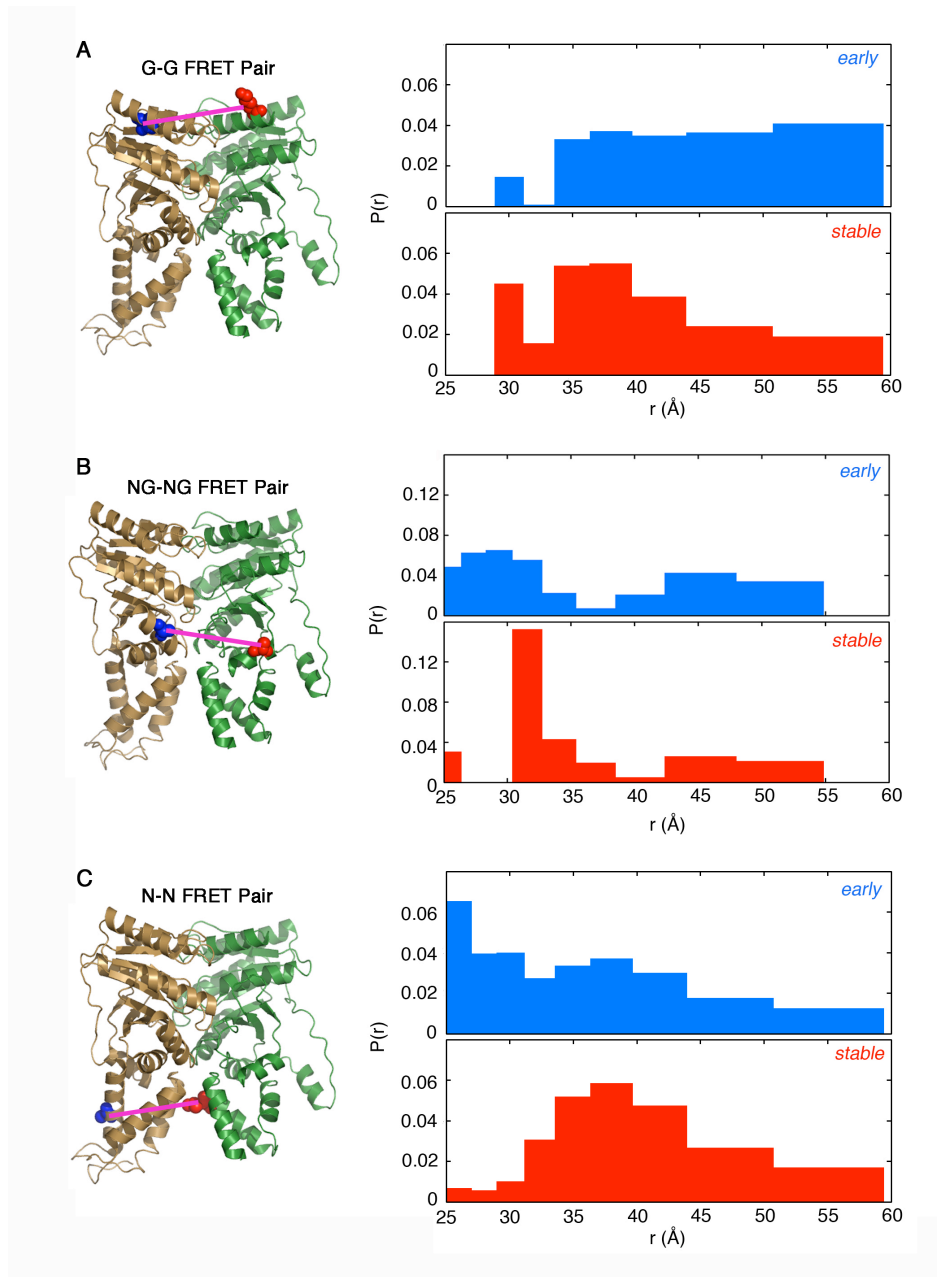


Figure 3.2. The early complex has a more broad conformational distribution than the stable complex. Fluorescence decay kinetics of the donor fluorophore (blue) was measured in the presence of the acceptor fluorophore (red). Distributions of $P(r)$ were derived from the maximal entropy analyses of the TR-FRET kinetics data. Left panel in (A), (B), and (C) shows position of the G-G, NG-NG, and N-N FRET pairs, respectively. Distribution of $P(r)$ was measured for each FRET pair in the pre-formed early complexes (blue) or stable complexes (red) under equilibrium condition. Gold and green proteins are SRP and SR GTPases, respectively.

To test this hypothesis, we carried out time-resolved FRET experiments to measure the distance distribution between a fluorescence donor (DACM) on SRP and an energy acceptor (BODIPY-FL) on SR in an ensemble of the SRP•SR complexes. These measurements provide nanosecond snapshots of donor-acceptor distance distributions of either the early or the stable complex (figure 3.S3) (64). Three different positions were selected to measure distance distributions between the G domains (G-G, figure 3.2A), the NG domain interfaces (NG-NG, figure 3.2B), and the N domains (N-N, figure 3.2C) of both proteins. For all three pairs, the early complex generated more broad distance distributions than the stable complex (figure 3.3 and figure 3.S4, blue vs red). In addition, it is notable that the conformational distribution in the stable complex already existed in the early complex, suggesting that the molecular ensemble of the early complex underwent the conformational sampling to form the stable complex. These observations support the hypothesis that the early complex comprises more conformational populations than the stable complex.

Further, the observed pattern of distance distribution also revealed the process of the early complex assembly. Distance as short as ~ 25 Å was observed for the N-N pair, while the G-G pair generated a ubiquitous distance distribution that had no dominating peaks. This pattern of distance distributions suggested that the formation of the early complex initiated from the close contacts between N-domains of both proteins. We reasoned that these contacts could be originated from the long-range electrostatic interactions that commonly facilitate the formation of an encounter complex. Thus, we calculated the electrostatic surface of the GTPase domains of both the SRP and SR using adaptive Poisson-Boltzmann solver (APBS) (65). The N domain of the SRP contains a

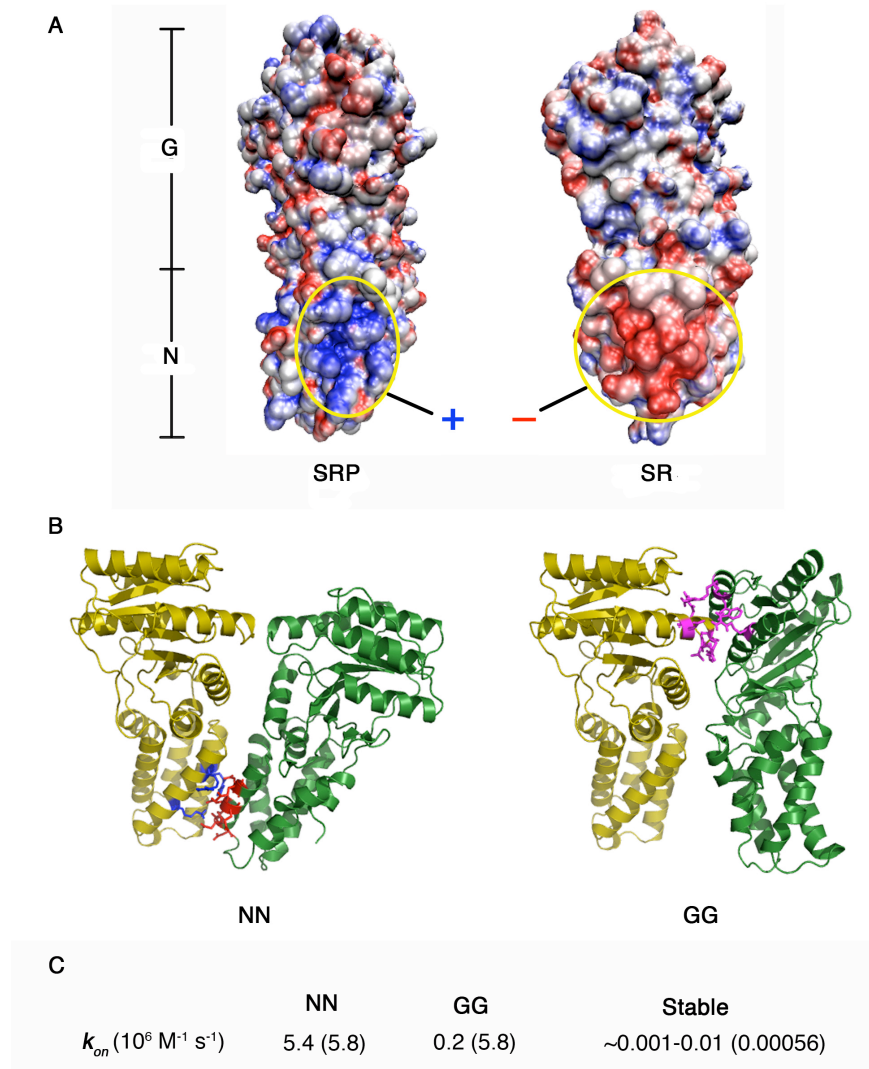


Figure 3.3. The long-range electrostatic interaction between sites with complementary charges drives the formation of the early complex. **(A)** Sites in the N domains of the SRP and SR GTPases contained complementary charges. Blue and red denotes positive and negative charges, respectively. **(B)** Molecular docking simulation generated two groups of conformations (NN and GG) that accounted for the ensemble of the early complex. Gold and green proteins are SRP and SR GTPases, respectively. In the NN conformations, hot spots analyses predicted that the positive residues on the SRP (blue) contacted the negative residues on the SR (red) via electrostatic interaction. In the GG conformations, hot spots analyses predicted that that van der Waals interaction between residues (pink) on the G domains contributed to the formation of the interface. **(C)** Association rate constants derived from the Brownian dynamics calculation were comparable to the experimental measured rate constants (in parentheses).

positively charged patch, whereas that of the SR has complementary negative charges (figure 3.3A). Thus, a general non-specific electrostatic interaction between these two patches could facilitate the assembly of the early complex.

To provide a molecular picture of the early complex, we carried out molecular docking simulation; and the first two highest-ranked groups, denoted as NN and GG, were selected to describe the possible conformations of the early complex (figure 3.3B and figure3.S5). Conformers in the NN group placed N domains of both GTPases adjacent to each other whereas the G domains were apart; and the interface of the NN complexes was consistent to what was identified by EPR spectroscopy (figure 3.1C, left panel). Interestingly, the contact sites in the N domains were composed of the residues bearing complementary charges as identified in APBS calculation, suggesting that the formation of the NN complexes was primarily mediated by a general electrostatic interaction (figure 3.3B, blue and red residues in the left panel). In contrast to the NN group, the GG group contained complexes with G domains contacting one another but N domains being separated; and the interface of the GG complexes were mainly mediated by van del Waals interaction between residues in G domains (figure 3.3B, pink residues in the right panel). As one means to validate the reliability of the docking simulation, we examined the distance distribution between all three FRET pairs using the complexes generated in these two groups. Both groups were needed to produce the distance distributions that were qualitatively comparable to the experimental measurements (figure 3.S7 vs figure3.2, blue), suggesting that both the NN and GG conformations existed as possible conformational states of the early complex. In addition, we also collected evidence suggesting that the NN complexes were more likely to be the

dominant population in the early complex under the equilibrium condition. First, residues that were affected in the EPR measurements resided in the interfaces of complexes in both groups but primarily the NN group (figure 3.S6). Second, the theoretically estimated associate rate constants for early complex formation based on the NN complexes agreed well to what were measured experimentally, whereas, the GG complexes produced the association rate constant that was slower than the experimental value by a factor of thirty (figure 3.3C).

We next ask whether the conformational dynamics of the SRP-SR early complex responds to the biological cue that it dictates. Since the interaction between the SRP and SR GTPases regulates the co-translational protein targeting process, we speculated that the cargos for SRP could alter the dynamics of the early complex. To this end, we measured the conformational distribution of the early complex in the presence of an authentic SRP cargo, RNC_{FtsQ} , a translating ribosome with the first 74 amino acids of the stalled FtsQ nascent chain (5). Early complex was incubated with RNC_{FtsQ} to form the early targeting complex; subsequently the TR-FRET experiment was carried out to obtain the distance distributions of three different FRET pairs. Notably, cargo substantially narrows the distance distribution of all measured FRET pairs. Instead of being broad, bipolar distance distributions of the early complex were observed in the presence of RNC_{FtsQ} (figure 3.4A and figure3.S8). These observations suggested that the cargo modulated the dynamics of the early complex into a limited configuration space in which the success rate of selecting complementary structures were increased, providing additional explanation to why cargos could kinetically accelerate the formation of the stable complex (5).

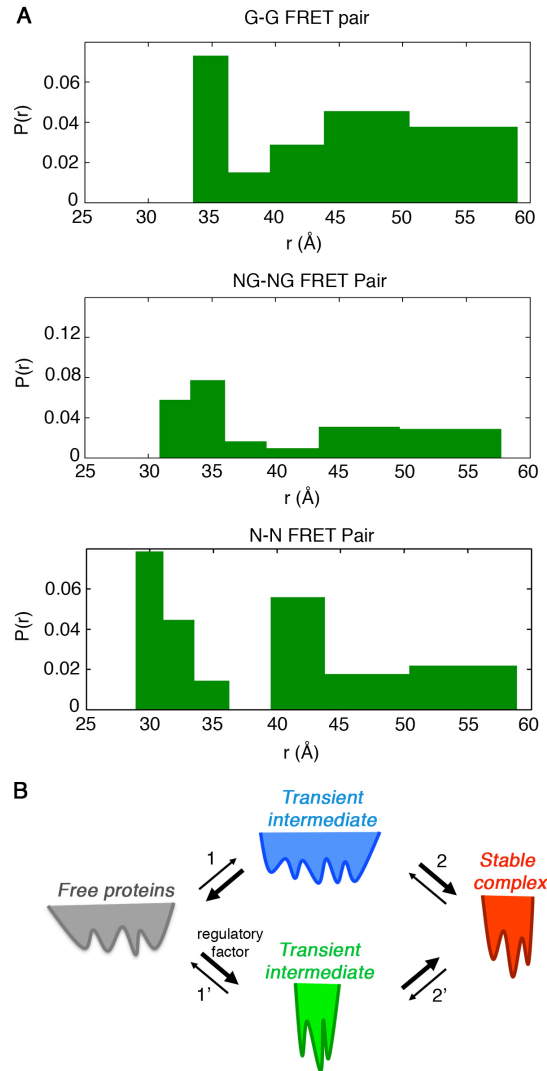


Figure 3.4. SRP-dependent cargo confined the conformational distribution of the early complex. **(A)** Distances between the FRET pairs were measured in a preformed early targeting complex in the presence of RNC_{FtsQ}. Distributions of $P(r)$ were extracted from the maximal entropy analyses of the TR-FRET kinetics data. **(B)** A schematic diagram of energy landscapes of the transient intermediate and stable complex during protein-protein assembly processes. The presence of an external factor changes the landscape of the transient intermediate to alter the thermodynamic and kinetic framework of the protein-protein assembly.

3.4 Discussion

Our work suggests that the ensemble of the early complex is a collection of various distinct conformational states (blue in figure 3.4B). In this ensemble, the early complex

samples through a broad range of the conformational space to seek optimal conformations that are efficient to produce short-range interactions for formation of the stable complex (step 2 in figure 3.4B), which contains a restrained conformational distribution (red in figure 3.4B). More importantly, the conformational distribution of the early complex could respond to the cargos that SRP needs to deliver via the SRP-SR interaction (step 1' and green in figure 3.4B), suggesting that the structural dynamics during protein-protein interactions could play a regulatory role to the biological processes that they dictates. The observed features of the SRP-SR early complex during the formation of the stable complex could represent general features that are shared by the transient intermediates during protein assembly.

The direct visualization of the transient intermediate during protein assembly adds to a growing collection of examples to support the notion that the intermediate contains a conformational ensemble in which the complementary structures are selected for further induced fit (figure 3.4B). The efficiency of the stable complex assembly is more affected by the possibility that the complementary structures are successfully selected than by the rate constants of the intermediate assembly (54). In addition, external regulatory factors can also affect the conformational landscape of the transient intermediate to alter the thermodynamic and kinetic framework of the protein assembly. Since the transient intermediate is possibly formed prior to the free proteins undergo conformational rearrangements; these conformational distributions could be well built in the innate conformational fluctuations of the free proteins (gray in figure 3.4B) (58). Upon formation of the transient intermediate, the conformational fluctuations in the free protein can be further reduced to expedite the formation of the stereospecific and stable complex.

This mechanism can be viewed as a funnel-shaped binding model in which many possible routes to approach the stable complex can be selected from the conformational distributions within the ensemble of the transient intermediate.

3.5 Materials and Methods

3.5.1 Materials

The *E. coli* SRP and SR GTPases (Ffh and FtsY, respectively), and 4.5S RNA were expressed and purified as described previously (4, 66). FtsY (47-497) was used in all the fluorescence and EPR measurements. The abilities of FtsY(47-497) to interact with SRP and respond to the cargo are similar to those of full length FtsY. Single cysteine mutants of Ffh and FtsY and stable complex defective mutants of FtsY were constructed using the QuickChange mutagenesis procedure (Stratagene). All mutants were expressed and purified using the same procedure as that for the wild-type proteins. Fluorescent dyes N-(7-dimethylamino-4-methylcoumarin-3-yl)maleimide (DACM) and BODIPY-FL-N-(2-aminoethyl)-maleimide were from Invitrogen.

3.5.1.1 RNC_{FtsQ} purification

Homogeneous RNC_{FtsQ} were generated from In vitro translation reactions using membrane free cell extract prepared from MRE600 cells, and RNC_{FtsQ} were purified through affinity chromatography and sucrose gradient centrifugation as described previously (5, 67). Purified RNC_{FtsQ} can serve as functional cargos in protein targeting reaction as they can bind SRP, trigger-factor, and secYEG translocon complex. In quantitative assays, purified RNC_{FtsQ} exhibit the same affinity for SRP as those measured with RNCs that do not contain an affinity tag (68).

3.5.1.2 Fluorescence labeling

For FRET measurements, DACM and BODIPY-FL were used to label single-cysteine mutants of Ffh and FtsY, respectively, as described previously (4). Labeled

protein was purified as described (4), and the efficiency of labeling was typically $\geq 95\%$ with a background of $< 5\%$.

3.5.1.3 Spin labeling

All single cysteine FtsY mutants, in 20 mM HEPES pH8.0 buffer with 150mM NaCl and 2mM EDTA, were incubated with 10 molar excess of dithiothreitol (DTT) at room temperature for 1-2 h to reduce any disulfide cross-linking. DTT was removed from protein by passing through gel filtration column. In the labeling reactions, a 3- to 5 fold molar excess of spin label (1-oxy-2,2,5,5-tetramethyl-3-pyrrolyl-3-methyl)methanethiosulfonate (MTSSL) (Toronto Research Chemicals, Toronto, Canada) was added to the argon degassed protein sample ($\sim 100 \mu\text{M}$). The spin-label reactions were carried out at room temperature in the dark for 2-3 h. Excess MTSSL was removed by gel filtration. The labeling efficiency was determined by EPR measurements using a TEMPO calibration curve (Bruker user manual). The typical efficiency of spin label is usually $> 80\%$; and a $< 5\%$ background labeling is observed with cysteine-less wild-type protein labeled following the same protocol. Only functional labeled FtsY mutants similar to wild-type enzymatic activity were used for subsequent EPR measurements.

3.5.2 Experimental strategy

In order to directly visualize the transient intermediate along the association pathway between SRP and SR, we used a combination of different techniques, including electronic paramagnetic resonance (EPR), steady-state FRET, mutagenesis, and time-resolved fluorescence energy transfer (TR-FET). EPR technique was used to explore the interaction surface of both the early and the stable complexes. Mutagenesis and steady-state FRET assay were used together to determine the equilibrium stability of the early

complex formed with different SR mutants. The TR-FET technique was used to directly measure the distance distribution between the donor molecule on SRP and acceptor molecule on SR. By collecting the distance distribution between donor and acceptor at different positions on both SRP and SR, we can characterize the conformational dynamics of the early and stable complexes in the configuration space. Taken together, these techniques enable us to directly characterize the structural dynamics of the early and stable complexes under equilibrium condition.

3.5.3 Electron paramagnetic resonance (EPR) measurements

EPR measurements were carried out to determine the local mobility of 9 spin label molecules in the form of apo-FtsY, the early complex or the stable complex. For FtsY in apo-form, 75-100 microM spin-labeled FtsY was used to obtain the EPR spectra. The early complex was formed by mixing 30 microM spin-labeled SR with 90 microM SRP in the presence of GDP. Based on the binding affinity of the early complex (K_d values of 4-10 μ M) (4), more than 90% of labeled FtsY is in complex form with SRP in the state of the early complexes. The stable complex was formed by mixing 30 microM spin-labeled-SR with 60 microM SRP in the presence of the GTP analogue 5'-guanylylimido-diphosphate (GMPPNP). More than 99% of labeled FtsY is in complex form with SRP in the state of the closed complex according to the reported K_d values of the stable complex (\sim 16 nM) (4).

EPR spectra were acquired with a 9.4 GHz (X-band) Bruker EMX EPR spectrometer equipped with an ER 4119HS cavity at 20-23 °C. In order to generate the local mobility of spin labels, 40% glycerol was added in all samples to eliminate the motion of protein global tumbling. Since the center line width (ΔH_0) of EPR spectra

stays the same at microwave powers of 0.2, 2, or 5 mW, all scans were carried out using microwave power of 5 mW to improve the signal-to-noise ratio. The modulation amplitude was set at 2 gauss and magnetic field sweep width was set as 100 gauss. For each sample, an averaged spectrum was obtained from approximately 32 to 64 scans and the background signal was subtracted.

During EPR measurements, the energy absorption process takes place when the unpaired electron in the probe transits from the ground state to the excited state. EPR signals can be observed when the scanning magnetic field is in resonance with the electron spin frequency, akin to the mechanism in nuclear magnetic resonance phenomenon. It has been shown that the center signal is sensitive to both the local environment and secondary structure. Thus we used the central line width (ΔH_0), which is measured from peak to peak of the center signal (figure 3.1B), as a way to characterize residue mobility. Collectively, the mobility measurements of a set of labeled residues can be used to describe dynamics of the interested area.

3.5.4 Steady-state fluorescence measurements

Our previous work showed that the rate constant of early complex formation is rapid and the K_d value of this complex is 4-10 μM . We therefore measured the relative equilibrium stability of the early complex formed by different SR mutations using the FRET assay at a steady-state condition. All measurements were carried out at 25 °C in assay buffer [50 mM KHEPES, pH 7.5, 150 mM KOAc, 2 mM $\text{Mg}(\text{OAc})_2$, 2 mM DTT, 0.01% Nikkol] on a Fluorolog-3-22 spectrofluorometer (Jobin Yvon, Edison, NJ). FRET measurements were carried out using an excitation wavelength of 380 nm and an emission wavelength of 470 nm. FRET efficiency was calculated as described.

To compare the relative equilibrium stability of the early complexes formed with different SR mutants, 4 or 20 microM acceptor labeled SR-mutants were incubated with 1 microM donor-labeled SRP in the absence of GTP or GTP analogue. Equilibrium is established upon manual mixing. FRET efficiency was calculated as described. For representative mutants, equilibrium titrations were carried out in the presence of a small, fixed amount of donor-labeled SRP and increasing amounts of acceptor-labeled SR in the absence of GTP or GTP analogues. FRET efficiency was plotted as a function of SR concentration ($[SR]$). The data were fit to Eq. (3.1),

$$E = E_1 \times \frac{[SR]}{K_d + [SR]} \quad (3.1)$$

in which E_1 is the FRET value (end point) when all the SRP are bound to SR, and K_d is the equilibrium dissociation constant of the early complex.

3.5.5 Time-resolved fluorescence energy transfer (TR-FET) measurements

TR-FET experiments were carried out to measure the distance distribution between the donor (DACM) on SRP and acceptor (BODIPY-FL) on SR. Donor-only measurement was carried out in the presence of 5 microM or 1 microM DACM-labeled SRP for the early and stable complexes, respectively. For the early complex, 5 microM DACM-labeled SRP and 50 microM BODIPY-FL-labeled SR were mixed together in the presence of GDP. For the stable complex, 1 microM DACM-labeled SRP and 8 microM BODIPY-FL-labeled SR were mixed in the presence of GMPPNP. Formation of both complexes was complete after a 20-minute incubation at room temperature at dark.

The time-resolved DACM fluorescence-decay kinetics measurements were carried out with a picosecond streak camera (C5680; Hamamatsu Photonics) in the photon-counting mode (69, 70). The excitation wavelength was set at 355 nm from a

third harmonic of a regeneratively amplified mode-locked Nd-YAG laser (pulsewidth is ~ 15 ps) (Vanguard, Spectra-Physics). A band-pass filter of 450 ± 5 nm was used as the emission filter. This filter is capable of minimizing the fluorescence from the acceptor (BODIPY-FL), and there was no observable fluorescence signal from either the buffer solution or the unlabeled protein. DACM fluorescence decay kinetics was measured in both short (5 ns) and long (20 ns) time scale, whose time resolutions are ~ 10 and ~ 40 ps, respectively.

3.5.6 Data fitting and analysis

The measured short and long timescale data were spliced together, and the combined traces were compressed logarithmically before fitting process (70 points per decade). The splicing and compression did not introduce artifact to the interpretation of data (64). The TR-FET data analysis can be described as a numerical inversion of a Laplace transform [$I(t) = \sum_k P(k) \exp^{-kt}$] (71, 72). In this work, two algorithms were used to invert the kinetics data with regularization methods that impose additional constraints on the properties of $P(k)$. The simplest constraint that applies to the FET kinetics data is the non-negativity constraint, $P(k) \geq 0$ ($\forall k$).

The first method is based on the least-squares fitting algorithm. The kinetics data were fitted using a MATLAB algorithm (LSQNONNEG) (Mathworks, Natick, MA) that minimizes the sum of the squared deviations (χ^2) between observed and calculated values of $I(t)$, subject to the non-negativity constraint. The LSQNONNES algorithm produces the narrowest $P(k)$ distributions and smallest values of χ^2 with relatively few nonzero components.

The second method is based on the maximum entropy theory. The information theory proposes that the least biased solution to the inversion problem is to minimize χ^2 and maximize the breadth of $P(k)$ (73). This regularization condition can be met by maximizing the Shannon-Jaynes entropy of the rate-constant distribution

$$\left\{ S = -\sum_k P(k) \ln[P(k)] \right\} \text{ with the satisfaction of the non-negativity constraint.}$$

Maximum-entropy (ME) fitting generates stable and reproducible numerical inversions of the kinetics data. The balance between χ^2 minimization and entropy maximization is evaluated by the L-curve analysis. This approach yields upper limits for the widths of $P(k)$ consistent with our experimental data. The $P(k)$ distributions from ME fitting are broader than those obtained with LSQNNPNEG fitting, but exhibit maxima in similar locations.

Both methods were used to generate the decay rate distribution $P(k)$.

Subsequently, a coordinate transformation using the Förster relation (Eq. 3.2) was carried out to convert the probability distribution of the decay rates k to the donor-acceptor distances r .

$$r = R_0 \left(\frac{k}{k_0} - 1 \right)^{1/6}. \quad (3.2)$$

This transformation produces the donor-acceptor distance distribution $P(r)$ from the decay rate distribution $P(k)$. The Förster critical length, R_0 , for the DACM/BODIPY-FL pair is $\sim 47 \text{ \AA}$. The value of k_0 was obtained from donor-only measurements. At distances larger than $1.5 R_0$, energy transfer quenching of donor-fluorophor cannot compete with the excited-state decay so the energy transfer does not take place efficiently. In addition, at distances $\sim 13 \text{ \AA}$, the Förster model does not reliably describe

FET kinetics. Therefore, our TR-FET measurements can provide information about donor-acceptor distances only in the range from 13 to 70 Å.

3.6.7 Theoretical simulation

3.5.7.1 Early complex docking

ClusPro 2.0 docking server was used for early complex docking. During the docking, *E. coli*-Ffh was set to a static receptor while *E. coli*-FtsY was set to a ligand that searched for the best docking position with the receptor. The initial docking positions were generated by the Fast Fourier Transform method and docking positions were clustered according to their root mean square deviations. Clusters were sorted via a filter that was set to an electrostatic-favored energy function. The ranking of the clusters was determined by the number of structures that each cluster contained. The top five clusters have 89, 88, 65, 59 and 46 structures, respectively. The top two clusters, named GG and NN, were chosen for further analyses.

3.5.7.2 Hot spots analyses

Knowledge-based FADE and Contacts (KFC) server was used for hot spots prediction for GG and NN structures. Only the central structures of GG and NN clusters were used for this analysis. The hot spots were predicted by either K-FADE model (based on shape specificity feature) or K-CON model (based on biochemical contacts). Both models were trained with a set of alanine-scan experimental data and hot spots were defined as $\Delta\Delta G$ larger than 2 kcal/mol.

3.5.7.3 Brownian dynamics

BrownDye was used for Brownian Dynamics calculations (74). APBS (Adaptive Poisson-Boltzmann Solver) was used to calculate the electrostatic potentials (65). Partial

atomic charges and atomic radii were assigned from the PARSE parameter set. The dielectric constants were assigned to be 4 in the protein interior and 78 in the exterior. Grids were assigned with dimensions of $193 \times 193 \times 193$ points. Temperature was set to 298 K and ionic strength was set to 100 mM. Brownian dynamics trajectories were started at a minimum intermolecular separation that still gave spherically symmetric forces. The number of trajectories to estimate the association rate varied from 40,000 to 100,000 depending on how fast the association rates were. The reaction criterion was specified by the atom-contact pairs that were defined by the structure of the complex. All the intermolecular nitrogen-oxygen pairs within 0.55 nm were considered as within the reaction criterion. A series of simulations with different levels of reaction criteria were generated by systematically tuning the required atom-contact number from 3 to 7. Three structures were used for this analysis to obtain the association rate constants: the central structure of GG cluster, the central structure of NN cluster and the stable complex from crystal structure.

3.6 Supplementary Figures

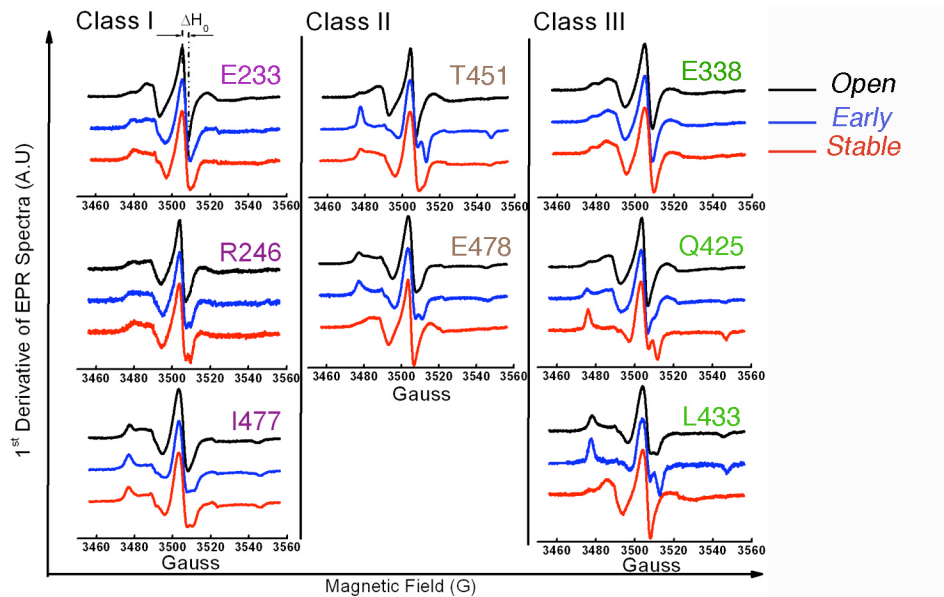


Figure 3.S1. The mobility of residues on SR changed upon formation of early complex (class II), stable complex (class III), or both complexes (class I). The black, blue and red curves represent the free proteins, the early complex and the stable complex, respectively. The mobility of spin-labeled residue was derived from the line width (ΔH_0) of the central resonance and the breadth of the spectra.

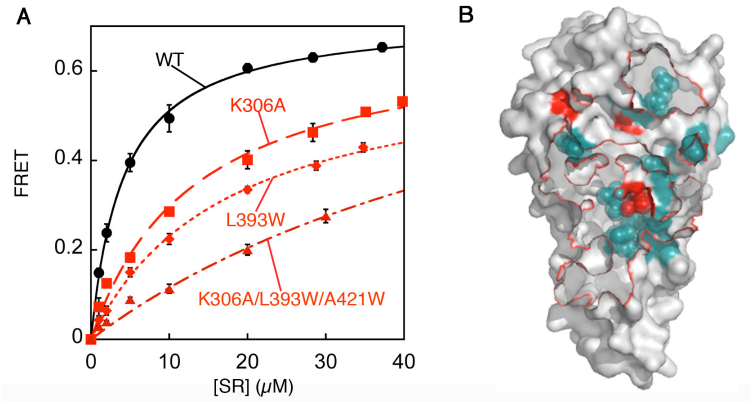


Figure 3.S2. Mutants that disrupt the formation of the stable complex only caused moderate defect in the stability of the early complex. (A) The stability of the early complexes formed by mutants was determined by equilibrium titration experiments. Nonlinear fits gave the equilibrium constants (K_d) of the early complexes as 4.1 μM for wild-type SR, 13.2 μM for SR (K306A), 17.3 μM for SR (L393W), and 31.3 μM for SR (K306A:L393W:A421W). (B) Positions of the SR mutants (cyan) studied in this work are shown on the surface representation of the SR. The three moderately defective mutants are highlighted in red. Red lines on the surface representation denotes the interaction surface between SRP and SR in the stable complex.

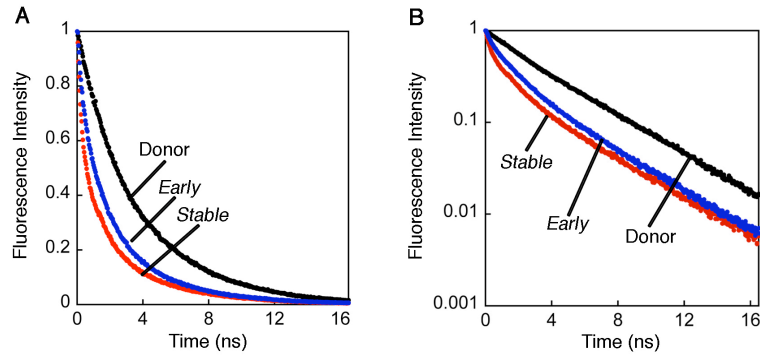


Figure 3.S3. Fluorescence decay of FRET donor (DACM) labeled at SRP (235C) under different experimental conditions. The black, blue, and red curves represent donor-only, donor-acceptor in the early complex, and donor-acceptor in the stable complex, respectively. The fluorescence decay curves in the linear and logarithmic scales are shown in (A) and (B), respectively. Donor-only measurement gave the linear decay of the donor fluorescence and could be fitted to a single exponential decay equation; suggesting that only one decay rate constant was observed. In contrast, the donor-acceptor curves in both the early and stable complexes gave non-linear decay of the donor fluorescence and could be fitted to a multiple-exponential decay equation; suggesting that multiple decay rate constants were recorded.

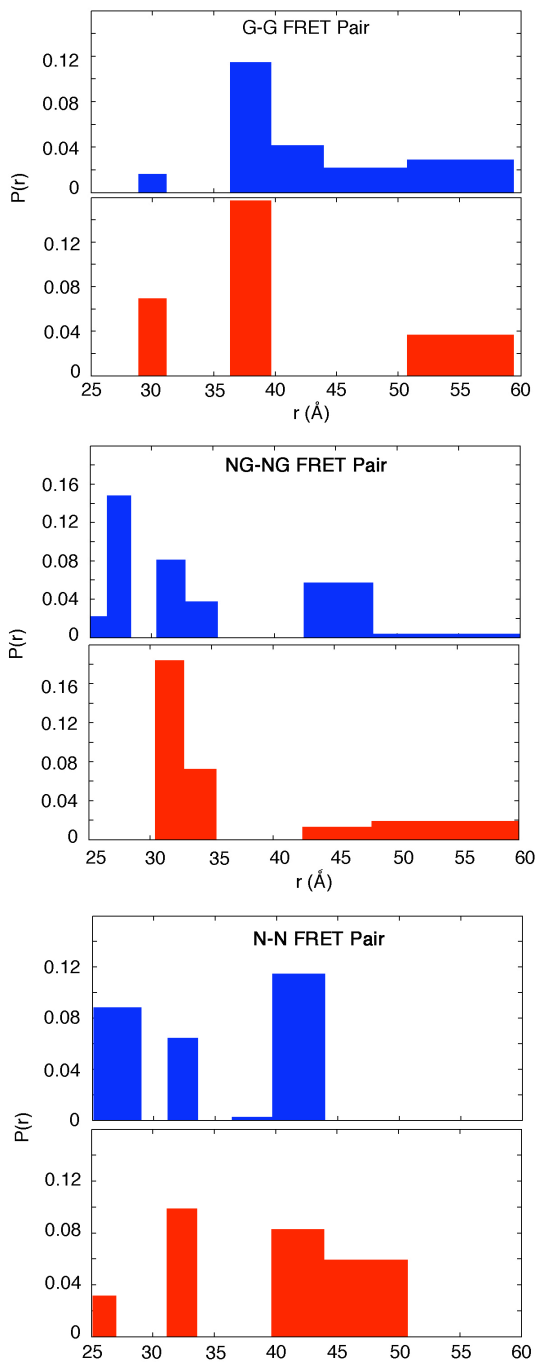


Figure 3.S4. Distance distributions derived from the least-square analyses (LSQ) of the TR-FRET kinetics data. Distribution of $P(r)$ was measured for each FRET pair in the pre-formed early complexes (blue) or stable complexes (red) under equilibrium condition.

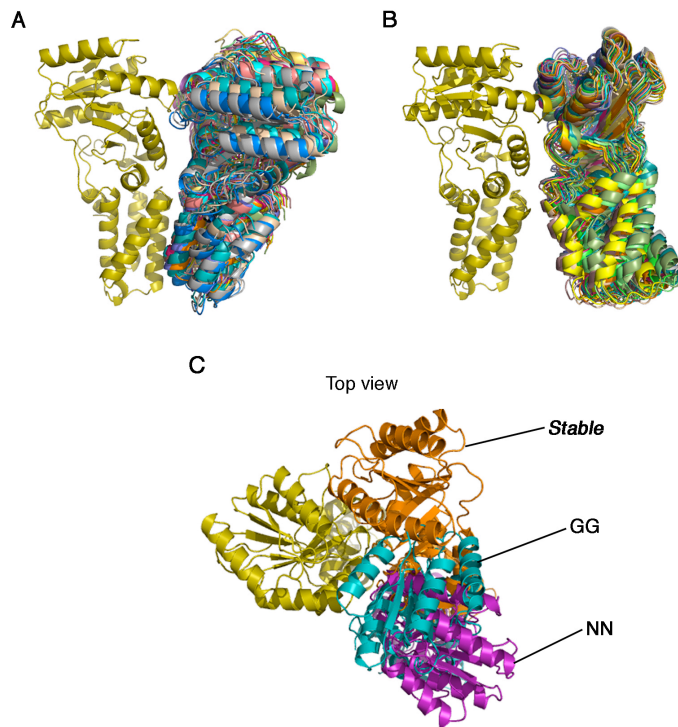


Figure 3.S5. Structural models of the SRP-SR early complex generated by molecular docking. **(A)** and **(B)**: Ensemble of the NN and GG complexes. Structures were overlaid on the top of the SRP GTPase (gold). **(C)**: Top view of the center structures of NN (pink) and GG (cyan) complexes in comparison to that of the co-crystal structure of the stable complex (brown). Structures were overlaid on the top of the SRP GTPase (gold). In the NN conformations, the G domain of the SR GTPase (FtsY) made no contact to the G domain of the SRP GTPase (Ffh). Although the G domains of both GTPases contacted one another in the GG conformations, the interaction surface was not fully formed and the GTP-binding pockets were open to allow free-exchange of nucleotide, explaining why the early complex is GTP-independent. To form the stable complex, extensive conformational rearrangements would be required in the early complex to establish an interaction surface between the SRP and SR GTPases. In particular, the G domains need to undergo a large sliding motion to achieve the correct orientation that is shown in the stable complex.

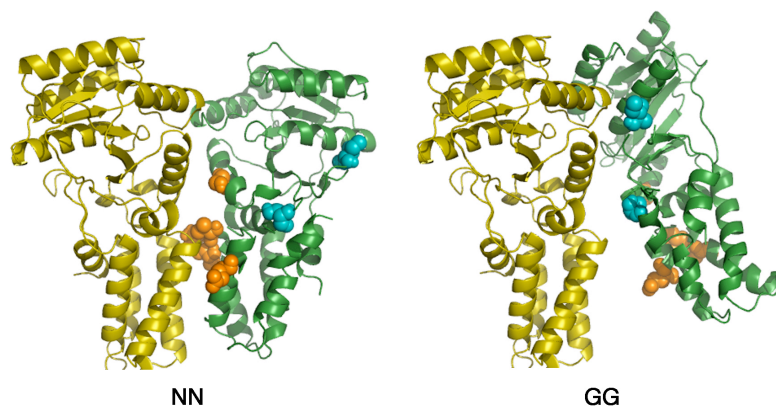


Figure 3.S6. Residues that changed mobility upon formation of the early complex resided close to the interaction surface of either the NN (orange residues) or the GG (cyan residues) complexes.

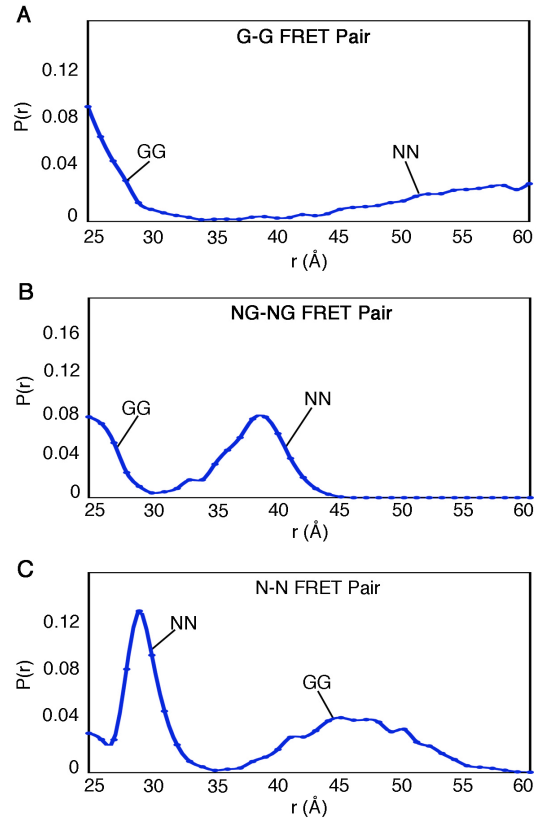


Figure 3.S7. Theoretical distance distributions derived from the NN and GG complexes for all FRET pairs.

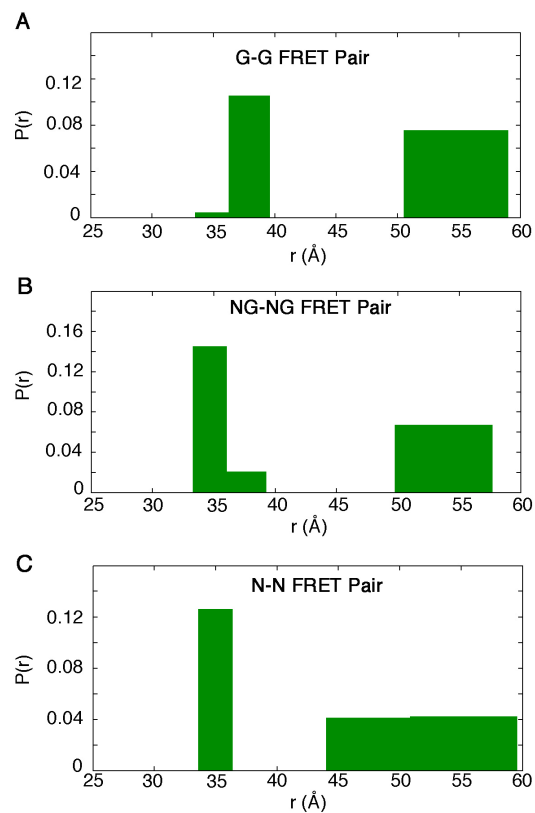


Figure 3.S8. Distance distributions derived from the least-square analyses (LSQ) of the TR-FRET kinetics data. Distribution of $P(r)$ was measured for each FRET pair in the preformed early complexes (green) in the presence of RNC_{FtsQ} .

3.7 Acknowledgements

I thank H. B. Gray for insightful discussions; Vinh Lam and Caltech EPR facility for carrying out EPR measurements; Jaeyoon Chung for protein purification and fluorescence labeling; Tetsunari Kimura and Jay W. Winkler for TR-FRET experiments; Yum Mou and Stephen L. Mayo for molecular docking and Brownian dynamics simulation; and Shan laboratory for helpful suggestions to experimental design. This work was supported by NIH grant GM078024, and career awards from the Burroughs Wellcome Foundation, the Henry and Camille Dreyfus foundation, the Beckman foundation, and the Packard foundation to S. S.

Chapter 4

Multiple Conformational Switches Control Co-translational Protein Targeting

A version of this chapter has been published as

*X Zhang, C Schaffitzel, N Ban, S-O Shan, Proceedings of the National Academy of Sciences of the United States of America, (2009), **106**, 1754-1759.*

4.1 Abstract

The “GTPase switch” paradigm, in which a GTPase switches between an active, GTP-bound state and an inactive, GDP-bound state through the recruitment of nucleotide exchange factors (GEFs) or GTPase activating proteins (GAPs), has been used to interpret the regulatory mechanism of many GTPases. A notable exception to this paradigm is provided by two GTPases in the signal recognition particle (SRP) and the SRP receptor (SR) that control the co-translational targeting of proteins to cellular membranes. Instead of the classical “GTPase switch”, SRP and SR undergo a series of discrete conformational rearrangements during their interaction with one another, culminating in their reciprocal GTPase activation. Here, we show that this series of rearrangements during SRP–SR binding and activation provide important control points to drive and regulate protein targeting. Using real time fluorescence, we showed that the cargo for SRP – ribosomes translating nascent polypeptides with signal sequences – accelerates SRP–SR complex assembly over 100 fold, thereby driving rapid delivery of cargo to the membrane. A series of subsequent rearrangements in the SRP•SR GTPase complex provide important driving forces to unload the cargo during late stages of protein targeting. Further, the cargo delays GTPase activation in the SRP•SR complex by 8–12 fold, creating an important time window that could further improve the efficiency and fidelity of protein targeting. Thus the SRP and SR GTPases, without recruiting external regulatory factors, constitute a self-sufficient system that provides exquisite spatial and temporal control of a complex cellular process.

4.2 Introduction

SRP-mediated co-translational protein targeting delivers roughly a third of proteins to their correct subcellular destinations, including the eukaryotic endoplasmic reticulum and the bacterial plasma membrane. This pathway involves a sequential series of molecular steps (2, 6, 7), including (1) recognition and loading of cargo (ribosomes translating nascent polypeptides with signal sequences) on the SRP; (2) delivery of cargo to the target membrane via complex formation between SRP and SR; (3) unloading and transfer of cargo from the SRP to the protein conducting channel (PCC); and (4) disassembly of the SRP•SR complex and recycling of free SRP and SR for subsequent rounds of protein targeting. Like many cellular processes, this complex series of molecular interactions are spatially and temporally regulated by members of the GTPase superfamily, in this case, two highly homologous and directly interacting GTPases in both the SRP and SR.

SRP and SR provide a notable exception to the ‘GTPase switch’ paradigm established for classical signaling GTPases (75). These GTPases do not exhibit substantial conformational changes depending on whether GTP or GDP is bound (26-28), and further, their intrinsic nucleotide exchange rates are 10^2 – 10^4 fold faster than those of classical GTPases (29, 76). Thus no external GEFs are required to switch these GTPases from the GDP- to the GTP-bound state, and the facilitation of nucleotide exchange by an external GEF cannot be the mechanism to turn these GTPases to the ‘on’ state. Moreover, SRP and SR reciprocally stimulate each other’s GTP hydrolysis activity when they form a complex with one another (21, 29). Thus no external GAPs are required either to switch these GTPases from the GTP- to the GDP-bound state, and the

stimulation of GTP hydrolysis by an external GAP cannot be the mechanism to turn these GTPases to the 'off' state. In contrast, these GTPases undergo a series of discrete conformational changes driven by heterodimeric interactions between the two GTPases (figure 4.1) (9, 20, 21, 77). Both proteins, starting in an inactive, '*open*' conformation, quickly bind one another to form a transient '*early*' intermediate independently of GTP (figure 4.1, step 1). The presence of GTP bound at both GTPase active sites induces a conformational rearrangement in both proteins to form a stable '*closed*' complex (figure 4.1, step 2) (9, 77, 78). A subsequent rearrangement involving the activation loops in both proteins activates GTP hydrolysis (figure 4.1, step 3) (9, 20), which drives disassembly of the complex (figure 4.1, step 4) (79).

If these conformational rearrangements during SRP–SR binding and activation are integral to the regulatory role of these GTPases in protein targeting, then they should be responsive to the biological events they are monitoring. To test this hypothesis, we examined the effects of cargo loading on the kinetic and thermodynamic features of the SRP and SR's GTPase cycle. Our results demonstrate that the SRP and SR GTPases can use each of the conformational changes during their binding and activation cycle to sense temporal cues such as cargo loading and in response, substantially change the free energy landscape of the different conformational states in the SRP•SR GTPase complex. These cargo-induced responses allow these GTPases to drive the efficient delivery and unloading of cargo to the target membrane, and to potentially improve the fidelity of protein targeting via kinetic proofreading mechanisms.

4.3 Results

4.3.1 General Experimental Approach

To monitor the different conformational stages of the SRP•SR complex, we used fluorescence resonance energy transfer (FRET) between donor and acceptor probes incorporated on the SRP and SR. FRET provides a highly sensitive assay that allows us to detect the transient *early* intermediate (figure 4.1) (80). Further, this intermediate can be distinguished from the subsequent conformations because it has a lower FRET value than the *closed* and *activated* complexes (figure 4.1) (80). In addition, an environmentally sensitive probe, acrylodan labeled at residue 235 of SRP, detects formation of the *closed* and *activated* complexes but not the *early* intermediate (figure 4.1 and figure 4.S1), thereby simplifying kinetic and thermodynamic analyses of these later conformations. Finally, acrylodan labeled at residue 356 of SR near its catalytic loop specifically detects the *activated* complex (figure 4.1 and figure 4.S2). In addition to these fluorescent probes, mutant GTPases and GTP analogues were used to block specific rearrangements and thus isolate each conformational intermediate (9, 21). We can block the *early* → *closed* rearrangement by leaving out GTP (figure 4.1) (80); this allows us to isolate the *early* intermediate and characterize its kinetics and stability. Mutations in the catalytic loop, SRP A144W or SR A335W, allow a stable *closed* complex to form but block its rearrangement to the *activated* complex (9, 10). The non-hydrolyzable GTP analogue 5'-guanylylimido-diphosphate (GppNHp) allows most of the rearrangements to occur but inhibits GTP hydrolysis (9, 21). Using these tools, we determined how the SRP and SR GTPases use their conformational changes to respond to cargo loading.

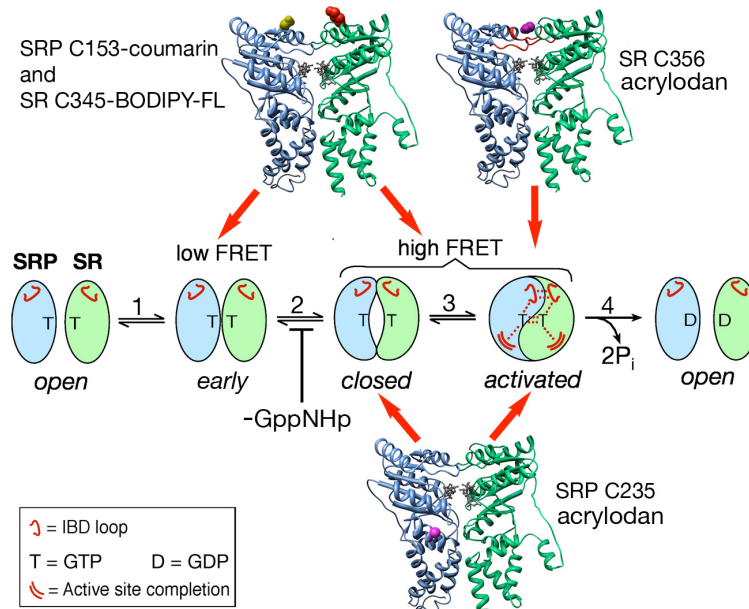


Figure 4.1. Multiple conformational changes during SRP-SR complex formation and activation (9, 80), as described in the text, and the positions of fluorescence probes that detect the different conformational stages, as described in the text.

4.3.2 Cargo Accelerates Assembly of a Stable SRP•SR Complex over 100 Fold

As cargo, we purified stalled ribosome•nascent chain complexes (RNCs) bearing the N-terminal 74 amino acids of the model SRP substrate FtsQ (67, 81, 82). SRP-SR complex assembly was monitored using FRET in the presence of GppNHp. Comparison of the time courses for complex assembly shows three differences between free and cargo-loaded SRP (figure 4.2A): (1) the initial rates are much faster with cargo-loaded SRP; (2) the kinetics of complex formation with cargo-loaded SRP is bi-phasic with a burst phase, suggesting the accumulation of an intermediate; (3) at completion of the reaction, FRET plateaus at a lower value for cargo-loaded SRP, suggesting a change in the equilibrium stability of the final SRP•SR complex. These effects are further characterized in the following.

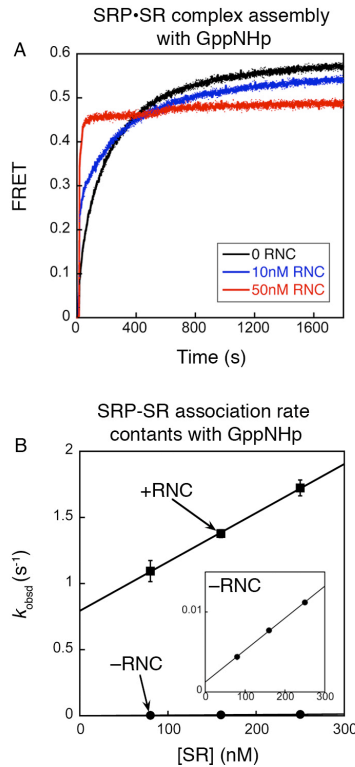


Figure 4.2. Cargo changes the kinetics of SRP-SR interaction. (A) Time courses for SRP-SR complex assembly with GppNHp in the absence (black) or presence of 10 nM (blue) and 50 nM (red) RNC, using 10 nM SRP and 100 nM SR to mimic physiological protein concentrations (83). (B) Cargo accelerates SRP-SR complex assembly with GppNHp by 100 fold. The data are fit to the equation: $k_{obsd} = k_{on}[SR] + k_{off}$, and gave association rate constants (k_{on}) of $3.7 \pm 0.4 \times 10^6 \text{ M}^{-1} \text{ s}^{-1}$ and $4.0 \pm 0.3 \times 10^4 \text{ M}^{-1} \text{ s}^{-1}$ with (■) and without (●) 60 nM RNC, respectively.

An observed rate constant for complex formation (k_{obsd}) at any protein concentration is the sum of the complex assembly and disassembly rate constants (84)

$$k_{obsd} = k_{on} \times [SR] + k_{off} . \quad (4.1)$$

To isolate the effect of cargo on complex assembly, we measured the observed rate constants as a function of SR concentration; the slope of this concentration dependence gives the association rate constant, k_{on} [Eq. (4.1); figure 4.2B]. The value of k_{on} is $4.4 \times 10^4 \text{ M}^{-1} \text{ s}^{-1}$ in the absence of cargo, consistent with previous measurements (21). In the

presence of cargo, the complex formation rate constant is 100–400 fold faster (figure 4.2B and figure 4.S3A). Thus cargo-loaded SRP has a substantial kinetic advantage over free SRP to form a complex with the SR, ensuring efficient delivery of cargo to the target membrane.

4.3.3 Cargo Stabilizes the *Early Intermediate* by Two Orders of Magnitude

The biphasic kinetics with a burst phase during complex formation with cargo-loaded SRP suggests the accumulation of an intermediate (figures 4.2A and 4.3A, blue). A likely candidate to account for this burst is the *early* intermediate, which forms quickly and has a lower FRET value than the subsequent complexes (figure 4.1) (80). To test this notion, we blocked the *early* → *closed* rearrangement and isolated the *early* complex by performing complex assembly in the absence of nucleotide (figure 4.1, step 2; figure 4.3A, green). Both the rate and the magnitude of FRET changes for assembly of the *early* intermediate agree well with those of the burst phase during complex assembly with GppNHp (figure 4.3A). This provides strong evidence that in the presence of cargo, the *early* intermediate accumulates substantially during complex assembly.

The *early* intermediate, which lacks stabilizing interactions from the γ -phosphate of GTP, is very unstable without cargo (26, 80), hence it cannot accumulate under the nanomolar concentrations of SRP and SR used here (figure 4.2A, black). Therefore it was surprising to detect its accumulation with cargo-loaded SRP. This observation suggests that the cargo strongly stabilizes this intermediate. To test this hypothesis, we determined the equilibrium and kinetic stability of the *early* complex with and without cargo. Indeed, the cargo stabilizes the *early* complex over 50 fold, lowering its

equilibrium dissociation constant (K_d) from 4–10 μM (80) to 80 ± 4 nM (figure 4.3B, squares) and decreasing its dissociation rate constant (k_{off} , derived from the y-intercept in figure 4.3C) from 62 ± 2 s^{-1} to 1.6 ± 0.1 s^{-1} .

Stabilization of the *early* intermediate explains the faster rate of SRP–SR complex assembly with GppNHp for cargo-loaded SRP (figure 4.2B). Without cargo, formation of the highly labile *early* intermediate is not sufficient to give a stable SRP•SR complex; to obtain a stable complex, the *early* intermediate needs to rearrange to the *closed* complex. However the *early* intermediate dissociates quickly and less than 2% of the population rearranges to form the *closed* complex ($k_{\text{off}} = 62 \pm 2$ s^{-1} vs $k_{\text{rearrange}} = 1.03 \pm 0.02$ s^{-1}) (80). This gives rise to the slow rate constant for formation of a stable *closed* complex between free SRP and SR. In contrast, for cargo-loaded SRP the *early* intermediate is stabilized over 50 fold. Thus forming the *early* complex (figure 4.1, step 1) is sufficient to give a relatively stable SRP•SR complex under physiological SRP and SR concentrations (200–400 nM) (83). Furthermore, the cargo•SRP•SR *early* complex dissociates with much slower kinetics (figure 4.3C, $k_{\text{off}} = 1.6 \pm 0.1$ s^{-1}), giving this intermediate a much longer lifetime to undergo subsequent rearrangements. Both of these effects contribute to the faster rate of assembling a stable GTPase complex with cargo-loaded SRP in the presence of GppNHp.

4.3.4 Cargo Stalls the SRP•SR Complex at Earlier Conformational Stages

The different FRET end points in figure 4.2A suggest that the stability of the final SRP•SR complex is also altered by the cargo. To test this hypothesis, we compared the equilibrium stability of the SRP•SR complex assembled in GppNHp with and without

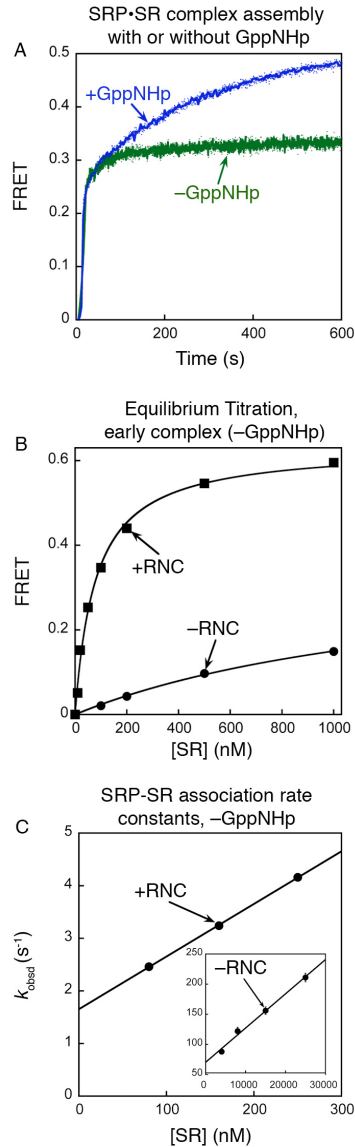


Figure 4.3. Cargo stabilizes the early intermediate. (A) Comparison of the time courses for SRP-SR complex formation for cargo-loaded SRP in the absence (green) and presence of 100 μM GppNHp (blue). Data were obtained using 20 nM SRP, 100 nM SR and 20 nM RNC. (B) Cargo stabilizes the *early* intermediate 50 fold. Equilibrium titration of the *early* complex assembled in the absence of GppNHp with (■) and without (●) 50 nM RNC. Nonlinear fits of data gave K_d values of 80 ± 4 nM in the presence of RNC. (C) Cargo increases the kinetic stability of the *early* intermediate 40 fold. The data are analyzed as in part B and give $k_{\text{on}} = 1.0 \pm 0.1 \times 10^7 \text{ M}^{-1} \text{ s}^{-1}$ with cargo-loaded SRP, which is within two fold of the value in the absence of RNC ($k_{\text{on}} = 5.6 \pm 0.3 \times 10^6 \text{ M}^{-1} \text{ s}^{-1}$) (80), and $k_{\text{off}} = 1.62 \pm 0.1 \text{ s}^{-1}$, which is 40 fold slower than that in the absence of RNC ($k_{\text{off}} = 60 \pm 2 \text{ s}^{-1}$) (80). The inset shows the data in the absence of RNC (adapted from ref. (80)). Note the difference in scales between the two plots.

cargo using SRP C235 labeled with acrylodan (figure 4.1 and figure 4.S1). Equilibrium titrations using this probe showed that the cargo destabilizes the *closed/activated* complexes four fold, increasing its K_d from 10 ± 2 nM to 40 ± 4 nM (figure 4.4A). A similar destabilizing effect was observed using the FRET probes, with the K_d of the *closed/activated* increasing from 14 ± 3 nM without cargo to 60 ± 7 nM with cargo-loaded SRP (figure 4.S4). An additional probe that specifically monitors the *activated* complex, acrylodan-labeled SR C356 (figure 4.1 and figure 4.S2), also confirmed that the cargo destabilizes the *activated* complex (figure 4.4B). In summary, the results from all three fluorescence probes showed that, in contrast to the large stabilizing effect of the cargo on the *early* intermediate, the subsequent conformations during the SRP-SR interaction are destabilized by the cargo.

Thus the cargo significantly alters the conformational rearrangements in the SRP•SR complex (figure 4.4C). Without cargo, the *closed* and *activated* states are >400 fold more stable than the *early* intermediate, therefore the equilibrium for the *early* → *closed* rearrangement is extremely favorable (figure 4.4C, $K^{\text{rel}} = 400$). In contrast, in the cargo•SRP•SR complex this rearrangement is 200 fold less favorable (figure 4.4C, $K^{\text{rel}} = 1.3\text{--}2$). Thus in the cargo•SRP•SR complex, a substantial fraction of the GTPase complex is still in the *early* conformation (30–40%) even in the presence of GppNHp. This conformational heterogeneity of the GTPase complex in the presence of cargo is consistent with previous EM analysis that showed that, while the SRP is well-resolved in the RNC•SRP complex, upon addition of SR and GppNHp the electron density for both the SRP and SR's GTPase domains are no longer visible (85). Thus both the biochemical

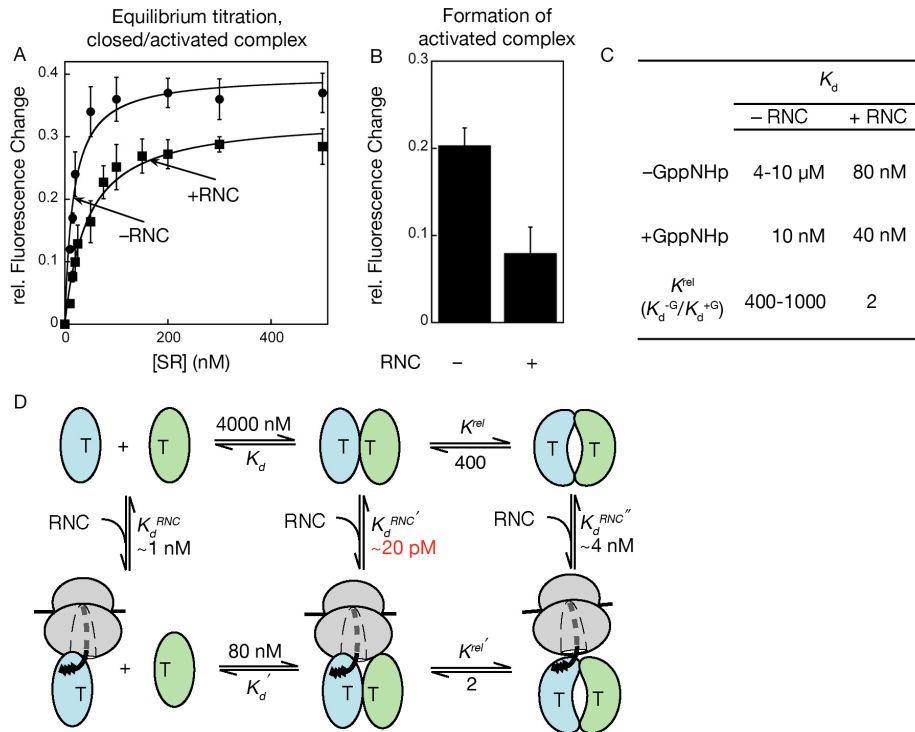


Figure 4.4. Cargo destabilizes the *closed* and *activated* states during SRP-SR interaction. (A) Equilibrium titration of the SRP•SR complex assembled in GppNHp with (■) and without (●) RNC using acrylodan-labeled SRP C235. Nonlinear fits of data gave K_d values of 10 ± 2 nM (without RNC) and 40 ± 4 nM (with RNC). (B) Relative fluorescence changes of acrylodan-labeled SR C356 in the presence and absence of cargo, obtained using 50 nM SRP and 15 nM labeled SR with 100 μ M GppNHp. An accurate K_d value could not be determined with this probe because of the large amount of cargo-loaded SRP that would be required to saturate labeled SR C356. (C) Equilibrium constants of the GTP-independent (K_d^{-G}) and GTP-dependent (K_d^{+G}) SRP•SR complexes with or without RNC. The equilibrium for rearrangement (K^{rel}) were calculated from $K^{rel} = K_d^{-G}/K_d^{+G}$. (D) Thermodynamic analysis of the interaction of cargo with SRP at different conformational stages during the SRP-SR interaction.

and structural analyses highlight the dynamic nature of the GTPase complex when it is bound to the cargo.

The SRP•SR complex can use the *early* \rightarrow *closed* rearrangement to drive cargo unloading during protein targeting (figure 4.4D). Initially, cargo loading stabilizes the *early* intermediate 50 fold (figure 4.4D, K_d and K_d'). Correspondingly, the interaction of

cargo with SRP should be stabilized to the same extent in the *early* intermediate (figure 4.4D, $K_d^{\text{RNC}'}/K_d^{\text{RNC}} = K_d'/K_d = 50$). Using the value of $K_d^{\text{RNC}} \sim 1$ nM (86, 87), the stability of cargo bound to the *early* intermediate would be in the range of $K_d^{\text{RNC}'} \sim 20$ pM.

Although this effect could enhance the initial recognition and delivery of cargo to the membrane, such strong binding will block the subsequent unloading of cargo from the SRP. This problem is circumvented by the 200 fold destabilizing effect of cargo on the *early* \rightarrow *closed* rearrangement (figures 4.4C and 4.4D, K^{rel} and $K^{\text{rel}'}$). Correspondingly, the interaction of cargo with SRP would also be weakened 200 fold by this rearrangement (figure 4.4C, $K_d^{\text{RNC}''}/K_d^{\text{RNC}} = K^{\text{rel}'}/K^{\text{rel}}$), thus priming the cargo for subsequent unloading. This model is supported by mutational analyses that showed that mutant GTPases defective in the *early* \rightarrow *closed* rearrangement severely block protein translocation (10). The observation that mutants defective in the *closed* \rightarrow *activated* rearrangement inhibit protein translocation further suggest that this last rearrangement is also essential for cargo unloading (10). Therefore both rearrangements within the GTPase complex provide essential driving forces to help unload the cargo from the SRP to the PCC, thus initiating protein translocation.

Since cargo disfavors the rearrangements to form the *activated* complex, one would predict that stimulated GTP hydrolysis, which occurs from the *activated* complex, would also be impaired. To test this notion, we compared the GTPase reaction rate from the SRP•SR complex in the presence and absence of cargo. In the absence of cargo, the GTPase rate of free SRP is significantly stimulated by the addition of SR (figure 4.5, circles). The reaction rate reaches a plateau of 0.79 s⁻¹ at saturating SR concentrations,

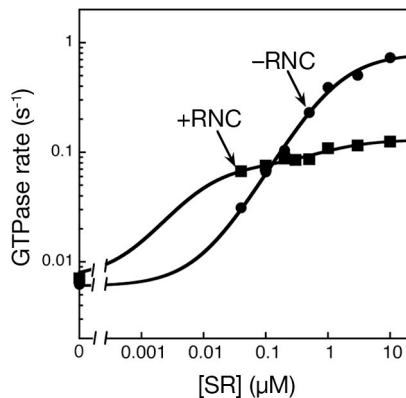


Figure 4.5. Cargo delays activation of GTP hydrolysis in the SRP•SR complex. GTPase rate constants were measured using 40 nM SRP and 100 μM GTP in the absence (●) and presence (■) of 100 nM RNC. The data in the absence of cargo were fit to a single binding curve and gave a rate constant of 0.79 s^{-1} for GTP hydrolysis from the SRP•SR complex. The data in the presence of cargo is not consistent with a single binding curve and was fit to a model based on two populations of SRP•SR complexes that reacts at rate constants of 0.064 and 0.11 s^{-1} .

representing the GTPase rate constant from the SRP•SR complex (figure 4.5, circles). In the presence of cargo, significantly less GTPase stimulation was observed (figure 4.5, squares). Intriguingly, two plateaus were observed for the GTPase reaction in the presence of cargo (figure 4.5, squares), suggesting the presence of two populations of cargo•SRP•SR complexes: one population, which forms at low SR concentrations (below 50 nM), hydrolyzes GTP at a rate constant of 0.064 s^{-1} ; the second population, which forms at higher SR concentrations (above 1 μM), hydrolyzes GTP at a rate constant of 0.11 s^{-1} (figure 4.5, squares). Although the nature of this heterogeneity is unclear at present, in both of these populations the GTPase activity is repressed by the RNC (12- and 8 fold for the first and second population, respectively). The effect of cargo in reducing the GTP hydrolysis rate is specific to the SRP•SR complex, as the cargo does not affect the basal GTP hydrolysis rate of free SRP (figure 4.S5). Thus the cargo also

delays GTPase activation in the SRP•SR complex. This effect, which we term ‘stalling’, would provide an important time window that allows the SRP to unload the cargo before GTP hydrolysis drives irreversible complex disassembly, as discussed below.

4.4 Discussion

We showed here that cargo loading substantially alters the free energy landscape of the SRP–SR interaction cycle (figure 4.6A). Without cargo (black), assembly of a stable SRP•SR complex is slow because it requires rearrangement from an unstable *early* intermediate (figure 4.6A, $\Delta G_{\text{complex}}^{\ddagger} = \Delta G_{\text{early}} + \Delta G^{\ddagger}$) (80). Further, the stable SRP•SR complex has a short lifetime because as soon as it is formed, rapid activation of GTP hydrolysis drives its irreversible disassembly (29). The cargo uses a remarkably simple solution to these problems, by stabilizing the *early* intermediate (figure 4.6A, $\Delta\Delta G = -2.4$ kcal/mol) and disfavoring the *closed* and *activated* states (figure 4.6A, $\Delta\Delta G \geq +0.8$ kcal/mol). This accelerates complex assembly (figure 4.6A, $\Delta\Delta G^{\ddagger} = -2.8$ kcal/mol), and prolongs the lifetime of the SRP•SR complex due to delayed GTP hydrolysis (figure 4.6A, $\Delta\Delta G^{\ddagger} = +1.3 - 1.5$ kcal/mol). The rate-limiting step of the SRP–SR interaction cycle shifts from the *early* \rightarrow *closed* rearrangement with free SRP to GTP hydrolysis with cargo-loaded SRP.

These cargo-induced effects allow the SRP and SR to use each of their conformational rearrangements to regulate a distinct step during protein targeting (figure 4.6B). At the beginning of each targeting cycle, cargo loading (figure 4.6B, step 1) allows the SRP to assemble a stable complex with SR >100 fold faster (figure 4.6B, step 2). This ensures rapid delivery of cargo to the membrane (88, 89), and avoids futile

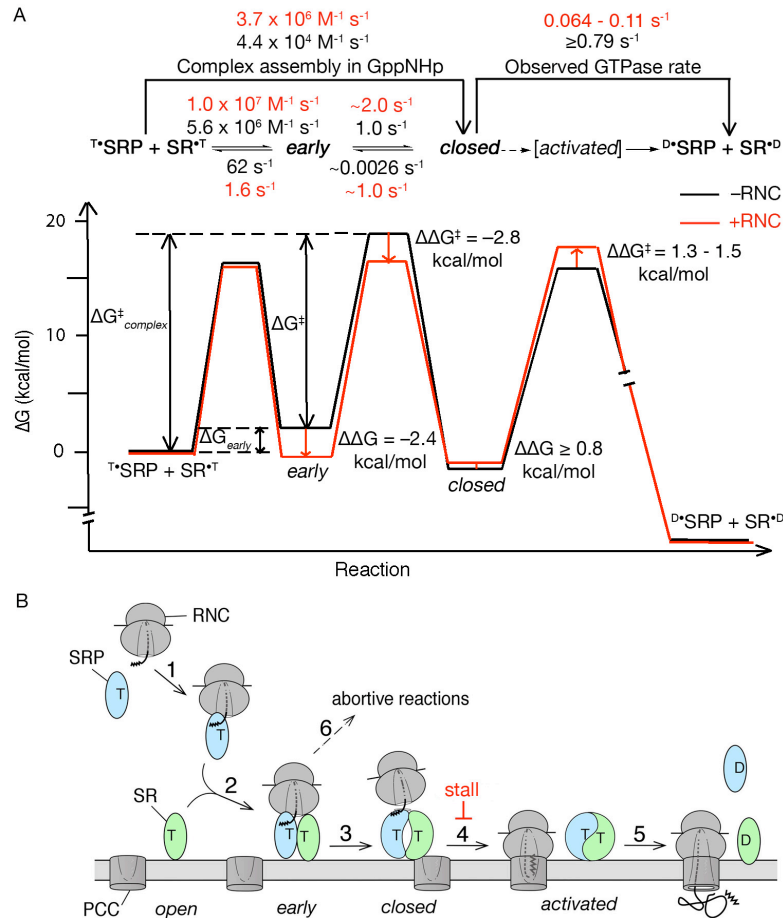


Figure 4.6. Conformational changes during the SRP–SR interaction respond to cargo loading and regulate protein targeting. (A) Rate constants and free energy profile for the SRP–SR interaction in the absence (black) and presence (red) of cargo. A standard state of 200 nM SRP is used to approximate cellular protein concentrations. Activation energies were calculated from the observed association and dissociation rate constants using $\Delta G^\ddagger = -RT \ln(kh/k_B T)$, where $R = 1.987 \text{ cal K}^{-1} \text{ mol}^{-1}$, $h = 1.58 \times 10^{-37} \text{ kcal s}^{-1}$, $k_B = 3.3 \times 10^{-27} \text{ kcal K}^{-1}$, and $T = 298\text{K}$. The relative energies of the different complexes were calculated from the observed equilibrium stabilities using $\Delta G = -RT \ln K$, where K is the equilibrium constant. ΔG_{early} is the free energy cost to form the *early* complex, ΔG^\ddagger is the activation energy for the *early* \rightarrow *closed* rearrangement. The sum of these two gives the overall energy barrier to form the *closed* complex ($\Delta G^\ddagger_{\text{complex}}$), which is lowered 2.8 kcal mol⁻¹ by the cargo because the cargo stabilizes the *early* complex by 2.4 kcal mol⁻¹. In contrast, the RNC increases the activation energy for GTP hydrolysis by 1.9 kcal mol⁻¹. (B) Proposed model for how the conformational changes during the SRP–SR interaction regulate protein targeting and translocation as described in text.

interactions between free SRP and SR. In the *early* intermediate, the cargo is locked in the SRP•SR complex with very high affinity (figure 4.4D, $K_d^{RNC'} \sim 20$ pM), allowing the SRP to effectively compete with cellular chaperones for binding the cargo. Subsequent GTPase rearrangements to the *closed* and *activated* conformations weaken the interaction of cargo with the SRP (figure 4.6B, steps 3–4; and figure 4.4D) and thus help the SRP to switch from a cargo-binding mode to a cargo-release mode, to unload the cargo to the PCC (figure 4.6B, step 4). Once in the *activated* conformation, and especially after cargo release, rapid GTP hydrolysis drives the disassembly and recycling of SRP and SR (figure 4.6B, step 5).

The mechanism proposed here (figure 4.6B) focuses on GTP-bound SRP and SR because the high cellular concentration of GTP compared to GDP (~900 microM and 100 microM in bacteria, respectively) predicts that over 90% of both GTPases are bound with GTP. Minor pathways are also possible in which empty-site or GDP-bound forms of SRP and SR first form the *early* intermediate to deliver cargo to the membrane surface, followed by rapid binding or exchange of GTP to drive the subsequent steps (88, 89); these pathways are not depicted in Figure 4.6B for clarity.

The most intriguing effect of cargo is ‘stalling’, i.e., the delay of GTPase activation by ~8–12 fold (figure 4.6B, step 4). A similar effect was suggested from studies of the mammalian system where prior to the addition of the PCC, a stable cargo•SRP•SR complex persists in the presence of GTP, suggesting that the cargo may also delay GTP hydrolysis in the mammalian SRP•SR complex (90). We suggest that stalling creates an important time window during which SRP ensures the efficiency and fidelity of protein targeting, via either or both of the following mechanisms. First,

stalling could provide a spatial checkpoint for the target membrane and/or the PCC. Before the SR associates with the PCC, stalling prevents premature GTP hydrolysis that would irreversibly disassemble the SRP•SR complex, and thus help avoid abortive targeting reactions (figure 4.6B, step 6). Interaction of SR with the PCC may trigger the rearrangement to the *closed* and *activated* states and initiate cargo unloading (90). The PCC also competes with SRP for interacting with the RNC (81, 82, 85, 91), which could further drive the transfer of cargo from SRP to the PCC (90, 92). Alternatively, stalling could provide a fidelity checkpoint. Many of the effects of the cargo described here are observed only with RNCs but not with empty ribosomes (figure 4.S6) nor with RNCs bearing weak signal sequences, establishing the importance of the signal sequence. It could be envisioned that cargos with weaker signal sequences could not effectively stall the SRP•SR complex, and thus are more likely to be rejected via premature GTP hydrolysis (figure 4.6B, step 6). In this way, GTP hydrolysis could be used to improve the fidelity of protein targeting akin to kinetic proofreading mechanisms used by elongation factor (93).

4.5 Materials and Methods

4.5.1 Materials

The *Escherichia coli* SRP and SR GTPases (Ffh and FtsY, respectively) and 4.5S RNA were expressed and purified using established procedures (10, 29). Most of the fluorescence experiments used the FtsY(47–497) construct. This truncated FtsY construct behaves similarly to full length FtsY in its ability to interact with the SRP and to respond to the cargo (SI: figure S3). The GTPase reactions with and without cargo was determined with full length FtsY. Mutant proteins were constructed using the QuickChange procedure (Stratagene, La Jolla, CA), and were expressed and purified by the same procedure as that for the wild-type protein. Fluorescent dyes DACM, BODIPY-FL and acrylodan were from Invitrogen (Carlsbad, CA). 70S ribosomes and RNCs were purified as described previously (67, 94, 95).

4.5.2 Fluorescence labeling

For FRET measurements, maleimide derivatives of coumarin and BODIPY-FL were used to label single-cysteine mutants of SRP and SR, respectively, as described (80). Labeling of SRP and SR with acrylodan followed the same procedure except that the labeling reaction was carried out using a 30 fold excess of dye over protein for over twelve hours at 4 °C. Absorbance of acrylodan ($\epsilon_{391} = 20,000 \text{ M}^{-1} \text{ cm}^{-1}$) was used to determine the concentration of labeled protein. The efficiency of labeling reaction was typically $\geq 90\%$ for both proteins. The background, estimated from the labeling of cysteinless SRP and SR using the same procedure, is less than 3%.

4.5.3 Fluorescence measurement

All measurements were carried out at 25 °C in assay buffer [50 mM KHEPES, pH 7.5, 150 mM KOAC, 10 mM Mg(OAc)₂, 2 mM DTT, 0.01% Nikkol] on a Fluorolog-3 spectrofluorometer (Jobin Yvon, Edison, NJ) as described (29, 80). FRET measurements were carried out using an excitation wavelength of 380 nm and an emission wavelength of 470 nm. FRET efficiency was calculated as described (80). Fluorescence emission spectrum of SRP (or SR) labeled with acrylodan was measured using an excitation wavelength of 370 nm. Fluorescence emission at 500 nm was monitored for equilibrium titrations using acrylodan-labeled protein.

Pulse chase experiments were carried out using unlabeled protein to trap any dissociated protein SRP or SR (21). Fast reactions were measured on a Kintek stop-flow apparatus (21). The incubation time during equilibrium measurements was calculated based on the SRP•SR complex assembly rate (21, 80), and varies from five minutes for fast reactions (*early* complex assembly and complex assembly in the presence of cargo) to several hours (complex assembly with GppNHp in the absence of cargo).

4.5.4 GTPase assay

The GTPase assay to measure the stimulated GTP hydrolysis reaction between SRP and SR were carried out and analyzed as described (29). Multiple turnover reactions were carried out at 25 °C with a small, fixed amount of free or cargo-loaded SRP and increasing concentrations of SR, 100 microM GTP (doped with trace γ -³²P-GTP) was present in the reaction to saturate both GTPase sites. Previous studies have established that the GTPase reaction rate is ratelimited by SRP-SR complex formation at

subsaturating SR concentrations, whereas at saturating SR concentrations, the reaction is rate-limited by GTP hydrolysis or a slow conformational change preceding GTP hydrolysis (29). The release of products, including dissociation of GDP, P_i, and disassembly of the ^{GDP}•SRP•SR^{GDP} complex, are not rate-limiting for the GTPase assay (29).

4.5.5 Preparation of 70S ribosomes and RNCs

70S empty ribosomes were purified from *E coli* MRE600 following a modified protocol described by Moazed and Noller (95). Cell pellet from a 1 L culture was resuspended in 30 mL buffer A [20 mM Tris•HCl (pH 7.0 at 21 °C), 10.5 mM MgCl₂, 100 mM NH₄Cl, 0.5 mM EDTA, 6 mM 2-mercapto ethanol (βME)]. The cell resuspension was passed through the French Press twice to lyse the cells. The lysate was clarified by two rounds of centrifugation at 20,000 g for 15 minutes at 4°C. The supernatant was layered on a 1.1 molar sucrose cushion in buffer B [20 mM Tris•HCl (pH 7.0 at 21 °C), 10.5 mM MgCl₂, 500 mM NH₄Cl, 0.5 mM EDTA, 6 mM βME, 1.1M sucrose] and ultracentrifuged at 100,000 g for 21 hours at 4°C. The ribosome pellet was collected and dissolved in buffer A containing 500 mM NH₄Cl. The dissolved ribosomes were ultracentrifuged at 4 °C for 3 hours at 100,000 x g. The pellet was dissolved in buffer C [20 mM Tris•HCl (pH 7.0 at 21 °C), 6 mM MgCl₂, 100 mM NH₄Cl, 6 mM βME], layered on top of 32 mL sucrose gradients (10%-40% w.v. sucrose in buffer C), and ultracentrifuged at 50,000 x g for 14 hours at 4°C. Fractions containing 70S ribosomes were collected and ultracentrifuged at 100,000g for 17 hours at 4 °C. Ribosome pellets were collected and dissolved in storage buffer [20 mM Tris•HCl (pH

7.0 at 21°C), 10 mM MgCl₂, 100 mM NH₄Cl, 6mM βME]. Ribosomes were stored at -80°C.

The RNC was generated from *in vitro* translation in a membrane-free cell extract prepared from *E. coli* MRE600 as described (67). *In vitro* translation was performed at 37°C for 25 minutes. The translation mix was layered onto a 40 mL sucrose gradient in buffer S1 (10-50% w.v. sucrose in 50 mM HEPES-KOH (pH 7.5 at 4 °C), 100 mM Mg(OAc)₂, 100 mM NH₄Cl) and ultracentrifuged at 4 °C for 15 hours at 23,500 rpm using a SW-32 rotor (Beckman). Fractions containing monoribosome were collected and loaded onto a 1 mL Strep-Tactin sepharose column (IBA, Göttingen Germany) equilibrated with buffer S1 at 4 °C. Buffer S1 containing 2.5 mM desthiobiotin (Sigma) was used to elute RNCs from affinity column. RNC-containing fractions were centrifuged at 55,000 rpm for 3 hours at 4 °C using a TLA-55 rotor (Beckman). Pellets were collected and dissolved in buffer S1 with 25 mM Mg(OAc)₂.

4.6 Supplementary Figures and legends

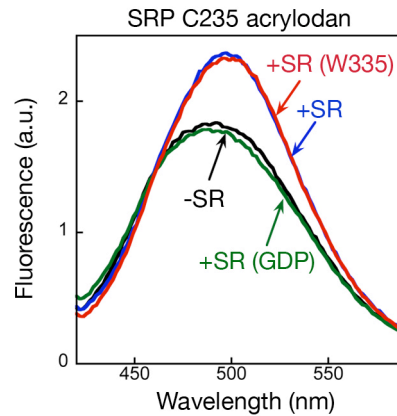


Figure 4.S1. Acrylodan labeled SRP C235 monitors formation of the *closed/activated* conformation. Fluorescence emission spectra are acquired in the presence of GppNHp for acrylodan-labeled SRP C235 alone (0.1 μM ; black), labeled SRP C235 incubated with 1 μM wild type SR (blue), or labeled SRP C235 incubated with 1 μM SR A335W (red), which is blocked in the *closed* \rightarrow *activated* rearrangement and thus isolates the *closed* complex (9), or in the presence of GDP with 10 μM SR (green), which isolates the *early* complex (80).

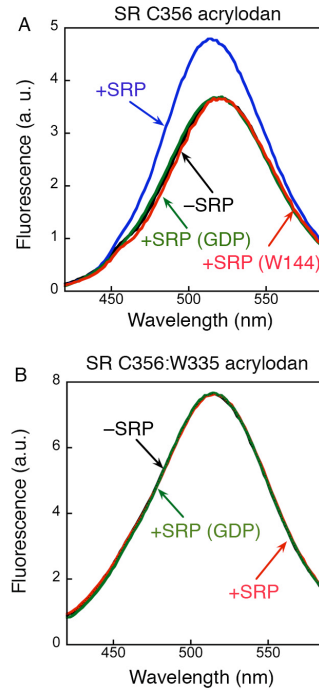


Figure 4.S2. Acrylodan labeled SR C356 specifically monitors formation of the *activated* SRP•SR complex. (A) Fluorescence emission spectra was obtained for acrylodan labeled SR C356 alone (0.1 microM; black), acrylodan labeled SR C356 incubated with wild type SRP (blue) or SRP A144W (red) in the presence of GppNHp, or with 10 microM SRP in the presence of GDP (green). SRP A144W allows a stable *closed* complex to form but specifically blocks formation of the *activated* complex (10). The absence of fluorescence change with SRP A144W shows that acrylodan labeled SR C356 specifically monitors formation of the *activated* complex. (B) Acrylodan labeled C356 does not change fluorescence if mutant SR A355W (9) was used to block the formation of the *activated* complex. Spectra was obtained for 0.1 microM acrylodan labeled SR A335W:C356 alone (black) and when this labeled SR mutant was incubated with 1 microM SRP in the presence of GppNHp (red) or with 5 microM SRP in the presence of GDP (green). The absence of a fluorescence change shows that the probe on SR T356 does not detect the *early* or the *closed* complex.

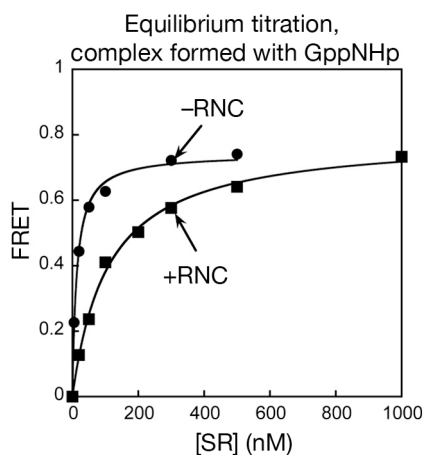


Figure 4.S3. Equilibrium titration of the SRP•SR complex assembled in GppNHp with (■) and without (●) RNC using the FRET assay. Nonlinear least squares fits of data gave K_d values of 14 ± 3 nM (without RNC) and 60 ± 7 nM (with RNC). For cargo-loaded SRP, an accurate determination of the stability of the *closed/activated* states by FRET is complicated by the fact that the stabilities of the SRP•SR complexes assembled with and without GppNHp are very similar (60 vs. 80 nM, respectively), thus a significant fraction of the SRP•SR complex is in the *early* conformation even in the presence of GppNHp. The observed affinity of the cargo•SRP•SR complex of 60 nM is consistent with the weighted average of the stabilities of the *early* intermediate (80 nM, figure 4.4C) and the *closed* complex (40 nM, figure 4.4C) that are equally populated in the presence of GppNHp and cargo.

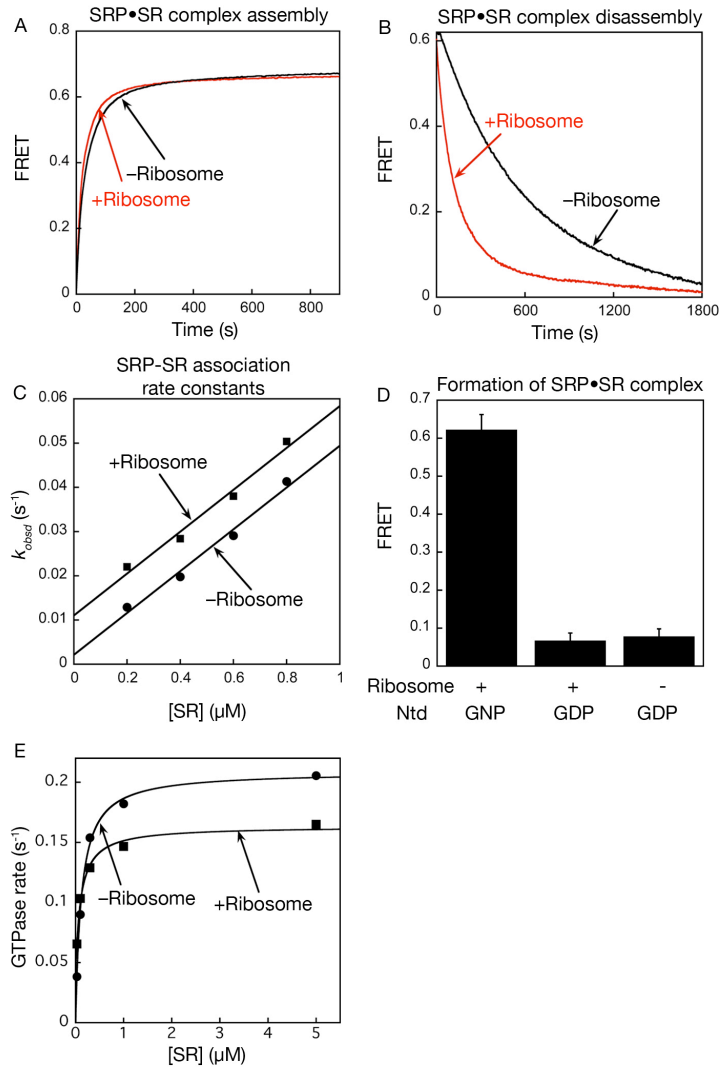


Figure 4.S4. Empty ribosomes do not substantially alter the interaction between SRP and SR. (A) The time course for SRP-SR complex formation, monitored by FRET, in the absence (black) and presence (red) of 0.8 μM ribosomes. Data were obtained with 0.1 μM SRP, 1.0 μM SR, and 100 μM GppNHp. (B) The ribosome accelerates disassembly of the SRP-SR complex ~ 3 fold. The rate constants for complex disassembly were determined in the absence (black) and presence (red) of 1.0 μM ribosomes. Fits of the data to single exponential decay give dissociation rate constants of $0.010 \pm 0.003 \text{ s}^{-1}$ and $0.0027 \pm 0.004 \text{ s}^{-1}$ in the presence and absence of ribosome, respectively. (C) The ribosome does not affect the rate of SRP-SR complex assembly. Association kinetics of the SRP-SR complex was measured as in figure 4.2 with (■) or without (●) 1.0 μM ribosome. Linear fits of the data gave k_{on} values of $4.7 \pm 0.7 \times 10^4 \text{ M}^{-1} \text{ s}^{-1}$ with ribosome and $4.7 \pm 0.4 \times 10^4 \text{ M}^{-1} \text{ s}^{-1}$ without ribosome, and k_{off} values of $0.011 \pm 0.004 \text{ s}^{-1}$ with ribosome and $0.0022 \pm 0.003 \text{ s}^{-1}$ without ribosome. (D) Ribosome does not stabilize the *early* intermediate. FRET values are compared for SRP-SR *early* complex assembled with GDP in the presence and absence of ribosome. Data are obtained with 0.1 μM SRP, ribosome, and 1.0 μM SR. (E) Ribosome does not

substantially affect the stimulated GTP hydrolysis on the SRP•SR complex. GTPase rate constants were measured and analyzed as described in Methods using 15 nM SRP and 50 microM GTP in the absence (●) and presence (■) of 1.0 microM ribosome.

4.7 Acknowledgments

We thank Sandra Schmid, Douglas C. Rees, Raymond Deshaies, Nathan Pierce, and members of the Shan laboratory for comments on the manuscript. This work was supported by NIH grant GM078024 to S.S., and by the Swiss National Science Foundation (SNSF) and the NCCR Structural Biology program of the SNSF to N.B.. S.S. was supported by a career award from the Burroughs Wellcome Foundation, the Henry and Camille Dreyfus foundation, the Beckman Young Investigator award, and the Packard and Lucile award in science and engineering. X.Z. was supported by a fellowship from the Ulric B. and Evelyn L. Bray Endowment Fund

Chapter 5

Sequential Checkpoints Govern Substrate Selection during Co-translational Protein Targeting

A version of this chapter will be published as a Report in Science on May 7th, 2010

X. Zhang, R. Rashid, K. Wang, and S.-O. Shan, Science, (2010), 328, 757-760.

5.1 Abstract

Proper localization of proteins to their correct cellular destinations is essential for all cells. However, the precise mechanism by which high fidelity is achieved in protein localization is not well understood for any targeting pathways. To probe this fundamental question we investigated targeting of proteins by the signal recognition particle (SRP). The “signal hypothesis” postulates that the signal sequence on a protein allows it to be specifically recognized by targeting factors such as SRP, which mediates the delivery of the protein to the correct cellular compartment. It was generally thought that fidelity arises from the inability of SRP to bind strongly to incorrect cargos. Here we show that incorrect cargos are further rejected through a series of fidelity checkpoints during subsequent steps of targeting, including complex formation between the SRP and SRP receptor (SR) and kinetic proofreading through GTP hydrolysis. Thus the SRP pathway achieves a high fidelity through the cumulative effect of multiple checkpoints; this principle may be generally applicable to other complex cellular pathways that need to recognize degenerate signals or discriminate between correct and incorrect substrates based on minor differences.

5.2 Introduction

Co-translational protein targeting by the SRP is an essential and evolutionarily conserved pathway for delivering proteins to cellular membranes (2, 96). SRP recognizes ribosomes translating nascent polypeptide chains (RNCs) as its cargo (figure 5.1A, step 1) (2, 82, 85, 91, 92, 96). Cargo loading enables efficient assembly of an SRP•SR complex through interactions between their GTPase domains, and the cargo stabilizes the

GTPase complex in an *early* conformational state (step 2) (4, 5). The interactions of SR with the target membrane and the protein conducting channel (PCC) is proposed to induce dynamic rearrangements in the SRP•SR complex (5, 85, 92), first to form a GTP-dependent *closed* complex (step 3) and then to activate GTP hydrolysis in the complex (step 4). These rearrangements facilitate the unloading of cargo from SRP to the PCC (steps 3–4) (5, 85, 92). In a productive targeting cycle, GTP is hydrolyzed after cargo unloading to drive the disassembly and recycling of SRP and SR (step 5) (45).

Despite significant progress in our dissection of the SRP pathway as a paradigm for understanding the molecular basis of protein localization, how the SRP ensures faithful delivery of correct cargos remains poorly understood. Like other topogenic sequences that mediate protein localization, signal sequences that engage the SRP lack a consensus motif and are highly divergent (97-99), with a hydrophobic core as their primary distinguishing feature (98, 100). Thus the SRP needs to be highly adaptable; indeed it was proposed that the methionine-rich M-domain of SRP provides a flexible pocket to accommodate diverse signal sequences (15, 101). Nevertheless, the difference in signal sequences of substrates that engage SRP vs. SRP-independent pathways are relatively minor (102). Thus despite its flexibility, the SRP has evolved a strategy to remain highly specific to its substrates. Here we demonstrate that the SRP pathway achieves high fidelity through a combination of binding, induced fit and kinetic proofreading mechanisms.

5.3 Results

It was generally thought that ‘incorrect’ cargos without strong signal sequences are rejected because they bind weakly to the SRP (figure 5.1A, arrow a). To test this hypothesis, we systematically varied the signal sequence based on alkaline phosphatase (phoA), a ‘borderline’ substrate targeted by either the SRP or SecB pathway (102, 103). We replaced the hydrophobic core of the phoA signal sequence (figure 1B, bold) with a combination of leucine and alanine, and varied the Leu/Ala ratio to generate signal sequences with different hydrophobicity (103, 104). As another means to vary the signal sequence and generate an incorrect cargo, the *E. coli* autotransporter EspP was used. Although the EspP signal peptide has a hydrophobicity comparable to that of phoA-3A7L, EspP enters the PCC via an SRP-independent pathway due to the presence of an N-terminal signal peptide extension (figure 5.1B, blue) (105). Firefly luciferase, a cytosolic protein without any identifiable signal sequences, was used as a negative control (figure 5.1B) (103). For all the following experiments, homogeneous stalled RNCs were purified and used as cargos (5, 67).

We first tested the binding affinities of SRP for different cargos. A single cysteine was engineered into the SRP M-domain (C421) and labeled with 5-maleimide-fluorescein (F5M); RNC binding was detected as an increase in the fluorescence anisotropy of SRP(C421)-F5M. SRP binds tightly to the two cargos with the strongest signal sequences (RNC_{1A9L} and RNC_{2A8L}), with equilibrium dissociation constants (K_d) of ~1 nM or less (figure 5.1C and 5.S1). These values are similar to that for an SRP model substrate, RNC bearing the FtsQ signal sequence (figure 5.S1A); thus the behavior of authentic SRP substrates can be recapitulated by the engineered signal sequences. The next strongest

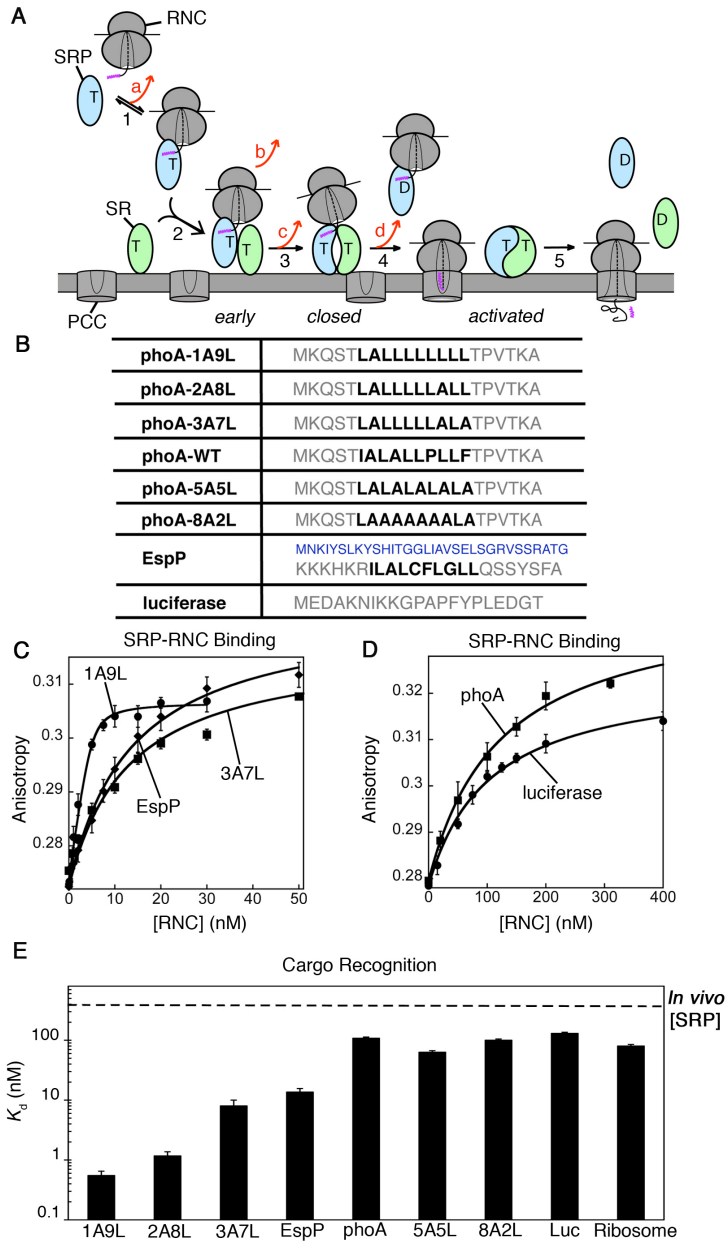


Figure 5.1. Potential fidelity checkpoints in the SRP pathway. (A) Model for potential checkpoints during co-translational protein targeting. A cargo bearing a signal sequence (magenta) enters this pathway upon binding the SRP, and is either retained (black arrows) or rejected (red arrows) at each checkpoint. T and D denote for GTP and GDP, respectively. (B) Signal sequence variants used in this study. Bold highlights the hydrophobic core. Blue denotes the unique N-terminal signal peptide extension in EspP. (C, D) Equilibrium titrations of SRP-RNC binding. Nonlinear fits of data gave K_d values of 0.55, 8.4, 13.6, 108 and 130 nM for RNC_{1A9L} (C, ●), RNC_{3A7L} (C, ■), RNC_{EspP} (C, ◆), RNC_{phoA} (D, ■) and $RNC_{luciferase}$ (D, ●), respectively. (E) Summary of the binding affinities of SRP for different cargos. The dashed line represents the cellular SRP concentration of ~ 400 nM.

cargo, RNC_{3A7L}, also exhibits strong albeit attenuated binding to SRP, with $K_d \sim 10$ nM (figure 5.1C). Cargos with even weaker signal sequences bind the SRP another 10 fold weaker (figure 5.1, D-E, and figure 5.S1). Nevertheless, the affinity of incorrect cargos or the empty ribosome for SRP is still substantial, with K_d 's of 80 – 100 nM. In comparison, signal peptides bind SRP with K_d 's in the micromolar range (35, 106). Thus interactions with the ribosome are important for recruiting the SRP to the cargo (82, 85, 91, 107). As the cellular SRP concentration is ~ 400 nM (83), at least four fold higher than the K_d values of SRP for even the weakest cargos (figure 5.1E, dashed line), a substantial amount of incorrect cargos could be bound at this SRP concentration. To our surprise, although EspP is not an SRP substrate, RNC_{EspP} binds SRP as tightly as RNC_{3A7L} (figure 5.1C). Thus the differences in cargo binding affinity may not provide sufficient discrimination against incorrect cargos, and additional factors in the bacterial cytosol do not increase the specificity of SRP-cargo binding (figure 5.S2) (108).

Besides SRP, the PCC also discriminates against incorrect cargos (109, 110). Nevertheless, the PCC mediates translocation of proteins from both the SRP- and SecB-pathways, including EspP (111), and hence is unlikely to be solely responsible for the stringent substrate selection by the SRP. We postulated that incorrect cargos could be less efficient during subsequent steps of targeting; these steps thereby provide additional checkpoints to help reject incorrect cargos (112). We tested several potential checkpoints: (i) Formation of the *early* SRP•SR complex (figure 5.1A, step 2), an obligatory intermediate preceding the formation of subsequent complexes (4, 5). This intermediate is highly unstable with free SRP, and >98% of it dissociates before rearranging into the subsequent complex. A strong cargo stabilizes the *early* intermediate and prevents its

premature disassembly (5). If incorrect cargos could not provide such a stabilization, then their *early* targeting complexes would be more likely to disassemble and exit the SRP pathway prematurely (figure 5.1A, arrow b). (ii) Rearrangement of the *early* intermediate to the *closed* complex (figure 5.1A, step 3), which is essential for switching the SRP from a cargo-binding to a cargo-releasing mode and primes the cargo for unloading (5). If incorrect cargos were less efficient in this rearrangement, then their late stages of targeting would be delayed (figure 5.1A, arrow c). (iii) GTP hydrolysis from the SRP•SR complex, which occurs rapidly in the absence of cargo (66). A strong cargo could delay GTP hydrolysis, providing the cargo•SRP•SR complex an important time window to search for the target membrane and the PCC before GTP hydrolysis drives the irreversible disassembly of the targeting complex (figure 5.1A, steps 4 vs. 5) (5). If incorrect cargos could not delay GTP hydrolysis as effectively, they would be more likely to be rejected through premature GTP hydrolysis (figure 5.1A, arrow d). This would further improve the fidelity of targeting via kinetic proofreading.

To test whether the *early* SRP•SR complex is stabilized more strongly by the correct than the incorrect cargo, we assembled cargo•SRP•SR *early* complexes in the absence of nucleotides; this blocks the rearrangement of the GTPase complex to subsequent conformations and allows us to isolate this intermediate (4, 5). The equilibrium stabilities of the *early* complexes were measured using fluorescence resonance energy transfer (FRET) between donor- and acceptor-labeled SRP and SR (4). In this and all the following experiments, saturating RNCs were used to ensure that 80 – 99% of the SRPs are loaded with cargo, such that differences in cargo binding affinities are bypassed. The *early* complex is significantly stabilized by RNC_{1A9L} and RNC_{2A8L},

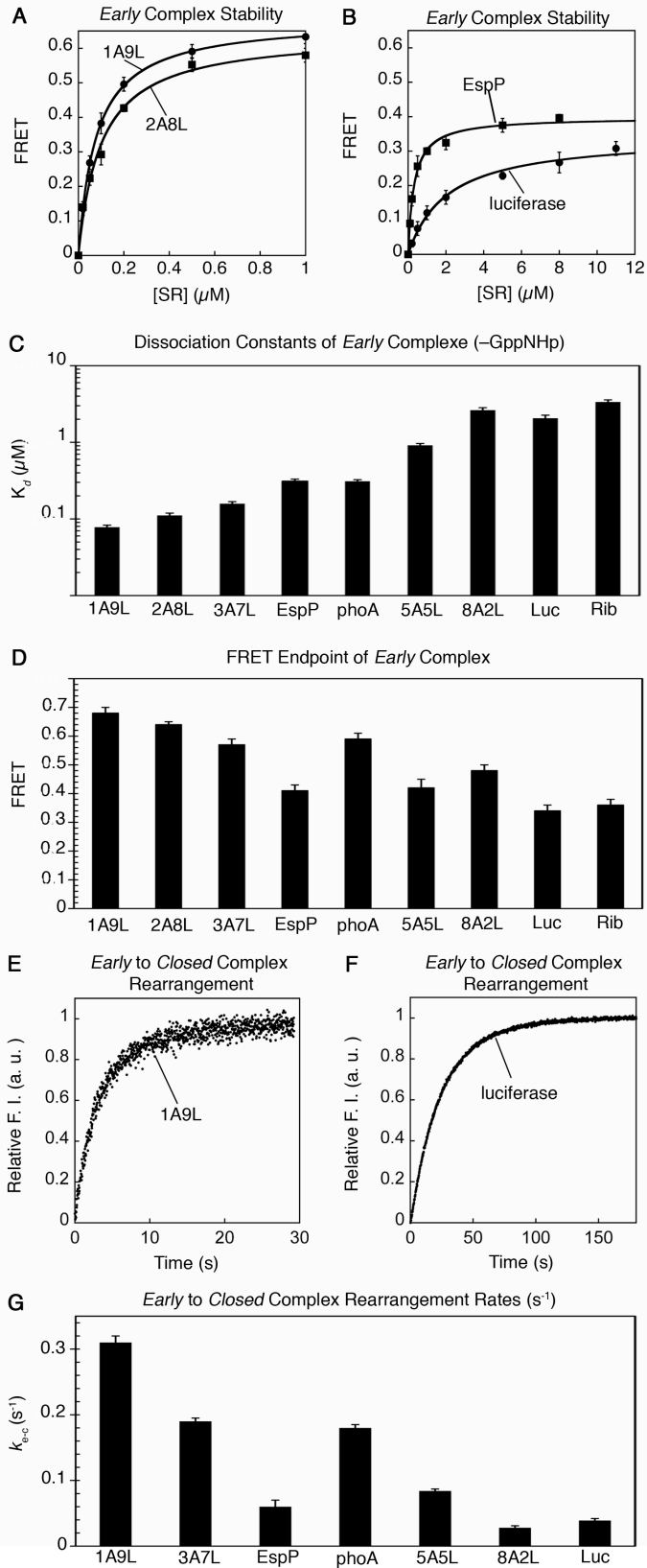


Figure 5.2. Correct cargos stabilize the *early* intermediate and mediate faster rearrangement to the *closed* complex. (A, B) Equilibrium titrations of the *early* intermediate. Nonlinear fits of data gave K_d values of 78, 110, 311 and 2060 nM and FRET endpoints of 0.68, 0.64, 0.41, and 0.34 for RNC_{1A9L} (A, ●), RNC_{2A8L} (A, ■), RNC_{EspP} (B, ■), and RNC_{luciferase} (B, ●), respectively. (C, D) Summary of the K_d values (C) and FRET end points (D) of the *early* intermediates formed by different cargos. (E, F) Measurements of the *early* → *closed* rearrangement. Nonlinear fits of data gave rate constants of 0.31 s⁻¹ with RNC_{1A9L} (E) and 0.039 s⁻¹ with RNC_{luciferase} (F). (G) Summary of the rate constants for the *early* → *closed* rearrangement with different cargos.

with $K_d \sim 80$ nM (figure 5.2A), and this stability is severely compromised for the weaker cargos (figure 5.2, B-C, and figure 5.S3). Further, with incorrect cargos such as RNC_{EspP} and RNC_{luciferase}, the FRET efficiency plateaus at a lower value, $\sim 0.3 - 0.4$ (figure 5.2, B and D, and figure 5.S3), compared to ~ 0.66 with the correct cargos (figure 5.2, A and D). This and the slower rate at which these *early* complexes rearrange to the *closed* state (see below) suggest that the SRP and SR are likely mispositioned in the *early* targeting complexes formed by the incorrect cargos. Thus weak or incorrect cargos do not induce the formation of a stable and productive *early* complex, and are more likely to exit the pathway prematurely (figure 5.1A, arrow b).

To test whether the rearrangement to the *closed* complex is more efficient with the correct than the incorrect cargos (figure 5.1A, step 3), we used acrylodan-labeled SRP(C235), which specifically detects formation of the *closed* complex (5). We preformed the *early* targeting complex in the absence of nucleotides and in the presence of saturating cargo and SR, and monitored its rearrangement into the *closed* complex upon addition of the GTP analogue 5'-guanylylimido-diphosphate (GMPPNP). With RNC_{1A9L}, this rearrangement is fast, occurring at 0.3 s⁻¹ (figure 5.2E). RNC_{3A7L} and RNC_{phoA} mediated this rearrangement 40% slower (figure 5.2G and 5.S4). Notably, RNC_{EspP} and cargos weaker than RNC_{5A5L} mediate this rearrangement 5–10 fold slower

than RNC_{1A9L} (figure 5.2, F-G, and figure 5.S4). The slower rate of the *early* \rightarrow *closed* rearrangement observed with these cargos correlated with their lower FRET value in the *early* intermediate (figure 5.2D), suggesting that efficient rearrangement to the *closed* complex requires formation of an *early* intermediate in a productive conformation.

The more favorable pre-equilibrium to form the *early* intermediate combined with the faster *early* \rightarrow *closed* rearrangement would allow the correct cargos to mediate GTP-dependent SRP-SR complex assembly at much faster rates (figure 5.1A, steps 2-3). We characterized this cumulative effect using both FRET (figure 5.3, A-C, and figure 5.S5, F-G) and acrylodan-labeled SRP(C235) (figure 5.S5). Both probes demonstrated that the correct cargos mediate rapid SRP-SR complex assembly with GMPPNP (figure 5.3A and 5.S5A), and this rate decreases significantly as the signal sequence becomes weaker (figure 5.3B-C, and figure 5.S5). Both assays revealed a $\sim 10^3$ fold discrimination between the strongest (e.g., RNC_{1A9L}) and weakest (e.g., RNC_{EspP} & RNC_{8A2L}) cargos in the kinetics of GTP-dependent complex assembly (figure 5.3C and 5.S5E). This is consistent with the cumulative effect of the over 50 fold more stable *early* intermediate (figure 5.2C) and the ~ 10 fold faster rate at which this intermediate rearranges to the *closed* complex (figure 5.2G) with the correct than the incorrect cargos.

To test whether the correct cargos delay GTP hydrolysis more effectively than the incorrect cargos, we determined the rate of the GTPase reaction from the cargo•SRP•SR complexes. RNC_{1A9L} and RNC_{2A8L} reproducibly delay GTP hydrolysis 6–8 fold (figure 5.3D and 5.S6). The next strongest cargo, RNC_{3A7L} , has a smaller but still substantial inhibitory effect on the GTPase reaction (figure 5.S6). In contrast, incorrect cargos such as RNC_{EspP} inhibit GTP hydrolysis by less than two fold, and $\text{RNC}_{\text{luciferase}}$ does not

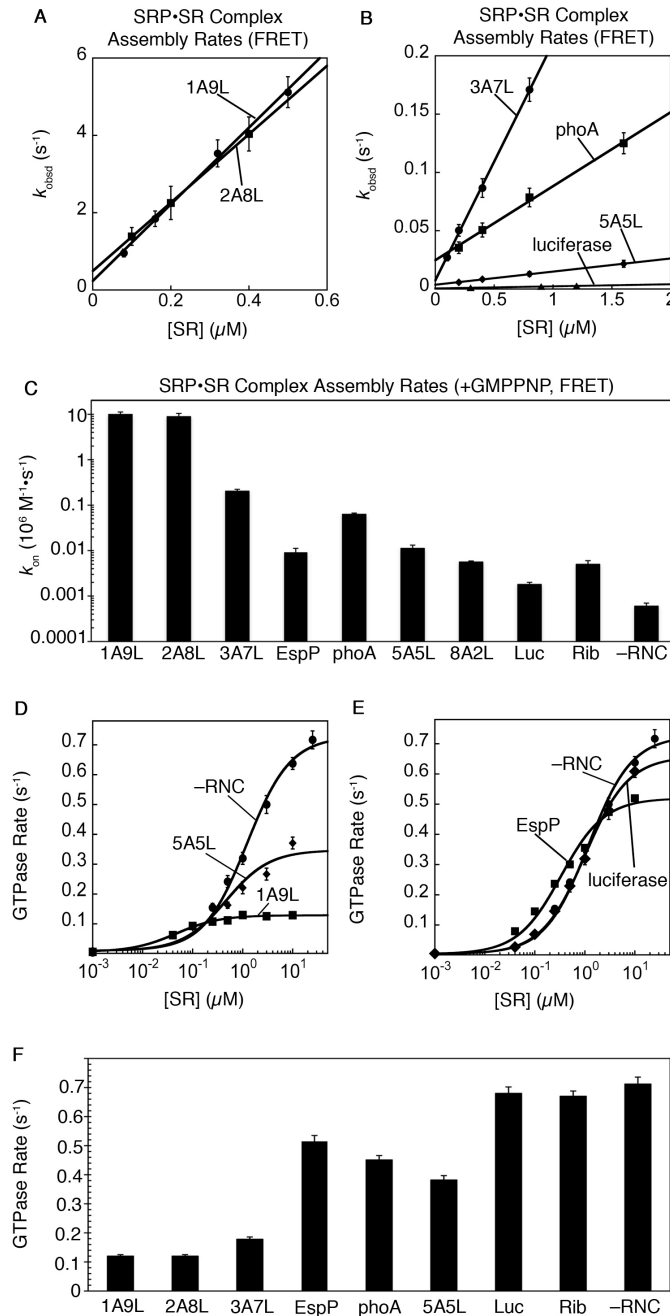


Figure 5.3. Correct cargos accelerate GTP-dependent complex formation but delay GTP hydrolysis. (A, B) Rate constants of SRP-SR complex assembly in GMPPNP measured by FRET. k_{on} values of 9.9×10^6 , 8.8×10^6 , 2.0×10^5 , 2.2×10^4 , 1.1×10^4 and 1.8×10^3 $M^{-1}s^{-1}$ for RNC_{1A9L} (A, ●), RNC_{2A8L} (A, ■), RNC_{3A7L} (B, ●), RNC_{phoA} (B, ■), RNC_{5A5L} (B, ◆) and RNC_{luciferase} (B, ▲), respectively. (C) Summary of GTP-dependent complex assembly rate constants with different cargoes. (D, E) Effects of cargo on GTP hydrolysis from the SRP-SR complex. k_{cat} are 0.72 s^{-1} without cargo (●), and 0.11 , 0.34 , 0.51 , and 0.65 s^{-1} with RNC_{1A9L} (D, ■), RNC_{5A5L} (D, ◆), RNC_{EspP} (E, ■) and RNC_{luciferase} (E, ◆), respectively. (F) Summary of GTPase rate constants in the presence of different cargoes.

significantly affect the GTPase rate (figure 5.3, E-F, and figure 5.S6). These results are consistent with the hypothesis that the fidelity of protein targeting can be further improved through kinetic proofreading mechanisms by using the energy of GTP hydrolysis (figure 5.1A, arrow d).

These results demonstrate that the SRP pathway discriminates against incorrect cargos not only through binding affinity, but also through differences in the kinetics of SRP-SR complex assembly and GTP hydrolysis. Another important determinant of co-translational protein targeting is the length of the nascent polypeptide, as the SRP loses its ability to target substrates when the nascent chain exceeds ~110 residues (87, 113). Since the bacterial SRP does not arrest translation (2), this gives a ~3 second time window for the SRP to complete protein targeting (112), assuming that SRP begins to recognize cargos when the nascent chain is ~35 amino acids long and a translation elongation rate of ~20–30 amino acids/second in bacteria (114). Based on this time constraint and the rate and equilibrium constants determined here, we calculated the amount of substrates retained in the SRP pathway after each checkpoint (figure 5.4A). The cargo binding step is not sufficient to discriminate against incorrect cargos, allowing over 75% of them to enter the SRP pathway (figure 5.4A, light grey). During cargo delivery through GTP-dependent SRP-SR complex assembly, a large portion of substrates weaker than *phoA* are rejected (figure 5.4A, dark grey). Finally, kinetic competition between GTP hydrolysis and cargo unloading allows most of the incorrect substrates to be rejected, whereas the majority of substrates stronger than *phoA*-3A7L are retained (figure 5.4A, black).

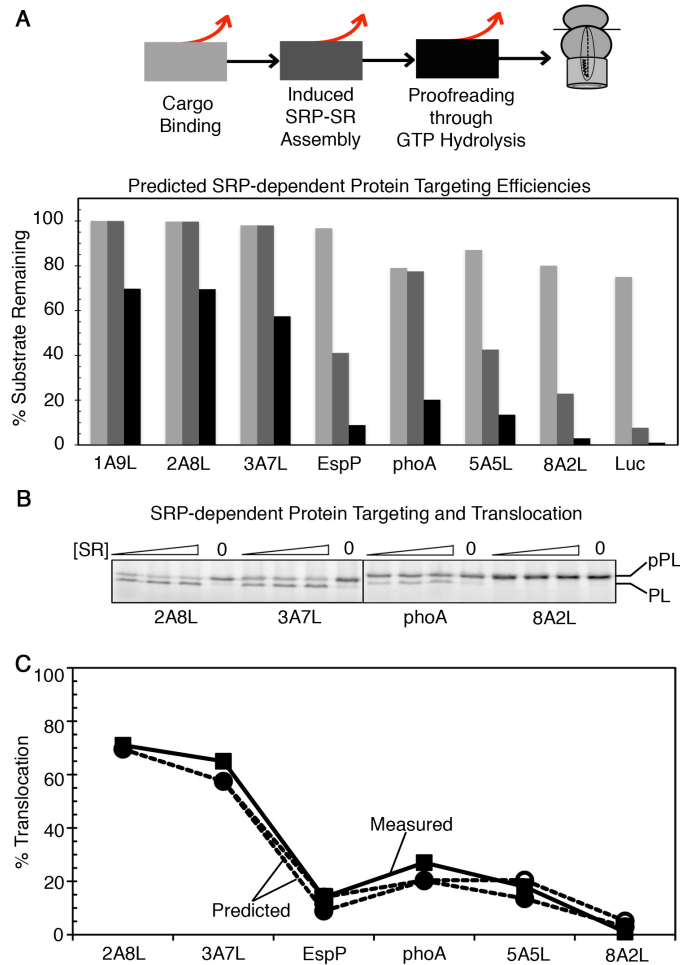


Figure 5.4. Stepwise rejection of weak or wrong cargos from the SRP pathway. (A) The fraction of cargos remaining in the SRP pathway after each step, calculated as described in the Methods. As depicted in the top panel, cargos are either retained (black arrow) or rejected (red arrow) from the pathway during cargo binding (light grey), induced SRP-SR assembly (dark grey), and proofreading through GTP hydrolysis (black). (B) SRP-dependent protein targeting and translocation of substrates with different signal sequences analyzed by SDS-PAGE. pPL and PL denote the precursor and signal sequence-cleaved forms of the substrate, respectively. (C) Predicted protein targeting efficiencies (● and ○) agree well with the experimentally determined values (■), quantitated from the data in (B). Translation elongation rates of 20 (●) and 10 amino acids/s (○) were used for the *E. coli* and eukaryotic ribosomes, respectively, to calculate the targeting efficiencies. The small discrepancies between the measured and calculated targeting efficiencies based on *E. coli* ribosomes could be rationalized by a slower translation rate of eukaryotic ribosome used in the assay than that of *E. coli* ribosome used in the calculations (115), which gives the SRP and SR a longer time window for complex assembly. This discrepancy became smaller when the calculation was performed using the translation rate of eukaryotic ribosomes (○).

To test the validity of this analysis, we determined the targeting efficiency of proteins with various signal sequences using a well-established assay that tests the ability of *E. coli* SRP and SR to mediate the co-translational targeting of preproteins to microsomal membranes (44, 116). Cleavage of preprolactin (pPL) signal sequence provides readout for successful targeting and translocation (figure 5.4B). Bacterial SRP and SR mediate pPL targeting as efficiently as their mammalian homologues despite the heterologous nature of this assay (44); this highlights the remarkable conservation of the SRP pathway and allows us to test insights from biophysical studies of bacterial SRP and SR in the context of a complete and functional targeting reaction. Importantly, as both reaction substrates and products are quantitated, this assay provides the most accurate measure of targeting efficiency. Substrates with signal sequences stronger than 3A7L are efficiently targeted and translocated (figure 5.4B and 5.S7). In contrast, substrates with the EspP signal sequence or signal sequences weaker than phoA show severe defects in translocation, and almost no translocation was detected for the phoA-8A2L substrate (figure 5.4B). Remarkably, the experimentally determined protein targeting efficiencies agree well with predictions based on the kinetic and thermodynamic measurements (figure 5.4C), suggesting that our model (figure 5.1A) faithfully represents the way SRP handles its substrates.

5.4 Discussion

Our work supports a novel model in which fidelity is achieved during co-translational protein targeting through the cumulative effect of multiple checkpoints, by using a combination of binding, induced fit, and kinetic proofreading mechanisms. With

correct substrates, loading of cargo is coupled to its rapid delivery (through accelerated complex assembly) and productive unloading (through delayed GTP hydrolysis); whereas with incorrect cargos stable SRP-SR complex assembly is extremely slow, but once the stable complex is formed rapid GTP hydrolysis immediately drives its disassembly. These differences in downstream steps strongly suggest that incorrect cargos bind the SRP in a less productive mode than the correct cargos (92). The lack of productive interactions with the signal sequence did not lead to complete rejection of incorrect cargos during the initial binding step, but were detected during subsequent steps and discriminated repeatedly. This conclusion is most strongly supported by the case of EspP, which binds SRP strongly but is rejected primarily by kinetic discrimination in the complex assembly and GTP hydrolysis steps. Our analyses here focused on how the SRP handles each substrate in a single round of targeting. *In vivo*, a higher fidelity could be achieved during multiple rounds of targeting and with competition between correct and incorrect cargos. In addition, the PCC provides another important checkpoint to discriminate against incorrect cargos such as phoA-8A2L (109, 110); we could not detect this additional discrimination as the targeting efficiency of this substrate before arrival at PCC is already $\leq 1\%$.

Our findings are analogous to those observed in tRNA selection during translation, in which a mismatch between the mRNA and tRNA anticodon at the ribosome active site leads not only to weaker binding affinities for the noncognate and near-cognate tRNAs, but also to slower rates of subsequent steps and higher frequency of rejection of the non- and near-cognate tRNAs (117, 118). Similar strategies of using multiple checkpoints to ensure fidelity have been demonstrated by pioneering work on

tRNA synthetases (*119*) and DNA and RNA polymerases (*120, 121*), and likely represents a general principle for complex cellular pathways, especially those that need to recognize degenerate signals or to discriminate between substrates based on minor differences.

5.5 Materials and Methods

5.5.1 Materials

The *E. coli* SRP and SR GTPases (Ffh and FtsY, respectively), trigger factor, and 4.5S RNA were expressed and purified as described previously (66, 122). FtsY(47-497) was used in all the fluorescence measurements, and full length FtsY was used in GTPase rate measurements. The abilities of FtsY(47-497) to interact with SRP and respond to the cargo are similar to those of full length FtsY (5). Single cysteine mutants of Ffh and FtsY were constructed using the QuickChange mutagenesis procedure (Stratagene), and were expressed and purified using the same procedure as that for the wild-type proteins. Fluorescent dyes N-(7-dimethylamino-4-methylcoumarin-3-yl)maleimide (DACM), fluorescein-5-maleimide (F5M), and BODIPY-FL-N-(2-aminoethyl)-maleimide were from Invitrogen.

5.5.2 Signal sequence mutants

Plasmids encoding signal sequence variants were constructed based on pUC19StrepFtsQSecM (67), composed of a strep3 tag in the N terminus, the first 74 amino acids of FtsQ, and a translation stall sequence from SecM (residues 136-166). For this work, FtsQ (1-74) was replaced with the first 50 residues of phoA or firefly luciferase, and mutations were introduced into the hydrophobic core of phoA (figure 1B in main text) using the QuickChange mutagenesis procedure (Stratagene).

5.5.3 RNC and ribosome purification

70S ribosomes were purified from *E. coli* MRE600 cells following established

protocols (5, 95). Homogeneous RNCs were generated from *in vitro* translation reactions using membrane free cell extract prepared from MRE600 cells, and purified through affinity chromatography and sucrose gradient centrifugation as described previously (5, 95). RNCs purified using this method can bind SRP, TF, and the secYEG complex (67) and in quantitative assays, exhibit the same affinity for SRP as those measured with RNCs that do not contain an affinity tag (68).

5.5.4 SRP- and ribosome-free *E. coli* (-*ffh*) total cytoplasmic extract

The bacterial strain HDB51 MC4100 *ara+* *secB+* *zic-4901::Tn10 ffh::kan-1* λ (Para-*ffh* Apr), in which the expression of Ffh is under the control of arabinose promoter, was a generous gift from Harris D. Bernstein at NIDDK, NIH (123). Bacterial culture was grown at 37 °C in the absence of arabinose for 4-5 generations so that more than 90% of endogenous Ffh was depleted (123). Cells were harvested at OD₆₀₀ = 0.70. The cell pellet was washed with 0.1M Tris•HCl buffer (pH 8.0), and resuspended in lysis buffer [0.1M Tris•HCl, 20% sucrose, 1mM phenylmethylsulphonyl fluoride (PMSF), and 50 µg/mL lysozyme] for 90 minutes at room temperature. MgCl₂ was then added to stabilize the spheroplasts at a final concentration of 20 mM. The mix was spun at 8000 rpm for 10 min to separate spheroplasts from the periplasmic fraction. The spheroplasts were washed twice in buffer containing 0.1M Tris•HCl (pH 8.0), 20% sucrose, and 20 mM MgCl₂, resuspended in PBS containing 1mM PMSF, and passed through French Press three times at 10,000 psi. The lysate was clarified by centrifugation at 8000 rpm for 10 minutes, and ultracentrifuged twice at 320,000 g for 3 hours at 4°C to remove membranes and ribosomes. The supernatant was collected as the cytosolic extract.

5.5.5 Fluorescence labeling

For FRET measurements, DACM and BODIPY-FL were used to label single-cysteine mutants of Ffh and FtsY, respectively, as described previously (4). For measurements using environmental sensitive probes, acrylodan was used to label Ffh(C235) as described (5). For fluorescence anisotropy measurements, F5M was used to label Ffh(C421). Fluorescence labeling with F5M followed the same procedure as those for DACM and BODIPY-FL. Labeled protein was purified as described (4), and the concentration of labeled protein was determined using an absorption extinction coefficient of $\epsilon_{504} = 83,000 \text{ M}^{-1} \text{ cm}^{-1}$ for F5M. The efficiency of labeling was typically $\geq 95\%$ with a background of $< 5\%$.

5.5.6 Fluorescence anisotropy measurements

Anisotropy measurements used an excitation wavelength of 450 nm and emission wavelength of 518 nm. Fluorescence anisotropy was calculated according to Eq. 5.1:

$$R = \frac{(I_{VV} - G \times I_{VH})}{(I_{VV} + 2G \times I_{VH})} \quad (5.1)$$

in which I_{VV} and I_{VH} are the vertically and horizontally polarized emission intensities when the sample is vertically excited, G is the grating factor that corrects for the wavelength response to polarization of the emission optics and detectors, defined as $G = I_{HV}/I_{HH}$, where I_{HV} and I_{HH} are the vertically and horizontally polarized emission intensities when the sample is horizontally excited.

5.5.7 Fluorescence measurements

All measurements were carried out at 25 °C in assay buffer [50 mM KHEPES, pH 7.5, 150 mM KOAc, 10 mM Mg(OAc)₂, 2 mM DTT] on a Fluorolog-3-22 spectrofluorometer (Jobin Yvon, Edison, NJ). The detergent Nikkol, which was used in previous work, was not used for studies of complex assembly in this work. The stimulatory effects of strong SRP cargos can be observed without removing Nikkol (4), and the same SRP-SR complex assembly rate constants and stability of the *early* complex was observed with the strong cargos (RNC_{1A9L}, RNC_{2A8L}, and RNC_{3A7L}) with or without Nikkol present. On the other hand, Nikkol obscures the small stimulatory effects from weak cargos or the empty ribosome, as the complex assembly rate constant between free SRP and SR is ~100 fold faster in the presence of Nikkol (106).

FRET measurements were carried out using an excitation wavelength of 380 nm and an emission wavelength of 470 nm. FRET efficiency was calculated as described (4). For measurements using acrylodan-labeled SRP(C235), an excitation wavelength of 380 nm was used and fluorescence emission at 500 nm was monitored (5).

5.5.8 Strategy to isolate individual reaction steps during protein targeting

This section describes how the individual reaction rate or equilibrium constants were isolated using the principles of rate laws, rate-limiting steps, the rules of thermodynamics and mass action, and the information acquired for a previous reaction step. In general, each time a subsequent reaction step was measured, reaction conditions were designed such that all the cargos have passed the previous steps.

5.5.8.1 Cargo binding to the SRP (figure 1A, step 1)

The equilibrium binding affinity of SRP for various cargos was determined by equilibrium titration using the change in the fluorescence anisotropy of F5M-labeled SRP(C421). In general, 5 – 20 nM SRP and 100 μ M GMPPNP were used in the titrations. We found that cargos bind to and dissociate from the SRP on a time scale faster than manual mixing (30 sec – 1 min). Therefore, all samples were incubated for 2 – 5 minutes to ensure that equilibrium has been established. In each measurement, increasing amounts of cargo were added to a fixed amount of fluorescently labeled SRP. The anisotropy value (A) at different SRP concentrations were plotted as a function of cargo concentration ($[RNC]$). The data were fit to single binding (Eq. 5.2) or quadratic (Eq. 5.3) equations,

$$A = A_0 + (A_1 - A_0) \times \frac{[RNC]}{K_d + [RNC]} \quad (5.2)$$

$$A = A_0 + (A_1 - A_0) \left\{ \frac{c_0 + [RNC] + K_d - \sqrt{(c_0 + [RNC] + K_d)^2 - 4c_0[RNC]}}{2c_0} \right\} \quad (5.3)$$

in which A_0 is the anisotropy value of free SRP, A_1 is the anisotropy value when SRP is bound to cargo, c_0 is the concentration of total SRP, and K_d is the equilibrium dissociation constant of SRP for the RNC. No significant changes were found in fluorescence intensity of free- and bound-SRP after photo-bleaching effect was corrected.

5.5.8.2 Formation of the SRP•SR early intermediate (figure 1A, step 2)

During the measurement of this and all subsequent steps, all reactions were carried out in the presence of saturating cargo concentrations (100 nM RNC_{1A9L} and

RNC_{2A8L}, 200 nM RNC_{3A7L} and RNC_{EspP}, 500 nM RNC_{phoA}, RNC_{5A5L} and RNC_{8A2L}, 600 nM RNC_{luciferase}, and 1 μ M ribosome). This ensures that 80–99% of the SRP are bound to the cargos so that the differences in cargo binding affinities contribute less than 20% to our measurements.

Our previous work showed that the rate constant of *early* complex formation is rapid and affected only two fold by a strong cargo, and that the primary effect of cargo is on the stability of the *early* complex. We therefore measured the equilibrium stability of the *early* complex formed by different cargos using the FRET assay. Equilibrium titrations were carried out in the presence of a small, fixed amount of RNC-bound, donor-labeled SRP and increasing amounts of acceptor-labeled SR in the absence of GTP or GTP analogues. Equilibrium was established upon manual mixing. FRET efficiency was calculated as described and plotted as a function of SR concentration ([SR]). The data were fit to Eq. 5.4,

$$E = E_1 \times \frac{[\text{SR}]}{K_d + [\text{SR}]} \quad (5.4)$$

in which E_1 is the FRET value (end point) when all the cargo•SRP complexes are bound to SR, and K_d is the equilibrium dissociation constant of the *early* intermediate.

The early \rightarrow *closed* rearrangement (figure 1A, step 3). This rearrangement was measured using acrylodan-labeled SRP(C235), which specifically detects the *closed* complex (5). The *early* cargo•SRP•SR complexes were pre-assembled in the presence of 0.1 – 0.25 μ M acrylodan-labeled SRP(C235), saturating cargo and SR with respect to their K_d values, and in the absence of nucleotides. An excess of GMPPNP (400 μ M) was added to initiate the rearrangement to the *closed* complex and the fluorescence intensity of

acrylodan (I) was monitored over time. The time courses were single exponential and fit to eq 5.5,

$$I(t) = I_1 + (I_0 - I_1) \times \exp(-k_{obsd}t) \quad (5.5)$$

in which I_0 is the fluorescence before addition of GMPPNP, I_1 is the fluorescence value at $t \rightarrow \infty$, and k_{obsd} is the observed rate constant. In all cases, we ensured that SR concentrations were sufficiently high such that the values of k_{obsd} were independent of SR concentration, confirming that the unimolecular rearrangement within the GTPase complex was isolated. With free SRP, this method gives the same rate constant for this rearrangement (1.5 s^{-1}) as that previously measured during a continuous FRET assay in which the *early* complex was not first stalled by leaving out GTP ($1-2 \text{ s}^{-1}$) (4). Further, when acrylodan-labeled SRP(C235) was used to monitor SRP-SR complex assembly with RNC_{1A9L}, at high SR concentrations the observed assembly rate constant deviated from linearity and plateaued, indicating that the reaction was rate limited by the early to closed rearrangement at saturating SR concentrations. The rate of the rearrangement obtained from this plateau was 0.34 s^{-1} (figure 5.S9), comparable to that of 0.31 s^{-1} measured using the pulse-chase experiment (figure 5.2E and G in main text). Together, the remarkable agreement between the different methods indicates that: (i) the *early* intermediate isolated in the absence of nucleotides is kinetically competent for subsequent rearrangements; and (ii) our approach of isolating the *early* intermediate and chasing it to the *closed* complex provides a valid method to measure the rate of this conformational rearrangement.

Rate constants for GTP-dependent SRP-SR complex assembly (figure 1A, steps 2+3). The

second-order rate constant for SRP-SR association to form the GTP-stabilized *closed* complex was measured using acrylodan-labeled SRP(C235). A constant concentration of cargo-bound, labeled SRP was mixed with varying concentrations of SR to initiate complex assembly, and the changes in the fluorescence of acrylodan-labeled SRP(C235) was monitored over time. The data were fit to Eq. 5.5 above to obtain the observed rate constants (k_{obsd}) at individual SR concentrations. The values of k_{obsd} were plotted as a function of SR concentrations of SR ($[SR]$) and fit to Eq. 5.6,

$$k_{obsd} = k_{on} \cdot [SR] + k_{off} \quad (5.6)$$

in which k_{on} and k_{off} are the rate constants for complex assembly and disassembly, respectively. Fast reactions were measured on a Kintek stopped-flow apparatus. As an independent way to measure the second order rate constant for stable SRP-SR complex assembly, FRET instead of the environmentally sensitive probes was used and the rate constants were determined analogously. The conditions for measuring complex assembly rate constants are: 100 μ M GMPPNP; 80 nM SRP and 100 nM RNC_{1A9L} or RNC_{2A8L}; 100 nM SRP and 200 nM RNC_{3A7L} or RNC_{EspP}; 200 nM SRP and 500 nM RNC_{phoA}, RNC_{5A5L} or RNC_{8A2L}, 300 nM SRP and 600 nM RNC_{luciferase}.

These two methods provide independent and complementary information about the rate constants of complex assembly. Acrylodan-labeled SRP(C235) allows us to specifically measure the assembly rate of the *closed* complex. FRET, on the other hand, reports on the formation of a stable targeting complex that includes both the *early* and *closed* conformational states. For most of the cargos, these two methods yield the same rate constants within experimental error (cf. figure 5.3C vs figure 5.S5E). For RNC_{1A9L} and RNC_{2A8L}, the rate constants measured by FRET is ~10 fold faster than by

acrylodan-labeled SRP(C235). This is because with these two cargos, the *early* intermediate is similar in stability to the *closed* complex; hence the SRP•SR complex formed by these cargos in GMPPNP is a roughly equal mixture of the *early* and *closed* states, both of which are detected by FRET but only the latter was detected by acrylodan-labeled SRP(C235). Because stable complex formation bypasses the *early* → *closed* rearrangement with these two cargos, their rate constant for GTP-dependent complex assembly detected by FRET is faster than that detected by acrylodan-labeled SRP(C235). In contrast, for cargos weaker than RNC_{3A7L}, the *closed* complex is the predominant conformation and its formation was monitored by both probes. Because complex assembly is rapid and not rate-limiting for the GTPase cycles and for protein targeting with RNC_{1A9L} and RNC_{2A8L}, roughly the same results (with differences of <2%) were obtained in numerical analysis of their protein targeting efficiencies regardless of whether the complex assembly rate constants measured by the FRET or acrylodan probes were used for the calculation.

GTP hydrolysis from the SRP•SR complex (figure 1A, step 4). The GTPase assay to measure the stimulated GTP hydrolysis reaction between SRP and FtsY was carried out and analyzed as described (66). 40 – 50 nM SRP were loaded with cargo in the presence of increasing SR concentrations, and the reactions were initiated by addition of 100 μM GTP doped with γ -³²P-GTP. The SR concentration dependence of the observed GTPase rate constant (k_{obsd}) was fit to eq. 5.7,

$$k_{obsd} = k_{cat} \times \frac{[SR]}{[SR] + K_m} \quad (5.7)$$

in which k_{cat} is the rate constant at saturating SR concentration, and K_m is the SR

concentration required to reach half saturation. It should be noted that in this assay, the observed rate constants at subsaturating SR concentrations represents the second order reaction: $\text{GTP}\cdot\text{SRP} + \text{SR} \cdot\text{GTP} \rightarrow 2\text{GDP} + 2\text{P}_i$, and is rate-limited by complex assembly between the SRP and SR. The rate constant observed at saturating SR concentrations (k_{cat}) represents the GTPase rate constant from a fully formed, stable cargo•SRP•SR complex, and is the parameter relevant in this study. Nikkol was included in the GTPase assay as the rate of GTP hydrolysis from the SRP•FtsY complex was not affected by Nikkol (106), and inclusion of Nikkol allows saturation to be achieved at much lower FtsY concentrations.

5.5.9 Co-translational protein targeting and translocation

A previously established heterologous protein targeting assay (44, 116), based on the ability of *E. coli* SRP and FtsY to mediate the targeting of preprolactin (pPL) to microsomal membranes, was used in this study. Bacterial SRP and SR mediate pPL targeting as efficiently as their mammalian homologues despite the heterologous nature of this assay (44); this highlights the remarkable conservation of the SRP pathway and allows us to test insights from biophysical studies of bacterial SRP and SR in the context of a complete and functional targeting reaction. Importantly, as both substrates and products are quantitated, this assay provides the most accurate measure of targeting efficiency. Therefore, it is by far the most suitable assay for the purpose of this study.

ER microsomal membranes have been washed with EDTA, high salt, and digested with trypsin to remove the endogenous SRP and SR, as described previously (44). 200 nM SRP and 4 equiv. of washed and trypsin-digested microsomal membrane

were used in the targeting reaction. *E. coli* SRP binds to *E. coli* ribosomes with similar affinity ($K_d = 80$ nM) as those measured previously for the binding of SRP to wheat germ ribosomes ($K_d = 71$ nM) (87). Further, *E. coli* SRP and FtsY can mediate the targeting and translocation of preproteins as efficiently as mammalian SRP and SR despite the heterologous nature of this assay (44). This strongly suggests that the SRP-ribosome interactions are highly conserved across species and that the heterologous targeting assay provides a reasonable system to test insights from our biophysical measurements in the bacterial system in the context of a complete and functional targeting reaction. Constructs for the protein translocation assay were based on the plasmid pSPBP4. The hydrophobic core of the pPL signal sequence was replaced with the model signal sequences (figure 5.S7) using the QuickChange mutagenesis procedure (Stratagene).

5.5.10 Numerical analysis of protein targeting efficiency

This analysis estimates the fraction of each cargo that can be successfully targeted by the SRP pathway within a limited time window, t_w , before the nascent chain exceeds ~ 110 residues (113). This time window was based on the consideration that the SRP loses its ability to target substrates when the nascent chain exceeds ~ 110 residues (87, 113). Since the bacterial SRP does not arrest translation (2), this gives a t_w of ~ 3 second (or 6 second when eukaryotic ribosome was used) for the SRP to complete protein targeting (112), assuming that SRP begins to recognize cargos when the nascent chain is ~ 35 amino acids long and a translation elongation rate of ~ 20 – 30 amino acids/second in bacteria (or 10-15 amino acids/second for eukaryotic ribosome) (114).

During the first step, the fraction of cargos that bind to SRP is calculated from:

$P(1) = [SRP]/(K_d + [SRP])$, using a cellular SRP concentration of 400 nM (83) and the K_d values from figure 5.1. During the second step, the fraction of cargos that are delivered to the membrane after stable SRP-SR complex assembly is calculated from:

$P(2) = P(1) \times \exp(-k_{on}[SR] \times t_w)$, using a SR concentration of 2 μ M (as was the condition used in the protein targeting reactions in figures 5.4B and 5.S7), the k_{on} values determined in Figure 5.3C, and a time window (t_w) of 3- or 6-seconds for *E coli* and eukaryotic ribosomes, respectively. During the last step, the fraction of cargos that can be unloaded to the protein conducting channel (PCC) before GTP hydrolysis is calculated from: $P(3) = P(2) \times [1 - \exp(-k_{GTPase} \times t_{PCC})]$, using the GTP hydrolysis rate constants (k_{GTPase}) determined in Figure 5.3F. t_{PCC} denotes the lifetime for cargo unloading and was estimated to be ~ 3 s, as in the presence of the correct cargos the late conformational changes in the SRP•SR GTPase complex that are important for driving cargo unloading become rate limiting (5) and likely takes the majority of the 3s time window for protein targeting.

5.6 Supplementary text

5.6.1 A sequential model for rejection of incorrect cargos by additional checkpoints in the SRP pathway following the cargo-binding step

In this chapter, we postulated and tested the model that after the cargos are loaded on the SRP, the incorrect cargos could be less efficient during subsequent steps of targeting; these steps thereby provide additional checkpoints to help reject incorrect cargos (35). We considered the following potential checkpoints: (1) Formation of the *early* SRP•SR complex (figure 5.1A, step 2), an obligatory intermediate preceding the formation of subsequent complexes (4, 5). This intermediate is highly unstable with free SRP, and >98% of it dissociates before rearranging into the subsequent complex. A strong cargo could stabilize the *early* intermediate and prevent its premature disassembly (5). If incorrect cargos could not provide such a stabilization, then their *early* targeting complexes would be more likely to disassemble and exit the SRP pathway prematurely (figure 5.1A, arrow b). (2) Rearrangement of the *early* intermediate to the *closed* complex (figure 5.1A, step 3), which is essential for switching the SRP from a cargo-binding to a cargo-releasing mode and primes the cargo for unloading (5). If incorrect cargos were less efficient in this rearrangement, then their late stages of targeting would be delayed (figure 5.1A, arrow c). (3) GTP hydrolysis from the SRP•SR complex, which occurs rapidly in the absence of cargo (66). A strong cargo could delay GTP hydrolysis, providing the cargo•SRP•SR complex an important time window to search for the target membrane and the PCC before GTP hydrolysis drives the irreversible disassembly of the targeting complex (figure 5.1A, steps 4 vs. 5) (5). If incorrect cargos could not delay GTP hydrolysis as effectively, they would be more likely to be rejected through

premature GTP hydrolysis (figure 5.1A, arrow d). This would further improve the fidelity of targeting via kinetic proofreading. Beside SRP, the protein translocation machinery also discriminates against incorrect cargos (109, 110). However, the translocation machinery mediates translocation of proteins from both the SRP- and SecB-pathways, including EspP (111). Thus it is unlikely to be solely responsible for the stringent substrate selection by the SRP.

5.6.2 *E. coli* cytosolic factors do not compete with SRP for binding the RNC

It has been suggested that cellular chaperones that interact with translating ribosomes, such as trigger factor (TF), can compete with SRP for binding to the RNCs and thus increase the specificity of SRP-cargo binding (107, 124). However, the presence of up to 80 μ M TF did not compete away the binding of SRP to either the correct (RNC_{ftsQ}), borderline (RNC_{phoA}), or incorrect (RNC_{Luciferase}) cargos (figure S2A), consistent with previous findings (108). Even in the presence of SRP- and ribosome-free *E. coli* total cytosolic extract (see Methods), SRP-RNC binding affinities were not significantly affected (figure 5.S2, B-C). These results strongly suggest that cytosolic factors do not compete with SRP to increase the specificity of SRP-cargo binding.

5.6.3 Additional considerations of substrate selection by the SRP in vivo

The analyses in this work considered how the SRP handles each substrate protein during a single round of protein targeting. In vivo, a higher fidelity could be achieved by the SRP because of several factors. First, correct cargos are delivered more rapidly than the incorrect cargos; this would allow a larger number of the correct than incorrect cargos

to be targeted within a given time window during multiple rounds of protein targeting. Second, the SRP-SR interaction kinetics could be slower *in vivo* than *in vitro*, as protein diffusion rates tend to be slower within the crowded cellular environment. This would render the SRP-SR complex assembly step more rate-limiting for the targeting reaction *in vivo* and thus increase the contribution of this step to rejection of borderline substrates such as *phoA*. On the other hand, the membrane association of the SRP receptor FtsY could also affect the kinetics of SRP-SR interactions and the cargo unloading steps, rendering these downstream step(s) more or less rate-limiting. However, FtsY's localization could not affect the interaction of free SRP with the RNC, and thus would not change the conclusion that differences in SRP-cargo binding affinities do not provide sufficient discrimination against the incorrect cargos. Finally, competition between the strong and weak cargos may lower the effective concentration of free SRP *in vivo*; this would allow some of the discrimination in SRP's cargo binding affinities to be realized. Nevertheless, regardless of the effective SRP concentration *in vivo*, mechanisms based solely on discrimination in SRP-cargo binding affinities would not be able to reproduce the experimentally observed pattern of substrate selection (figure 5.S8). Under all conditions, such a mechanism predicts that EspP would be targeted with similar efficiency as *phoA-3A7L*, and that *phoA*, *phoA-5A5L* and *phoA-8A2L* would be targeted with the same efficiencies (figure 5.S8, dashed lines); these predictions are not supported by experimental data (figure 5.S8, red). Thus subsequent steps following cargo binding would be essential for the SRP to select the correct set of substrate proteins even in the presence of competition between correct and incorrect cargos. In addition, the *secY* translocation machinery provides another important checkpoint to discriminate against

incorrect cargos such as phoA-8A2L (109, 110); we could not detect this additional discrimination as the targeting efficiency of this substrate before arrival at the translocation machinery is already $\leq 1\%$.

5.6.4 Table

Table 5.S1. Kinetic and thermodynamic parameters for individual reaction step during SRP-dependent protein targeting in the presence of various cargos. Error bars are SDs from three independent experiments.

	K_d (nM)	K_d (nM)	FRET end point	$k_{e \rightarrow c}$ (s^{-1})	k_{on} ($M^{-1} \cdot s^{-1}$)	GTPase rate (s^{-1})
	RNC binding	early complex	early complex	early \rightarrow closed rearrangement	closed complex	
1A9L	0.55 ± 0.20	78 ± 5	0.68 ± 0.02	0.31 ± 0.02	9.9 $\pm 1.3 \times 10^6$	0.11 ± 0.01
2A8L	1.2 ± 0.20	110 ± 8	0.64 ± 0.02	N.D.	8.8 $\pm 1.6 \times 10^6$	0.12 ± 0.02
3A7L	8.4 ± 2.0	158 ± 10	0.57 ± 0.02	0.19 ± 0.01	2.0 $\pm 0.2 \times 10^5$	0.18 ± 0.01
EspP	13.6 ± 3.0	311 ± 21	0.41 ± 0.03	0.060 ± 0.02	9.2 $\pm 0.2 \times 10^3$	0.51 ± 0.08
phoA	108 ± 11	310 ± 20	0.59 ± 0.03	0.18 ± 0.02	6.3 $\pm 0.4 \times 10^4$	0.45 ± 0.02
5A5L	63 ± 4	910 ± 50	0.42 ± 0.02	0.084 ± 0.003	1.1 $\pm 0.2 \times 10^4$	0.38 ± 0.02
8A2L	100 ± 5	≥ 2630	≥ 0.48	0.028 ± 0.003	5.6 $\pm 0.3 \times 10^3$	N.D.
Lucife -rase	130 ± 12	2060 ± 201	0.34 ± 0.02	0.039 ± 0.003	1.8 $\pm 0.3 \times 10^3$	0.65 ± 0.22

N.D.: not determined.

5.7 Supplementary Figures

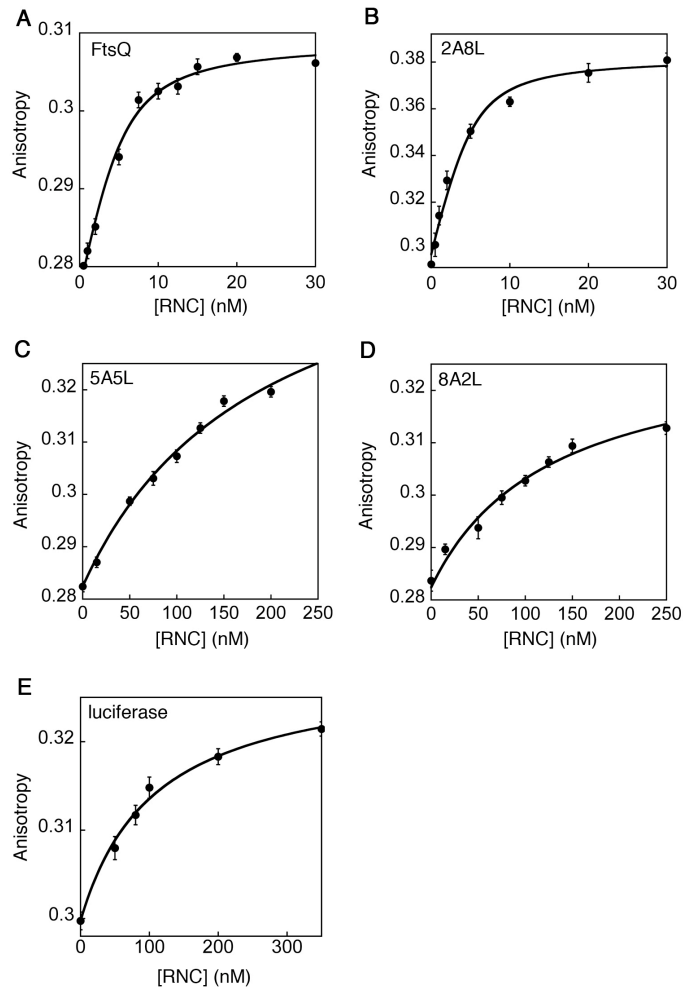


Figure 5.S1. The binding affinities of SRP for different cargoes. Equilibrium titrations to measure cargo-SRP binding were carried out as described in the Methods. K_d values of each cargo (Table S1) were derived from quadratic fits of data according to Eq (5.3). Error bars are SDs from three independent experiments.

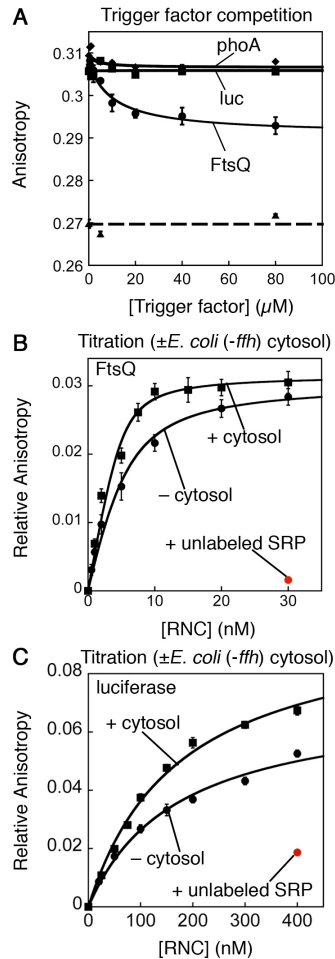


Figure 5.S2. Trigger factor and SRP-free *E. coli* (-*ffh*) total cytosol do not displace the SRP from the RNCs. (A) Fluorescence anisotropy of cargo-loaded SRP in the presence of increasing amounts of trigger factor. RNC_{FtsQ} (●), RNC_{phoA} (u) and RNC_{luciferase} (■) are used as representatives of correct, weak and wrong cargos, respectively. The dashed line represents the anisotropy value of free SRP (▲). At each concentration, TF has been incubated with the RNC•SRP complex for sufficient time (15–30 min) to ensure that equilibrium has been reached. (B, C) Equilibrium titrations to measure the binding affinities of SRP for RNC_{FtsQ} (B) and RNC_{luciferase} (C) in the presence (■) and absence (●) of SRP- and ribosome-free *E. coli* (-*ffh*) total cytosolic extract. Nonlinear fits of data to Eq. (5.3) gave K_d values of 0.10 ± 0.02 and 0.67 ± 0.11 nM for RNC_{FtsQ} with and without cytosol (B), respectively, and 174 ± 14 and 170 ± 10 nM for RNC_{luciferase} with and without *E. coli* cytosol (C), respectively. In all titration experiments, fluorescence anisotropy changes can be competed away by unlabeled SRP (●). Error bars are SDs from three independent experiments.

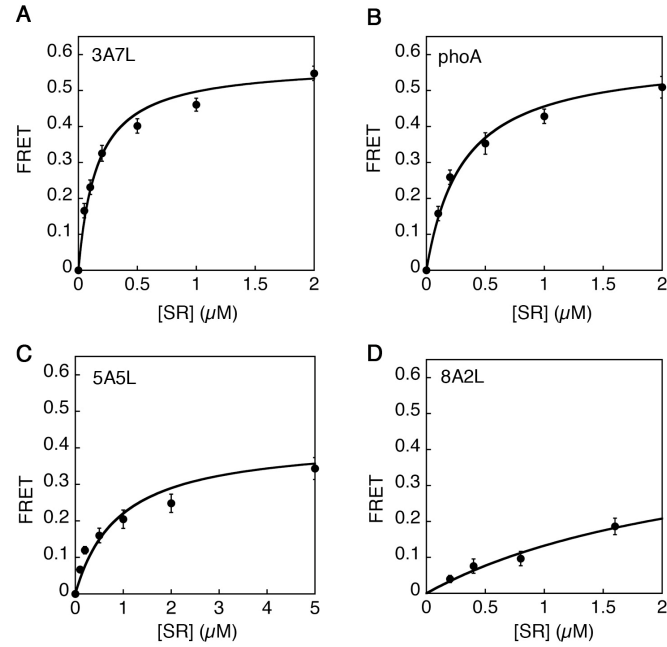


Figure 5.S3. Stabilities of the SRP•SR *early* intermediates formed with different cargoes. Equilibrium titrations of the *early* intermediate were carried out as described in the Methods. Nonlinear fits of data to Eq (5.4) gave K_d values of the *early* intermediate in the presence of each cargo (Table 5.S1). Error bars are SDs from three independent experiments.

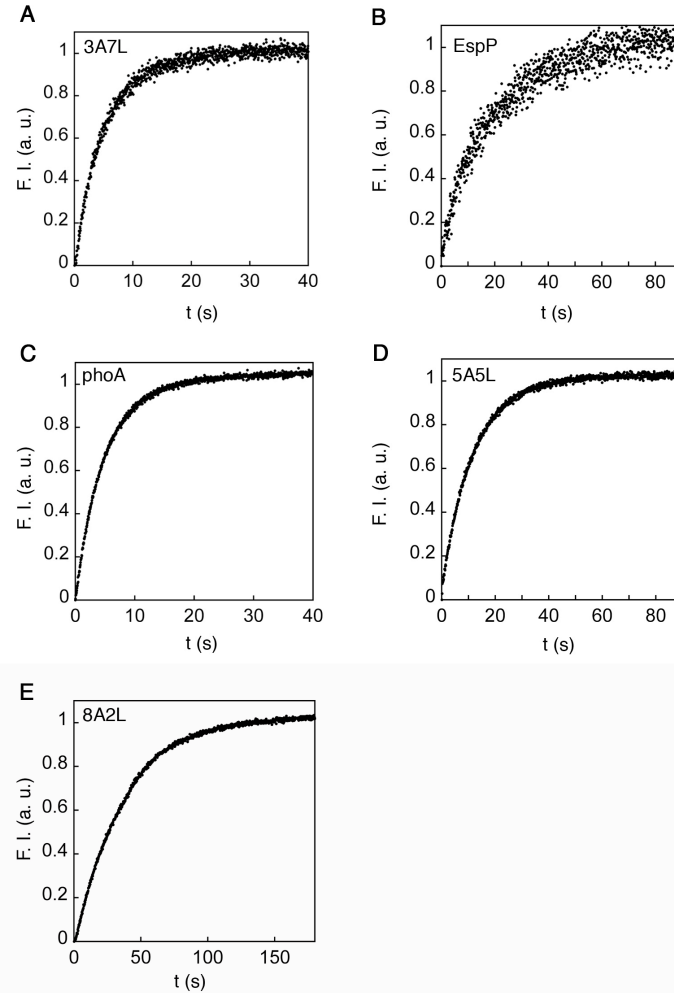


Figure 5.S4. The *early*→*closed* rearrangement is slower with weaker cargos. Rate constants of the GTPase rearrangements were measured using acrylodan-labeled SRP(C235) as described in the Methods. Rate constants with each cargo (Table S1) were derived from nonlinear fits of the data to Eq. (5.5). Reactions were carried out with 100 – 250 nM SRP, 200 nM RNC_{3A7L} and RNC_{EspP} or 500 nM RNC's with other signal sequences, and 50 –75 μ M SR.

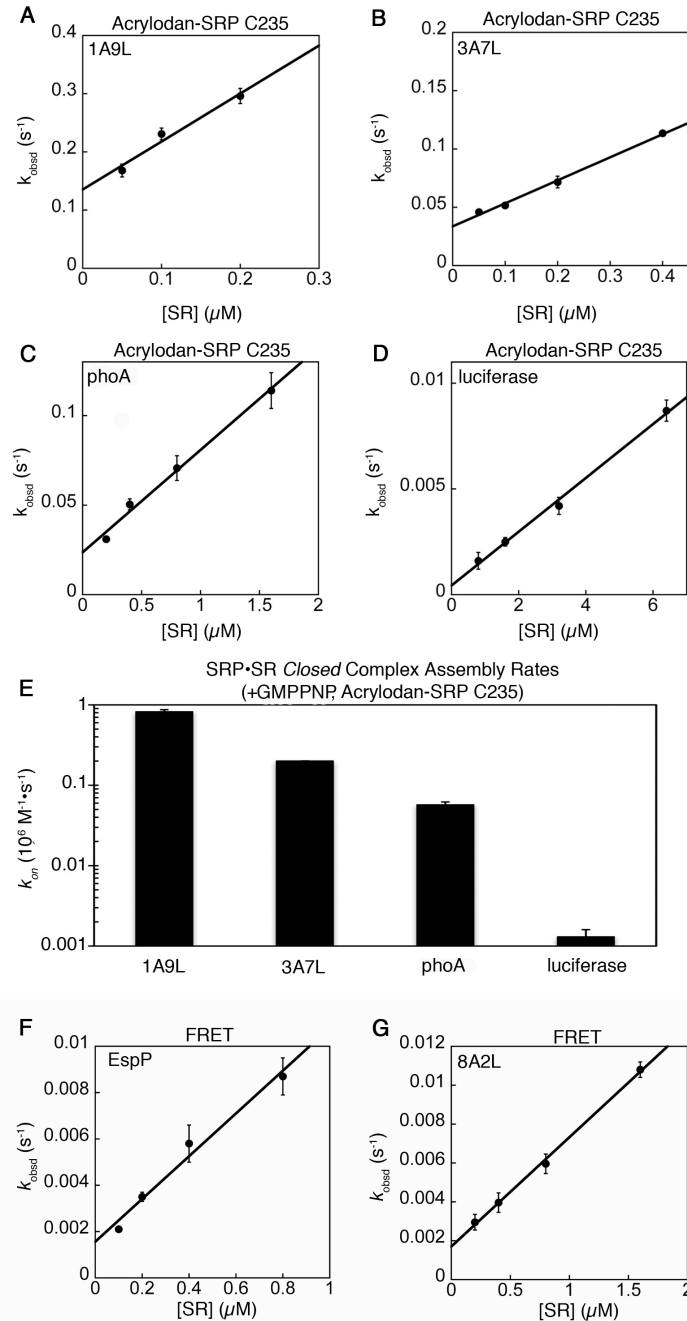


Figure 5.S5. Rate constants for assembly of the SRP•SR *closed* complex. (A-D) Complex assembly rate constants were determined using acrylodan-labeled SRP(C235) as described in the Methods. Linear fits of data to Eq (5.6) gave second order constants of complex assembly (k_{on}) of 0.82 ± 0.05 , 0.20 ± 0.04 , 0.057 ± 0.005 , and $0.0013 \pm 0.0003 \times 10^6 \text{ M}^{-1} \text{ s}^{-1}$ with RNC_{1A9L} (A), RNC_{3A7L} (B), RNC_{phoA} (C), and RNC_{luciferase} (D) respectively. (E) Summary of *closed* complex assembly rates with different cargoes measured by acrylodan-labeled SRP(C235). (F, G) Complex assembly rate constants for RNC_{EspP} and RNC_{8A2L} measured using FRET. Second order constants of complex assembly (k_{on}) were obtained from linear fits of the data to Eq (5.6) (Table 5.S1). Error bars are SDs from three independent experiments.

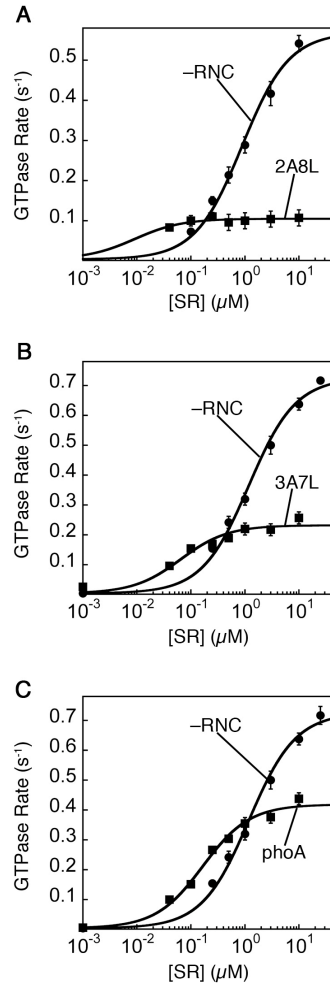


Figure 5.S6. Effects of different cargos on GTPase activation in the SRP-SR complex. GTPase reactions were carried out and analyzed as described in the Methods. GTPase rate constants (k_{cat}) from the cargo•SRP•SR complexes were obtained from nonlinear fits of data to Eq (5.7) (Table 5.S1). Error bars are SDs from three independent experiments.

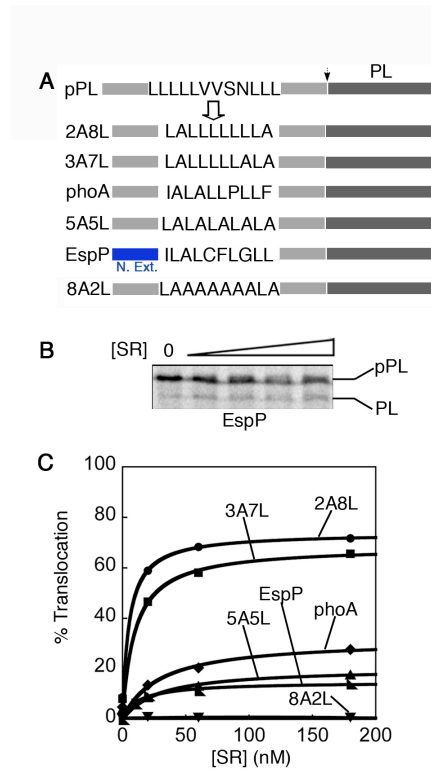


Figure 5.S7. Experimental determination of protein targeting efficiency of substrates bearing the different signal sequences. (A) Schematic diagram depicting the chimeric pPL constructs used for the co-translational protein targeting assay (see Methods). The arrow between signal sequence (light grey) and mature protein (dark grey) shows the signal peptidase cleavage site from pPL. Blue denotes the N-terminal signal peptide extension of EspP construct. (B) SRP-dependent protein targeting and translocation efficiency of substrates with EspP signal sequences analyzed by SDS-PAGE. pPL and PL denote the precursor and signal sequence-cleaved forms of the substrate protein, respectively. (C) Quantification of the protein targeting and translocation efficiencies of each substrate tested.

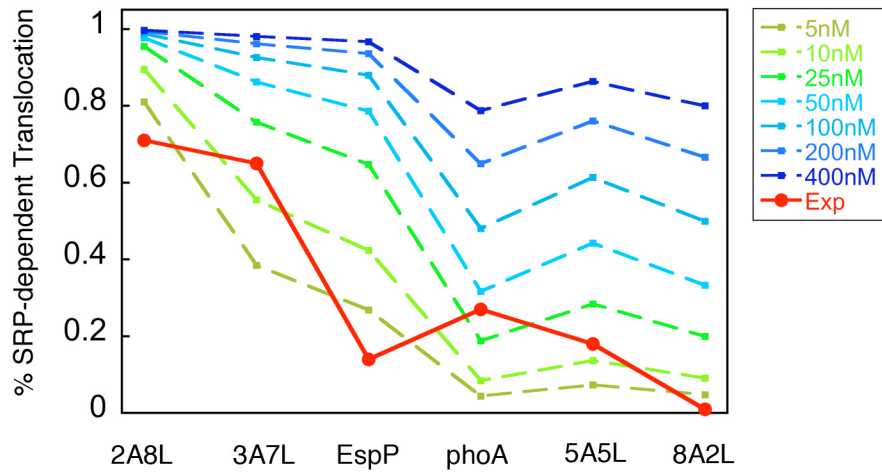


Figure 5.S8. Models based solely on discrimination in cargo-binding affinities would not reproduce the experimentally observed pattern of substrate selection by the SRP pathway. Numerical analysis for protein targeting and translocation efficiencies was carried out as described in the Methods assuming a one-step mechanism of substrate selection based on the binding affinities of SRP to different cargo substrates. Different effective concentrations of free SRP ranging from 5 to 400 nM (specified in the top right panel) were used. The red line depicts the experimentally determined protein targeting and translocation efficiencies (from figure 5.4C in main text) and was shown for comparison.

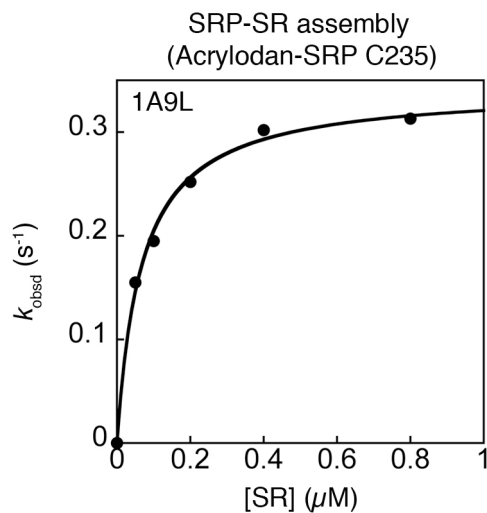


Figure 5.S9. Acrylodan-labeled SRP C235 monitors two-step assembly of the SRP-SR closed complex. Observed complex assembly rate constants were determined using acrylodan-labeled SRP(C235) as described in the Methods. The deviation from linearity of the observed rates indicate that assembly of the closed complex is a two-step process, with a unimolecular rearrangement rate-limiting at saturating SR concentrations. Nonlinear fits of data to Eq (5.7) gave the rearrangement rate from the early to the closed complex as 0.34 s^{-1} with $\text{RNC}_{1\text{A}9\text{L}}$.

5.8 Acknowledgments

We thank C. Schaffitzel and N. Ban for help with the purification of RNCs and trigger factor, J. Luirink for plasmids encoding the *phoA* signal sequence variants, L. Randall for the plasmid encoding luciferase, B. Bukau and E. Deurling for the plasmid encoding trigger factor, H. D. Bernstein for the strain HDB51, and R. J. Deshaies, A. Varshavsky, W. Zhong, N. Pierce, and the Shan laboratory for comments on the manuscript. This work was supported by NIH grant GM078024, career awards from the Burroughs Welcome Foundation, the Henry and Camille Dreyfus foundation, the Beckman foundation, and the Packard foundation to S. S.

Bibliography

1. B. Alberts, *Cell* **92**, 291 (1998).
2. P. Walter, A. E. Johnson, *Annu Rev Cell Biol* **10**, 87 (1994).
3. S. O. Shan, S. L. Schmid, X. Zhang, *Biochemistry* **48**, 6696 (2009).
4. X. Zhang, S. Kung, S. O. Shan, *J Mol Biol* **381**, 581 (2008).
5. X. Zhang, C. Schaffitzel, N. Ban, S. O. Shan, *Proc Natl Acad Sci U S A* **106**, 1754 (2009).
6. K. E. S. Matlack, W. Mothes, T. A. Rapoport, *Cell* **92**, 381 (1998).
7. A. E. Johnson, M. A. van Waes, *Annu Rev Cell Dev Biol* **15**, 799 (1999).
8. S. O. Shan, P. Walter, *Febs Lett* **579**, 921 (2005).
9. S. O. Shan, R. M. Stroud, P. Walter, *Plos Biol* **2**, 1572 (2004).
10. S. O. Shan, S. Chandrasekar, P. Walter, *J. Cell Biol* **178**, 611 (2007).
11. P. Walter, I. Ibrahimi, G. Blobel, *J. Cell Biol* **91**, 545 (1981).
12. P. Walter, G. Blobel, *J Cell Biol* **91**, 551 (1981).
13. P. Walter, G. Blobel, *J Cell Biol* **91**, 557 (1981).
14. R. T. Batey, R. P. Rambo, L. Lucast, B. Rha, J. A. Doudna, *Science* **287**, 1232 (2000).
15. R. J. Keenan, D. M. Freymann, P. Walter, R. M. Stroud, *Cell* **94**, 181 (1998).
16. U. C. Krieg, P. Walter, A. E. Johnson, *Proc Natl Acad Sci U S A* **83**, 8604 (1986).
17. T. V. Kurzchalia, M. Wiedmann, A. S. Girshovich, E. S. Bochkareva, H. Bielka, T. A. Rapoport, *Nature* **320**, 634 (1986).
18. D. Zopf, H. D. Bernstein, A. E. Johnson, P. Walter, *EMBO J.* **9**, 4511 (1990).
19. T. Connolly, P. J. Rapiejko, R. Gilmore, *Science* **252**, 1171 (1991).

20. P. F. Egea, S. O. Shan, J. Napetschnig, D. F. Savage, P. Walter, R. M. Stroud, *Nature* **427**, 215 (2004).
21. P. Peluso, D. Herschlag, S. Nock, D. M. Freymann, A. E. Johnson, P. Walter, *Science* **288**, 1640 (2000).
22. T. Powers, P. Walter, *Science* **269**, 1422 (1995).
23. R. M. Cleverley, L. M. Gierasch, *J Biol Chem* **277**, 46763 (2002).
24. H. R. Bourne, D. A. Sanders, F. McCormick, *Nature* **349**, 117 (1991).
25. J. Gawronski-Salerno, J. S. V. Coon, P. J. Focia, D. M. Freymann, *Proteins* **66**, 984 (2007).
26. P. J. Focia, J. Gawronski-Salerno, J. S. Coon, D. M. Freymann, *J Mol Biol* **360**, 631 (2006).
27. D. M. Freymann, R. J. Keenan, R. M. Stroud, P. Walter, *Nat Struct Biol* **6**, 793 (1999).
28. D. M. Freymann, R. J. Keenan, R. M. Stroud, P. Walter, *Nature* **385**, 361 (1997).
29. P. Peluso, S. O. Shan, S. Nock, D. Herschlag, P. Walter, *Biochemistry* **40**, 15224 (2001).
30. S. Q. Gu, J. Jockel, P. Beinker, J. Warnecke, Y. P. Semenkov, M. V. Rodnina, W. Wintermeyer, *RNA-Publ RNA Soc* **11**, 1374 (2005).
31. F. Y. Siu, R. J. Spangord, J. A. Doudna, *RNA-Publ RNA Soc* **13**, 240 (2007).
32. M. B. Sagar, L. Lucast, J. A. Doudna, *RNA-Publ RNA Soc* **10**, 772 (2004).
33. S. Brown, M. J. Fournier, *J Mol Biol* **178**, 533 (1984).
34. J. R. Jagath, N. B. Matassova, E. De Leeuw, J. M. Warnecke, G. Lentzen, M. V. Rodnina, J. Luirink, W. Wintermeyer, *RNA-Publ RNA Soc* **7**, 293 (2001).

35. N. Zheng, L. M. Gierasch, *Mol Cell* **1**, 79 (1997).
36. M. A. Poritz, K. Strub, P. Walter, *Cell* **55**, 4 (1988).
37. M. A. Poritz, K. Strub, P. Walter, *Science* **250**, 1111 (1990).
38. R. T. Batey, M. B. Sagar, J. A. Doudna, *J Mol Biol* **307**, 229 (2001).
39. T. Hainzl, S. Huang, A. E. Sauer-Eriksson, *Proc Natl Acad Sci U S A* **104**, 14911 (2007).
40. R. M. Stroud, P. Walter, *Curr Opin Struct Biol* **9**, 754 (1999).
41. R. J. Spangord, F. Siu, A. L. Ke, J. A. Doudna, *Nat Struct Mol Biol* **12**, 1116 (2005).
42. E. C. Mandon, Y. Jiang, R. Gilmore, *J Cell Biol* **162**, 575 (2003).
43. I. Buskiewicz, F. Peske, H. J. Wieden, I. Gryczynski, M. V. Rodnina, W. Wintermeyer, *J Mol Biol* **351**, 417 (2005).
44. T. Powers, P. Walter, *EMBO J* **16**, 4880 (1997).
45. T. Connolly, R. Gilmore, *Cell* **57**, 599 (1989).
46. P. J. Rapiejko, R. Gilmore, *J Cell Biol* **117**, 493 (1992).
47. D. Zopf, H. D. Bernstein, P. Walter, *J Cell Biol* **120**, 1113 (1993).
48. J. R. Jagath, M. V. Rodnina, W. Wintermeyer, *J Mol Biol* **295**, 745 (2000).
49. S. Padmanabhan, D. M. Freymann, *Structure* **9**, 859 (2001).
50. U. D. Ramirez, G. Minasov, P. J. Focia, R. M. Stroud, P. Walter, P. Kuhn, D. M. Freymann, *J Mol Biol* **320**, 783 (2002).
51. P. J. Focia, H. Alam, T. Lu, U. D. Ramirez, D. M. Freymann, *Proteins* **54**, 222 (2004).

52. J. R. Lakowicz, Principles of fluorescence spectroscopy, *Kluwer Academic/Plenum Publishers, London*, (1999).
53. A. C. Gavin, Bosche, M., Krause, R., Grandi, P., Marzioch, M., Bauer, A., Schultz, J., Rick, J. M., Michon, A. M., Cruciat, C. M., Remor, M., Hofert, C., Schelder, M., Brajenovic, M., Ruffner, H., Merino, A., Klein, K., Hudak, M., Dickson, D., Rudi, T., Gnau, V., Bauch, A., Bastuck, S., Huhse, B., Leutwein, C., Heurtier, M. A., Copley, R. R., Edlmann, A., Querfurth, E., Rybin, V., Drewes, G., Raida, M., Bouwmeester, T., Bork, P., Seraphin, B., Kuster, B., Neubauer, G., Superti-Furga, G. *Nature* **415**, 141 (2002).
54. G. Schreiber, G. Haran, H. X. Zhou, *Chem Rev*, (2009).
55. D. D. Boehr, P. E. Wright, *Science* **320**, 1429 (2008).
56. T. L. Blundell, J. Fernandez-Recio, *Nature* **444**, 279 (2006).
57. D. E. Koshland, *Proc Natl Acad Sci U S A* **44**, 98 (1958).
58. B. Ma, S. Kumar, C. J. Tsai, R. Nussinov, *Protein Eng* **12**, 713 (1999).
59. R. Grunberg, J. Leckner, M. Nilges, *Structure* **12**, 2125 (2004).
60. G. Schreiber, A. R. Fersht, *Nat Struct Biol* **3**, 427 (1996).
61. O. F. Lange, Lakomek, N. A., Fares, C., Schroder, G. F., Walter, K. F., Becker, S., Meiler, J., Grubmuller, H., Griesinger, C., de Groot, B. L., *Science* **320**, 1471 (2008).
62. C. Tang, J. Iwahara, G. M. Clore, *Nature* **444**, 383 (2006).
63. P. B. Crowley, M. Ubbink, *Acc Chem Res* **36**, 723 (2003).
64. T. Kimura, J. C. Lee, H. B. Gray, J. R. Winkler, *Proc Natl Acad Sci U S A* **106**, 7834 (2009).

65. N. A. Baker, D. Sept, S. Joseph, M. J. Holst, J. A. McCammon, *Proc Natl Acad Sci U S A* **98**, 10037 (2001).
66. P. Peluso, S. O. Shan, S. Nock, D. Herschlag, P. Walter, *Biochemistry* **40**, 15224 (2001).
67. C. Schaffitzel, N. Ban, *J Struct Biol* **158**, 463 (2007).
68. T. Bornemann, J. Jockel, M. V. Rodnina, W. Wintermeyer, *Nat Struct Mol Biol* **15**, 494 (2008).
69. J. C. Lee, K. C. Engman, F. A. Tezcan, H. B. Gray, J. R. Winkler, *Proc Natl Acad Sci U S A* **99**, 14778 (2002).
70. J. C. Lee, R. Langen, P. A. Hummel, H. B. Gray, J. R. Winkler, *Proc Natl Acad Sci U S A* **101**, 16466 (2004).
71. J. M. Beals, E. Haas, S. Krausz, H. A. Scheraga, *Biochemistry* **30**, 7680 (1991).
72. J. M. Beechem, E. Haas, *Biophys J* **55**, 1225 (1989).
73. A. A. Istratov, O. F. Vyvenko, *Rev Sci Instrum* **70**, 1233 (1999).
74. D. L. Ermak, J. A. Mccammon, *J Chem Phys* **69**, 1352 (1978).
75. H. R. Bourne, *Nature* **321**, 814 (1986).
76. J. R. Jagath, M. V. Rodnina, G. Lentzen, W. Wintermeyer, *Biochemistry* **37**, 15408 (1998).
77. S. O. Shan, P. Walter, *Proc Nat Acad Sci U S A* **100**, 4480 (2003).
78. Y. Lu, Qi, H. Y., Hyndman, J. B., Ulbrandt, N. D., Teplyakov, A., Tomasevic, N., Bernstein, H. D., *EMBO J* **20**, 6724 (2001).
79. J. D. Miller, H. Wilhelm, L. Gierasch, R. Gilmore, P. Walter, *Nature* **366**, 351 (1993).

80. X. Zhang, S. Kung, S. O. Shan, *J Mol Biol* **381**, 581 (2008).
81. K. Mitra, Schaffitzel, C., Shaikh, T., Tama, F., Jenni, S., Brooks, C. L., Ban, N., and Frank, J., *Nature* **438**, 318 (2005).
82. C. Schaffitzel, C., Oswald, M., Berger, I., Ishikawa, T., Abrahams, J. P., Koerten, H. K., Koning, R. I., and Ban, N., *Nature* **444**, 503 (2006).
83. A. Fersht, *Structure and Mechanism in Protein Science : A Guide to Enzyme Catalysis and Protein Folding*. (W.H. Freeman, New York, 1999), pp. xxi, 631 p.
84. C. G. Jensen, S. Pedersen, *J Bacteriol* **176**, 7148 (1994).
85. M. Halic, Gartmann, M., Schlenker, O., Mielke, T., Pool, M. R., Sinning, I., and Beckmann, R., *Science* **312**, 745 (2006).
86. T. Bornemann, J. Jockel, M. V. Rodnina, W. Wintermeyer, *Nat Struct Mol Biol* **15**, 494 (2008).
87. J. J. Flanagan, Chen, J. C., Miao, Y. W., Shao, Y. L., Lin, J. L., Bock, P. E., and Johnson, A. E., *J Biol Chem* **278**, 18628 (2003).
88. P. J. Rapiejko, R. Gilmore, *Cell* **89**, 703 (1997).
89. G. Bacher, H. Lutcke, B. Jungnickel, T. A. Rapoport, B. Dobberstein, *Nature* **381**, 248 (1996).
90. W. Q. Song, D. Raden, E. C. Mandon, R. Gilmore, *Cell* **100**, 333 (2000).
91. M. Halic *et al.*, Blau, M., Becker, T., Mielke, T., Pool, M. R., Wild, K., Sinning, I., and Beckmann, R., *Nature* **444**, 507 (2006).
92. M. R. Pool, J. Stumm, T. A. Fulga, I. Sinning, B. Dobberstein, *Science* **297**, 1345 (2002).
93. M. V. Rodnina, W. Wintermeyer, *Annu Rev Biochem* **70**, 415 (2001).

94. C. Schaffitzel, N. Ban, *J Struct Biol* **159**, 302 (2007).
95. D. Moazed, H. F. Noller, *Cell* **57**, 585 (1989).
96. T. A. Rapoport, *Nature* **450**, 663 (2007).
97. C. A. Kaiser, D. Preuss, P. Grisafi, D. Botstein, *Science* **235**, 312 (1987).
98. L. M. Gierasch, *Biochemistry* **28**, 923 (1989).
99. R. S. Hegde, H. D. Bernstein, *Trends Biochem Sci* **31**, 563 (2006).
100. G. von Heijne, *J Mol Biol* **184**, 99 (1985).
101. H. D. Bernstein, Poritz, M. A., Strub, K., Hoben, P. J., Brenner, S., Walter, P. ,
Nature **340**, 482 (1989).
102. D. Huber, Boyd, D., Xia, Y., Olma, M. H., Gerstein, M., Beckwith, J., *J Bacteriol*
187, 2983 (2005).
103. Q. A. Valent, Kendall, D. A., High, S., Kusters, R., Oudega, B., Luirink, J.,
EMBO J **14**, 5494 (1995).
104. S. K. Doud, M. M. Chou, D. A. Kendall, *Biochemistry* **32**, 1251 (1993).
105. J. H. Peterson, R. L. Szabady, H. D. Bernstein, *J Biol Chem* **281**, 9038 (2006).
106. N. Bradshaw, S. B. Neher, D. S. Booth, P. Walter, *Science* **323**, 127 (2009).
107. S. Q. Gu, F. Peske, H. J. Wieden, M. V. Rodnina, W. Wintermeyer, *RNA-Publ*
RNA Soc **9**, 566 (2003).
108. I. Buskiewicz, Deuerling, E., Gu, S. Q., Jockel, J., Rodnina, M. V., Bukau, B.,
Wintermeyer, W., *Proc Natl Acad Sci U S A* **101**, 7902 (2004).
109. B. Jungnickel, T. A. Rapoport, *Cell* **82**, 261 (1995).
110. R. S. Hegde, S. W. Kang, *J Cell Biol* **182**, 225 (2008).

111. Q. A. Valent, Scotti, P. A., High, S., de Gier, J. W., von Heijne, G., Lentzen, G., Wintermeyer, W., Oudega, B., Luirink, J., *EMBO J* **17**, 2504 (1998).
112. N. Zheng, L. M. Gierasch, *Cell* **86**, 849 (1996).
113. V. Siegel, P. Walter, *EMBO J.* **7**, 1769 (1988).
114. P. P. Dennis, M. Nomura, *Proc Natl Acad Sci U S A* **71**, 3819 (1974).
115. S. O. Shan, S. Chandrasekar, P. Walter, *J Cell Biol* **178**, 611 (2007).
116. M. V. Rodnina, W. Wintermeyer, *Trends Biochem.Sci.* **26**, 124 (2001).
117. L. Cochella, R. Green, *Curr Biol* **15**, R536 (2005).
118. A. R. Fersht, M. M. Kaethner, *Biochemistry* **15**, 3342 (1976).
119. T. A. Kunkel, K. Bebenek, *Annu Rev Biochem* **69**, 497 (2000).
120. S. M. Uptain, C. M. Kane, M. J. Chamberlin, *Annu Rev Biochem* **66**, 117 (1997).
121. B. Bonven, K. Gullov, *Mol Gen Genet* **170**, 225 (1979).
122. R. S. Ullers, Houben, E. N., Raine, A., ten Hagen-Jongman, C. M., Ehrenberg, M., Brunner, J., Oudega, B., Harms, N., Luirink, J. *J Cell Biol* **161**, 679 (2003).
123. G. Kramer, Rutkowska, A., Wegrzyn, R. D., Patzelt, H., Kurz, T. A., Merz, F., Rauch, T., Vorderwulbecke, S., Deuerling, E., Bukau, B. *et al.*, *J Bacteriol* **186**, 3777 (2004).
124. H. C. Lee, H. D. Bernstein, *Proc Natl Acad Sci U S A* **98**, 3471 (2001).